

Design, Analysis, and Characterization of Indirectly-pumped Terahertz Quantum Cascade Lasers

by

Seyed Ghasem Razavipour

A thesis
presented to the University of Waterloo
in fulfillment of the
thesis requirement for the degree of
Doctor of Philosophy
in
Electrical and Computer Engineering

Waterloo, Ontario, Canada, 2013

© Seyed Ghasem Razavipour 2013

I hereby declare that I am the sole author of this thesis. This is a true copy of the thesis, including any required final revisions, as accepted by my examiners.

I understand that my thesis may be made electronically available to the public.

Abstract

Quantum cascade laser (QCL), as a unipolar semiconductor laser based on intersubband transitions in quantum wells, covers a large portion of the Mid and Far Infrared electromagnetic spectrum. The frequency of the optical transition can be determined by engineering the layer sequence of the heterostructure. The focus of this work is on Terahertz (THz) frequency range (frequency of 1 - 10 THz and photon energy of $\sim 4 - 40$ meV), which is lacking of high power, coherent, and efficient narrowband radiation sources. THz QCL, demonstrated in 2002, as a perfect candidate of coherent THz source, is still suffering from the empirical operating temperature limiting factor of $T \approx \hbar\omega/k_B$, which allows this source to work only under a cryogenic system.

Most of high performance THz QCLs, including the world record design which lased up to ~ 200 K, are based on a resonant phonon (RP) scheme, whose population inversion is always less than 50%. The indirectly-pumped (IDP) QCL, nicely implemented in MIR frequency, starts to be a good candidate to overcome the aforementioned limiting factor of RP-QCL.

A rate equation (RE) formalism, which includes both coherent and incoherent transport process, will be introduced to model the carrier transport of all presented structures in this thesis. The second order tunneling which employed the intrasubband roughness and impurity scattering, was implemented in our model to nicely predict the behavior of the QCL designs. This model, which is easy to implement and fast to calculate, could help us to engineer the electron wavefunctions of the structure with optimization tools. We developed a new design scheme which employs the phonon scattering mechanism for both injecting carrier to the upper lasing state and extracting carrier from lower lasing state. Since there is no injection/extraction state to be in resonance with lasing states, this simple design scheme does not suffer from broadening due to the tunneling. Finally, three different THz IDP-QCLs, based on phonon-photon-phonon (3P) scheme were designed, grown, fabricated, and characterized.

The performance of those structures in terms of operating temperature, threshold current density, maximum current density, output optical power, lasing frequency, differential resistance at threshold, intermediate resonant current before threshold, and $k_B T/\hbar\omega$ factor will be compared. We could improve the $k_B T/\hbar\omega$ factor of the 3P-QCL design from 0.9 in first iteration to 1.3 and the output optical power of the structure from 0.9 mW in first design to 3.4 mW. The performance of the structure in terms of intermediate resonant current and the change in differential resistance at threshold was improved.

Acknowledgements

I would like to thank my supervisor Prof. Dayan Ban for his encouragement, knowledge, patience and never ending enthusiasm throughout my PhD studies. I want to express my gratitude to the members of my PhD committee: Prof. Xiupu (John) Zhang, Prof. Qing-Bin Lu, Prof. Amir Hamed Majedi, and Prof. Simarjeet Saini, for reading my thesis and helpful discussions.

I would like to express my thanks to our collaborators in National Research Council of Canada, specially Dr. Emmanuel Dupont for helpful stimulating discussions. This work would not have been possible without the help and support of Dr. Emmanuel Dupont. I would like to also thank Prof. Zbigniew Wasilewsk and Mr. Sylvain Laframboise who also helped me through this project.

I would like to express my thanks to my colleagues Saeed Fathololoumi, Jun Chen, Rudra Dhar, Chao Xu, Simon Ferre, and Mark Ferguson for the interesting discussions and talks.

I also want to express my gratitude to all my friends who supported me, including but not limited to Babak, Hossein, Siamak, Akbar, Ehsan, Reza, Aidin, Mohsen, Mehrbod, Shahed, Hadi, Javad, Behnood, Payam, Saman, and Moein. I really enjoyed their company and help during the time spent with them.

Last but not least, I would like to acknowledge the endless love and support from my family.

Dedication

To my beloved wife, *Zahra*,

and

to my parents.

Table of Contents

List of Tables	x
List of Figures	xi
List of Abbreviations	xx
1 Introduction	1
1.1 THz Applications	2
1.2 THz Sources	6
1.3 Quantum Cascade Lasers (QCLs)	10
1.4 QCL Active Region	12
1.5 QCL Waveguide Design	13
1.6 Active region design trend	16
1.7 Research objectives	19
1.8 Thesis organization	20
2 Waveguide analysis and scattering mechanism	22
2.1 Waveguide Design of THz QCLs	23
2.1.1 Loss Mechanisms	23
2.1.2 Free carrier absorption loss	23
2.1.3 Facet coupling loss	24

2.1.3.1	Effective index method	24
2.1.3.2	Impedance mismatch method	25
2.1.4	Confinement factor	25
2.1.5	Threshold Gain	25
2.1.6	Semi-Insulating Surface Plasmon versus Metal-Metal THz waveguides	26
2.1.6.1	Semi-Insulating-Surface-Plasmon waveguide	26
2.1.6.2	Metal-Metal Waveguide	28
2.1.6.3	Waveguide comparison	29
2.1.7	M-M waveguide	30
2.1.7.1	Top metal gap effect	30
2.1.7.2	Effect of metal on temperature performance of THz QCL .	34
2.2	Quantum Design of THz QCLs	37
2.2.1	Energy state and wavefunction calculation	37
2.2.2	Band structure of a Terahertz quantum cascade laser	39
2.2.3	Main parameters of the transport model	41
2.2.4	Tight binding parameters, detuning and coupling	41
2.2.5	Scattering time calculation	43
2.2.5.1	Intersubband and Intracubband scattering time	43
2.2.5.2	Intersubband scattering time	44
2.2.5.3	Intracubband scattering time	45
2.2.5.4	Longitudinal optical phonon scattering time	45
2.2.5.5	Interface Roughness Scattering	49
2.2.5.6	Ionized impurity scattering	50
2.2.5.7	Dephasing time calculation	51
2.2.6	Oscillator strength calculation	52
2.3	Measurement setup	54
2.3.1	Light-current density-voltage (LJV) setup	54
2.3.2	Spectrum measurement setup	55
2.4	Summary	56

3	Transport Modeling of Indirectly-Pumped Terahertz Quantum Cascade Laser	57
3.1	Rate equation model	57
3.2	Simplified model for an IDP QCL	58
3.3	Implemented rate equation model for IDP structures	63
3.4	Current density calculation	65
3.4.1	Resonant tunneling in a two level system	66
3.4.2	First-order current density calculation	67
3.4.3	Second-order current density calculation	68
3.5	Gain calculation in IDP THz QCLs	69
3.6	Summary	71
4	Design and Analysis of Indirectly-pumped THz QCLs	72
4.1	Design of THz IDP-QCLs	72
4.1.1	New design concerns	73
4.1.2	General parameters of 3P QCL design	74
4.1.2.1	Growth material	75
4.1.2.2	Alignment electric field	75
4.1.2.3	Doping concentration	75
4.2	First 3P-QCL design (V843)	76
4.2.1	Numerical simulation of V843	77
4.2.2	Experimental results	79
4.3	Second 3P-QCL design (V845)	86
4.3.1	Numerical simulation of V845	88
4.4	Experimental results of V845	90
4.5	Third 3P-QCL design (V962)	96
4.5.1	Numerical simulation of V962	98
4.6	Experimental results of V962	100

4.7	Analysis and Comparison of V843, V845, and V962	104
4.7.1	Electrical characteristics	105
4.7.2	Differential resistance at threshold	107
4.7.3	Comparing the main specification of V843, V845, and V962	109
4.8	Summary	112
5	Conclusion and future works	113
5.1	Summary and conclusion	113
5.2	Future works	116
	References	117

List of Tables

2.1	Scattering times, effective masses, doping concentration, and core permittivities used in THz numerical simulations.	24
4.1	Main specifications of each design extracted from experiment (device A) and simulation result are presented.	110

List of Figures

1.1	Electromagnetic spectrum shows the terahertz frequency between microwaves and near-/mid-infrared range. Adopted from [3].	1
1.2	Radiated energy versus wavelength from a 30-K blackbody. The spectrum includes dust continuum, molecular rotation line and atomic fine-structure line emissions [11].	4
1.3	(a) Atmospheric attenuation of THz waves in the range of 0.13 THz and nine major THz transmission bands. A: 0.1055 THz; B: 0.56075 THz; C: 0.76098 THz; D: 0.99109 THz; E: 1.21141 THz; F: 1.42159 THz; G: 1.92204 THz; H: 2.05215 THz; I: 2.47262 THz. The temperature of the measurements was 23 °C , and the relative humidity was 26%. Adopted from [14]. b) Terahertz images of a living leaf on a plant. Left picture was taken when the leaf was starved of water for several days and right image was only taken several tens of minutes after watering. The water distribution in the right image is much more uniform, indicating a dynamic uptake of water. Adopted from [13].	5
1.4	THz-emission power as a function of frequency for different THz sources. IMPATT diode stands for impact ionization avalanche transit-time diode, MMIC stands for microwave monolithic integrated circuit, TUNNET stands for tunnel injection transit time and the multiplexer is an SBD frequency multiplier and Ovals denote recent THz sources [12].	7
1.5	First observation of sequential resonant-tunneling in a semiconductor ($\text{In}_{0.53}\text{Ga}_{0.47}\text{As}/\text{In}_{0.52}\text{Al}_{0.48}\text{As}$) superlattice with 35 periods [32]. Conduction band schematics corresponding to two different bias points in the I-V are shown. The I-V shown here is a qualitative sketch of the measured I-V in [32]. . .	9

1.6	Conduction band diagram and magnitude squared wavefunctions for the first intersubband laser in a semiconductor ($\text{In}_{0.53}\text{Ga}_{0.47}\text{As}/\text{In}_{0.52}\text{Al}_{0.48}\text{As}$) superlattice with 25 periods. Adopted from [31]	11
1.7	Conduction-band diagrams for major terahertz QC design schemes. Examples are shown for: a) CSL, b) BTC, c) RP and d) hybrid/interlaced designs [2].	14
1.8	Schematic of terahertz QCL waveguides. a) The structure of a SISP-QCL and the corresponding mode profile . b) the structure of a M-M structure and the corresponding mode profile.	15
2.1	Schematic of the cross-section of an SISP waveguides geometry.	27
2.2	Schematic of the cross-section of an MM waveguides geometry.	28
2.3	Schematic presentation of the simulated MM THz QCL structure. The laser ridge width and the metal gap distance vary for simulating different waveguide mode allocations. a) no metal gap, b) variable metal gap	30
2.4	a) The total loss of M-M waveguide for 100 and 150 μm width in different metal gap. b) The power intensity of M-M waveguide for the first three TM modes	31
2.5	The collected THz light (optical output power) versus current curves for MM THz QCLs with a) no metal gap, c) 5 μm metal gap and 90 μm ridge width and d) 5 μm metal gap and 150 μm ridge width and 1 mm length at different heat sink temperatures. The device is fabricated using Pd/Ge/Ti/Pt/Au metal contacts and is biased in pulsed mode (pulse width = 200 ns, repetition rate = 1 kHz). The SEM of this waveguide is also shown in b.	32
2.6	Calculated waveguide losses of THz QCLs with different metal claddings. The curves from the top to the bottom correspond to metal claddings made of Pd/Ge/Ti/Pt/Au, Ti/Pt/Au, Ti/Au and Ta/Cu/Au. The waveguide losses increase with temperature for all cases. The device with a metal cladding made of Ta/Cu/Au has the lowest waveguide loss. The right vertical axis shows the simulated optical gain based on a simplified density matrix model [55], which includes intersubband LO-phonon, ionized impurity and interface roughness scatterings. At T_{max} (136, 146, 170, 172 K) the disagreement between the simulated waveguide loss and optical gain is represented by the vertical double arrows. This disagreement could be explained by the inaccuracy of the models used for optical gain and waveguide loss, as well as waveguide imperfections.	36

2.7	The block diagram of the numerical calculation of THz QCLs.	38
2.8	Conduction band diagram and the moduli squared of wavefunctions of the THz IDP-QCL, V843 [60], at a) 0 kV/cm and b) alignment electric field (21 kV/cm). The first for states of each module labeled by e , 1 , 2 , and i	40
2.9	The detuning and the coupling strength between different states of the structure presented in [60]. The detuning between two states at their alignment electric field is zero. The coupling strength will affect the tunneling time when the detuning is minimum. Δ and Ω are detuning and coupling between different states, respectively.	42
2.10	a) Intersubband b) Intraband scattering from the initial wave-vector k to a final wave-vector k' . Both Intersubband and Intraband scattering can be elastic or inelastic.	44
2.11	The intersubband LO-phonon scattering of the carrier. a) LO-phonon emission when the energy spacing between two subbands is less than the LO-phonon energy. b) LO-phonon absorption when the energy spacing between two subbands is less than the LO-phonon energy. c) LO-phonon emission when the energy spacing between two subbands is higher than the LO-phonon energy. d) LO-phonon absorption when the energy spacing between two subbands is higher than the LO-phonon energy.	46
2.12	Schematic diagram of characterization setup for QCL LJV measurements.	53
2.13	Schematic diagram of characterization setup for QCL spectroscopy measurement.	55
3.1	Schematic diagram of an IDP QCL active region based on a phonon-photon-phonon configuration. Throughout this thesis and whatever the electric field, the states within a module are labeled in energy ascending order e , 1 , 2 , and i . The solid lines show the forward scatterings, while the dashed lines indicate the back scatterings. Δ and Ω are the detuning and the coupling between two states, respectively. The green lines indicate the correct injection and extraction, while the red lines show the wrong injection and extraction in each module. 2 and 1 are the ULS and LLS, respectively.	59

3.2	Schematic diagram of three cascade IDP QCL active region based on a phonon-photon-phonon configuration. The main coupling between states are indicated in figure. The green arrows and the red arrows show the desired and undesired coupling strength, respectively. Even though the coupling between all 6 states of the left module and all 6 state of the middle and right module were included in our RE model, the main coupling which drastically affect the current density and the gain are plotted. Ω and Δ are the coupling strength and detuning energy between states.	64
3.3	Schematic diagram of a two-level system. Δ and Ω are the detuning energy and the coupling strength between states 1_n and 2_{n+1} . τ is the non-lasing transition lifetime of level 2_n . T is the tunneling time between states 1_n and 2_{n+1}	65
3.4	Different tunneling cases in two-level system. if the detuning energy is negative, only small fraction of electrons in state a which have enough kinetic energy (the red circles) can contribute in tunneling from state a to b and electrons with low kinetic energy (the blue circles) have no permission to tunnel, while all electron in state b (the green circles) have this opportunity to tunnel to state a . If the detuning energy is positive, all electrons from state a can tunnel to the states b while only hot electrons in state b contribute in tunneling mechanism from state b to a	70
4.1	Conduction band diagram and the moduli squared of wavefunctions of the THz 3P-QCL, V843, at 21 kV/cm. The “+” signs denote the position of Si doping in each module. The intersubband lifetimes by LO-phonon emission are given at the resonant in-plane kinetic energy.[60]	78
4.2	The 4-level RE simulation results of V843. (a) Different characteristic times at 20 K ($T_e = 70$ K, thick blue lines) and 150 K ($T_e = 200$ K, thin red lines). The scattering time presented in figure are defined as follows: τ_{tun} is tunneling time (solid line), $\tau_{\text{tr}}^<$ (dot line) and $\tau_{\text{tr}}^>$ (dash dot line) are the transit times—excluding the tunneling time—across the four wells before and after threshold, respectively; τ_i is injection state lifetime (dash line); and $\tilde{\tau}_{2\text{eff}}$ is the <i>modified</i> effective lifetime (dash dot dot line). (b) Normalized populations of the four states at 20 K (thick blue lines) and 150 K (thin red lines) lattice temperatures and the population inversion ($n_2 - n_1$) at 20 K (blue solid circles) and 150 K (red solid circles), (c) Current density, lasing frequency (dashed line), and optical gain-bandwidth product vs electric field at 20 and 150 K lattice temperatures.	80

4.3	Left axis: The bias voltage of THz 3P-QCL V843 versus the current density, a) Device A b) Device B. Right axis: Collected THz light (optical output power) versus current density at different heat sink temperatures. Since the measurement set-up and the waveguide properties are different, the collected light, and the maximum current density, are different in plots a) and b). Drop voltage on device B is higher than on device A, the latter having the top 100 nm n ⁺ contact GaAs layer hence, a top Schottky contact with a short depleted region (~18 nm).	81
4.4	Conduction band diagram and the moduli squared of wavefunctions of V843 at a) 4.4 kV/cm and b) 8.7 kV/cm. States in left module (upstream), middle module, and right module (downstream) are represented by subscripts $n - 1$, n , and $n + 1$, respectively. The extraction state (e) of each module is in resonance with states 1 and 2 of next module at electric fields of 4.4 kV/cm and 8.7 kV/cm, respectively.	83
4.5	THz spectra recorded for different biases and temperatures. The current density, the applied voltage bias, and voltage drop per module are reported in the figure. Spectrum at 141 K was collected from device B while all other spectra were measured from device A.	85
4.6	Conduction band diagram and the moduli squared of wavefunctions of the THz 3P-QCL, V845, at 21 kV/cm. The “+” signs denote the position of Si doping in each module. The intersubband lifetimes by LO-phonon emission are given at the resonant in-plane kinetic energy.	87
4.7	The 4-level RE simulation results of the structure presented in Fig. 4.6. (a) Different characteristic times at 20 K ($T_e = 70$ K, thick blue lines). The scattering time presented in figure are defined as follows: τ_{tun} is tunneling time (solid line), $\tau_{\text{tr}}^<$ (dot line) and $\tau_{\text{tr}}^>$ (dash dot line) are the transit times—excluding the tunneling time—across the four wells before and after threshold, respectively; τ_i is injection state lifetime (dash line); and $\tilde{\tau}_{2\text{eff}}$ is the <i>modified</i> effective lifetime (dash dot dot line). (b) Normalized populations of the four states at 20 K (thick blue lines) and 150 K (thin red lines) lattice temperatures and the population inversion ($n_2 - n_1$) at 20 K (blue solid circles) and 150 K (red solid circles), (c) Current density, lasing frequency (dashed line), and optical gain-bandwidth product vs electric field at 20 and 150 K lattice temperatures.	89

4.8	Left axis: The bias voltage of THz 3P-QCL V845 versus the current density, a) Device A b) Device B. The short vertical arrows show the change in the slope of the V-J curves at laser threshold and the lowest temperature (10 K for device A or 7.8 K for device B). Right axis: Collected THz light (optical output power) versus current density at different heat sink temperatures. Since the measurement set-up and the waveguide properties are different, the collected light, the maximum current density, and the threshold current are different in plots a) and b). Drop voltage on device B is higher than on device A, the latter having the top 100 nm n ⁺ contact GaAs layer.	92
4.9	Conduction band diagram and the moduli squared of wavefunctions of V845 at 7.7 kV/cm. States in left module (upstream), middle module, and right module (downstream) are represented by subscripts $n - 1$, n , and $n + 1$, respectively. The extraction state (e) of each module is in resonance with state (l) of next module at an electric field of 7.7 kV/cm.	94
4.10	THz spectra recorded for different biases and temperatures. The current density, the applied voltage bias, and voltage drop per module are reported in the figure. Spectrum at 150 K was collected from device B while all other spectra were measured from device A.	95
4.11	Conduction band diagram and the moduli squared of wavefunctions of a 3P THz QCL at 21 kV/cm. The quantum structure started with an injector barrier are 35 /48/ 8 /38.9/ 9 /72/ 27 /85.6/ 5 /66 Å, where the bold font indicates the barrier. The center 20 Å of the 48 Å first well after the injector barrier is doped with Si to $1.5 \times 10^{17} \text{ cm}^{-3}$ to give a two-dimensional carrier concentration of $3 \times 10^{10} \text{ cm}^{-2}$ per module. The intersubband lifetimes through LO phonon emission are given at the resonant in-plane kinetic energy. 97	97

4.12	The 4-level RE simulation results of the structure presented in Fig. 4.11. (a) Different characteristic times at 20 K ($T_e = 70$ K, thick blue lines) and 150 K ($T_e = 200$ K, thin red lines) . The scattering time presented in figure are defined as follows: τ_{tun} is tunneling time (solid line), $\tau_{\text{tr}}^<$ (dot line) and $\tau_{\text{tr}}^>$ (dash dot line) are the transit times—excluding the tunneling time—across the four wells before and after threshold, respectively; τ_i is injection state lifetime (dash line); and $\tilde{\tau}_{2\text{eff}}$ is the <i>modified</i> effective lifetime (dash dot dot line). (b) Normalized populations of the four states at 20 K (thick blue lines) and 150 K (thin red lines) lattice temperatures and the population inversion ($n_2 - n_1$) at 20 K (blue solid circles) and 150 K (red solid circles), (c) Current density of four-level system, lasing frequency (dashed line), and optical gain-bandwidth product vs electric field at 20 and 150 K lattice temperatures.	99
4.13	Left axis: The bias voltage of five-well THz 3P-QCL (V962) with a Au-Au waveguide versus the current density of the lasing (solid lines) at 4 K and non-lasing (dashed line) at 9 K, 90 K, and 140 K. The width and the length of the lasing device are 144 μm and 831 μm , respectively. The short vertical arrows show the change in the slope of the V-J curves at laser threshold. Right axis: Collected THz light (optical output power) versus current density of device A (9 K to 144 K) and device B (151 K).	101
4.14	Conduction band diagram and the moduli squared of wavefunctions of 3P THz QCL at 6.4 kV/cm. States in left module (upstream), middle module, and right module (downstream) represent by n-1, n, and n+1, respectively. The extraction state (e_{n-1}) of each module is in resonance with state (1_{n+1}) of two-next module at electric field of 6.4 kV/cm.	103
4.15	THz spectra recorded for different biases and temperatures. The spectrum at 10 K and a current density higher than 2 kA/cm ² shows that this IDP structure works as a wideband source.	104
4.16	The current density vs the electric field of a) V843, b) V845, and c) V962. The red curve shows the simulation results based of RE formalism with second-order tunneling. The green dots show depict the experimental results of the lasing device. The black solid line represents the leakage currents from the wrong extraction $2-e$	106

4.17 The differential resistance of a) V845 and b) V962. Left axis: The differential resistance of non-lasing (the red dashed line) and lasing (solid lines with symbols) device A versus current density at different temperatures. The L-J measurement results are also plotted (right scale) to determine the threshold current at each temperature. 108

List of Abbreviations

3P	phonon-photon-phonon
BTC	band-to-continuum
CSL	chirped superlattice
CW	continuous wave
FTIR	Fourier-transform infrared
FWHM	full-width-half-maximum
GA	genetic algorithm
IDP	indirectly-pumped
IR	interface roughness
J-V	current density-voltage
L-J	light-current density
LLS	lower lasing state
LO	longitudinal optical
LT	low-temperature
MM	metal-metal
MQW	multiple quantum-well
NDR	negative differential resistance

NEGF	nonequilibrium Greens function
QCL	quantum cascade lasers
RE	rate equation
RF	Radio Frequency
RP	resonant-phonon
SISP	semi-insulating surface-plasmon
SL	superlattice
THz	Terahertz
TM	transverse mode
TMM	Transfer Matrix Method
ULS	upper lasing state

Chapter 1

Introduction

The far-infrared radiation range is roughly defined as $30 - 300 \sim \mu\text{m}$ in wavelength or 4-40 meV in photon energy. Since 4-40 meV corresponds to 1-10 THz in frequency, this range is also called terahertz (THz) frequency. The THz frequency is between two ranges of frequencies (Radio Frequency (RF)/microwave and infrared/visible light) which are typically generated by electronic circuits and photonic technologies, respectively [1, 2]. Due to the progress of component development and potential applications, THz technology has been attracting significant interests. Figure 1.1 shows the electromagnetic spectrum, illustrating the wavelength and frequency of the THz range.

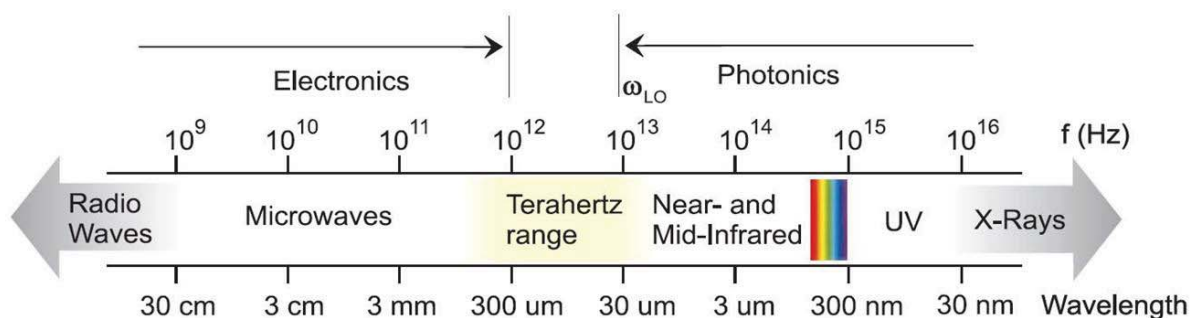


Figure 1.1: Electromagnetic spectrum shows the terahertz frequency between microwaves and near-/mid-infrared range. Adopted from [3].

Some important applications of this range include terahertz imaging and terahertz

spectroscopy, remote sensing and monitoring of earth's atmosphere, biomedical imaging, detection of concealed weapons and drugs, end-point detection in plasma-etching processes, free-space optical wireless communications and non-invasive inspection of semiconductor wafers [1]. In recent years, the generation, propagation and detection of terahertz electromagnetic radiation using two-dimensional semiconductor systems or other semiconductor nanostructures has become one of the most rapidly expanding fields in the photonics, optoelectronics and condensed matter physics communities. Lack of compact, coherent, low-cost radiation sources impedes the development of terahertz technology. The scientifically important spectral range from 1-10 THz is inaccessible to conventional semiconductor devices. The semiconductor THz quantum cascade lasers (QCLs) as a compact and coherent terahertz source was first demonstrated in 2002 by Kohler *et. al* [4]. Their large dynamic range, excellent sensitivity, and fail-safe operation combined with the solid-state reliability should easily overcome many of the technological hurdles that impede existing technology in these markets. In this thesis, a new quantum-well active-region design for high-performance THz QCLs is studied theoretically and experimentally. A comprehensive numerical approach is established for designing and simulating the THz QCLs. A series of novel THz QCLs based on an indirectly-pumped scheme have been grown and fabricated and characterized.

1.1 THz Applications

The oldest and main application involving terahertz radiation is spectroscopy. Since many chemical species have very strong characteristic rotational and vibrational absorption lines in terahertz region, this range has long been of scientific interest [5, 6]. The typical absorption strengths in THz frequency are $10^3 - 10^6$ stronger than in the microwave region. Spectroscopy was principally performed with incoherent thermal sources and Fourier-transform infrared (FTIR) spectrometers using cryogenic bolometric detection [6]. This measurement becomes difficult at frequencies below 1 THz ($\lambda > 300 \mu m$), and long mirror travel lengths were inconveniently required to reach the high-resolution spectroscopy. As a result, heterodyne spectroscopy becomes dominant for low frequencies, in which continuous-wave (CW) coherent THz sources are employed. In this heterodyne spectroscopy technique, an input signal in THz frequencies is mixed with a local THz oscillator signal and is down-converted to an intermediate frequency (typically in RF/microwave range) where it can easily be amplified and processed. Active spectroscopy can be also possible, where tunable narrow-band terahertz radiation is detected after transmission or reflection through a medium. Contrary to passive detection which does not need any source, in the active

method a narrow-band source is mandatory.

Since around one-half of the total luminosity of the galaxy fall into the terahertz range, the astronomical and space science community have been more interested in terahertz spectroscopy. Cool interstellar dust inside our own and in other galaxies contributes most of this radiation [7]. A schematic of some important resonances in interstellar dust as well as comparable blackbody curves is shown in Figure 1.2. This graph shows the radiated power of these materials versus wavelength. Due to the strong atmospheric absorption that results from pressure broadened water and oxygen lines, most terahertz astronomy must be performed on satellite platforms or at high altitude. The Wave Astronomy Satellite (SWAS) launched 1998 and the satellite Herschel (formerly known as the Far-Infrared and Submillimeter space Telescope (FIRST)) launched May 14th 2009 are some of such satellites [8]. Herschel includes a heterodyne instrument that provides coverage from 480 GHz to 1.25 THz in five bands and 1.41 THz to 1.91 THz in two bands.

Another area of interest for terahertz spectroscopy is atmospheric science. Terahertz spectroscopy is used for detecting the thermal emission from gasses in the stratosphere and upper troposphere such as water, oxygen, chlorine, and nitrogen compounds. Data obtained from this spectroscopy can be used for the study of chemical processes related to ozone depletion, pollution monitoring, and climate change [1]. The Earth Observing System Aura (EOS-Aura) was launched in July 15th 2004, and included a heterodyne band at 2.5 THz specially for monitoring atmospheric OH levels [1]. The materials which have been monitored by this satellite are cloud, ice and atmospheric chemical species like BrO, CH₃CN, ClO, CO, GP, H₂O, HCl, HCN, HNO₃, HO₂, HOCl, IWC, IWP, N₂O, O₃, OH, RHI and SO₂ [9]. A heterodyne radiometer measures the thermal emission at frequencies of around 118, 190, 240 and 640 GHz and 2.5 THz. The major objectives are to obtain information about ozone chemistry to better understand the climate change, to quantify aspects of how the atmospheric composition affects climate and to study aspects of pollution in the upper troposphere. Another application of terahertz spectroscopy is plasma fusion diagnostics, which measures the temperature profiles of the plasma [10].

In addition to terahertz spectroscopy, the terahertz imaging (so-called T-Ray) is one of most important applications of terahertz waves. For imaging, terahertz radiation is specifically useful since many materials such as paper, plastics, and ceramics, which are opaque at optical frequencies (visible light), are transparent in the terahertz and microwave region. Since THz frequency has a shorter wavelength, terahertz imaging yields a much better spatial resolution comparing to imaging at microwave frequencies. A THz beam can be focused using mirrors or lenses, and the images are obtained by scanning the beam through the objects. The imaging resolution is defined by the beam diameter, which is typically at the order of the THz wavelength (30 – 300 μm). Higher frequency components lead to a

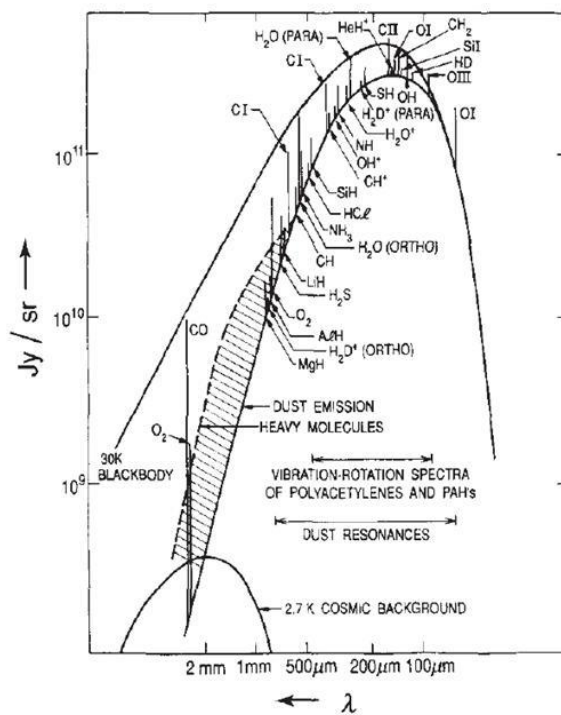


Figure 1.2: Radiated energy versus wavelength from a 30-K blackbody. The spectrum includes dust continuum, molecular rotation line and atomic fine-structure line emissions [11].

better imaging resolution, but it is still not sufficient for nanoscale applications. A wide variety of methods have been attempted to overcome this limitation. Scanning near-field microscopy, with a modulated THz field, is one of the potential imaging systems from which nanometrescale resolution is expected [12]. When compared to imaging with high energy X-rays, imaging with terahertz radiation is non-invasive, environment-friendly to human being and surroundings due to its low photon energy, and can provide much better contrast in terms of identification of different materials due to their different absorption and refraction indices in the terahertz range. Towards this goal, it is worth mentioning that atmospheric water absorption at terahertz frequencies is an important factor of consideration for terahertz imaging over a distance. The frequency band of 1.3 – 1.5 THz is very attractive for such an application because it offers the lowest atmospheric water absorption in the frequency range of 1 – 5 THz. The atmospheric attenuation in the range of 0.1 – 3 THz is shown in Figure 1.3(a) and nine different transmission windows throughout this range are indicated. Monitoring of water levels in plants(see Figure 1.3(b)), fat content in packaged meats, and manufacturing defects in automotive dashboards and high voltage cables have all been performed by THz imaging [13].

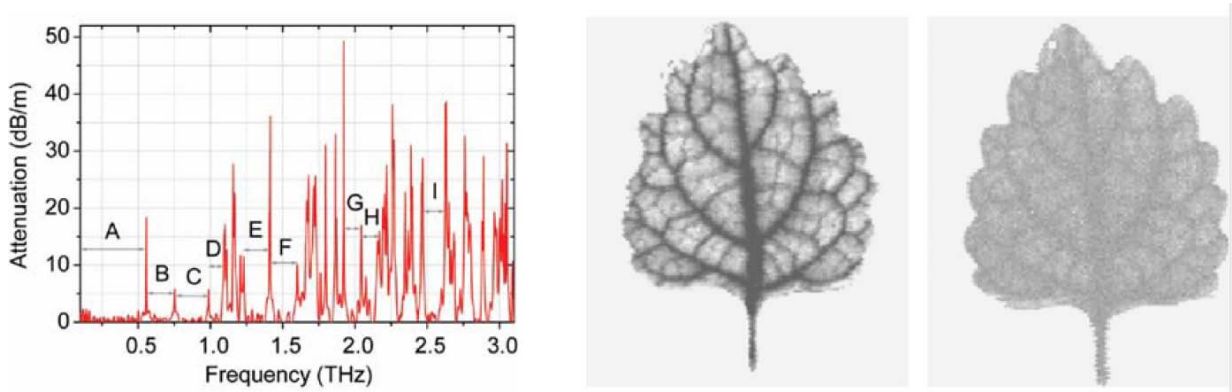


Figure 1.3: (a) Atmospheric attenuation of THz waves in the range of 0.13 THz and nine major THz transmission bands. A: 0.10.55 THz; B: 0.560.75 THz; C: 0.760.98 THz; D: 0.991.09 THz; E: 1.211.41 THz; F: 1.421.59 THz; G: 1.922.04 THz; H: 2.052.15 THz; I: 2.472.62 THz. The temperature of the measurements was 23 °C , and the relative humidity was 26%. Adopted from [14]. b) Terahertz images of a living leaf on a plant. Left picture was taken when the leaf was starved of water for several days and right image was only taken several tens of minutes after watering. The water distribution in the right image is much more uniform, indicating a dynamic uptake of water. Adopted from [13].

1.2 THz Sources

Early far-infrared spectroscopy generally used thermal blackbody sources as light sources. Due to the low-power, incoherent, and broadband nature of the radiation available by this method, the development of efficient coherent sources has long been desired. There are three major approaches in the development of THz sources. The first is optical THz generation [15, 16], which has spearheaded THz research for the past few decades. The second is the recently developed THz-QCL, which is still under development. The third is based on solid-state electronic devices, which are already well established at low frequencies [12]. There are two general categories for optical generation of THz radiation using lasers, either pulsed or CW. The first involves generating an ultrafast photocurrent in a photoconductive switch or semiconductor using electric-field carrier acceleration or the photo-Dember effect. In the second category, THz waves are generated by nonlinear optical effects such as optical rectification (limited to femto second (fs) laser excitation), difference-frequency generation (DFG) or optical parametric oscillation. Dupont *et al.* demonstrated THz coherent waves at room in GaAs/AlGaAs asymmetric quantum wells by mixing two CO₂ laser beams [17]. Recently two groups are actively working on generation of THz wave stacking two IR QCL and DFG technique [18, 19, 20, 21, 22, 23, 24]. Both groups could reach a device which can generate THz wave at room temperature while the maximum optical power is limited to 120 μW [19] and 215 μW [18]. The commonly-used nonlinear media include GaAs, GaSe, GaP, ZnTe, CdTe, DAST (diethylaminosulfurtetrafluoride) and LiNbO₃, although research to find more effective materials continues [12]. Figure 1.4 shows THz-emission power as a function of frequency for various generation technologies.

Generation of coherent terahertz radiation has traditionally involved either extending electronic techniques to higher frequencies, or extending photonic sources to longer wavelengths. Electronic semiconductor devices have troubles in operating far beyond 100 GHz, as resistive and reactive parasitic as well as transit time limitations result in high-frequency roll-offs. Due to small energy level separations (1 – 10 THz or 4 – 40 meV) for laser sources operating in the terahertz region, to achieve population inversion becomes very difficult. In addition, materials with a band gap of few milli-electron-volts are rare to be found. The most popular method of generating low-frequency terahertz radiation (0.5 – 2 THz) is nonlinear multiplication of a lower frequency oscillator (100 – 200 GHz) by chains of Schottky doublers and triplers [1]. This kind of oscillator produces continuous-wave narrowband power with limited tunability (roughly 10%) and is suitable for use as a local oscillator for mixing. Multiplication is a robust technology and is used as the local oscillator on Herschel to pump various mixers in bands up to 1.9 THz. The main disadvantage of this technique is the rapid reduction of output power with increasing frequency due to

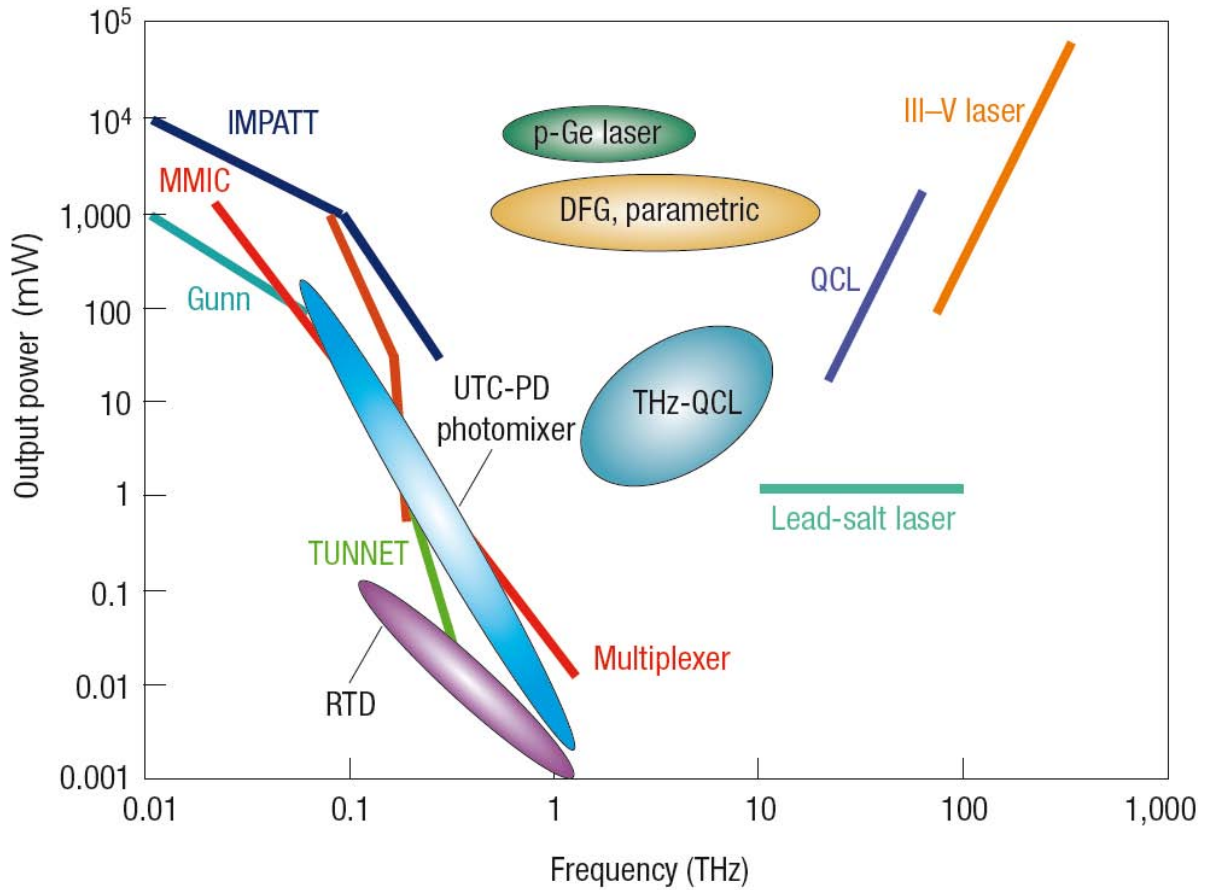


Figure 1.4: THz-emission power as a function of frequency for different THz sources. IMPATT diode stands for impact ionization avalanche transit-time diode, MMIC stands for microwave monolithic integrated circuit, TUNNET stands for tunnel injection transit time and the multiplexer is an SBD frequency multiplier and Ovals denote recent THz sources [12].

reduced multiplication efficiency. Another method for obtaining terahertz radiation is frequency down-conversion from optical sources. The technique of photomixing operates by illuminating a fast photoconductive material with two optical lasers detuned by the desired terahertz frequency. The intensity beating of the lasers modulates the conductivity of the photoconductor, and generates terahertz current flow in a dc-biased antenna. The optical conversion efficiency of this method is also low and power drops with increasing frequency due both to the antenna impedance and limited photoconductive response speed [25].

Another dominant source of far-infrared radiation is the optically pumped gas lasers. Low-pressure molecular gasses are pumped by a CO₂ gas laser to produce lasing between rotational levels of excited vibrational states. Such lasers are readily commercially available, and one is being used as a 2.5 THz local oscillator source in the EOS satellite [26]. The tunability of this laser is extremely limited and the availability of the gasses determines the laser frequency. In addition, such gas lasers are expensive and bulky, which makes them unsuitable for space flight applications [27].

After hot hole intersubband P-Ge and BiSb lasers were realized, semiconductor lasers for THz emission were first introduced in 1984 [28]. There are three important types of P-Ge coherent sources. In the first type, lasing action results from a hole population inversion that is established between the light and heavy hole bands due to a streaming motion that takes place in crossed electric and magnetic fields [29]. The second one is a light-hole cyclotron resonance laser in crossed electric and magnetic fields, and the third one is a negative mass heavy-hole cyclotron resonance maser in parallel electric and magnetic fields [28]. Several watts of peak power have been obtained in broadband lasing (linewidths of 10-20 cm⁻¹) that can be tuned from 1 to 4 THz. The utility of this source is limited by the need for a magnetic field, high voltage, and cryogenic-temperature operation ($T < 20$ K). Because of low efficiency and high power consumption, the device can work only at low duty cycles up to 5% [30].

The most recent development has been the extension of quantum cascade laser (QCL) operation from the mid-infrared to the terahertz. A QCL is an electrically-pumped unipolar photonic device in which light emission takes place due to intersubband optical transitions in two dimensional quantum-wells of a semiconductor heterostructure. This type of a laser was first demonstrated by Faist and co-workers in Federico Capasso's group at Bell Labs [31]. By varying the size of the quantum wells, we can arbitrarily tune determine the energy spacing between the subbands, and hence the frequency of light emission. One key characteristic of QCLs is the use of periodic multiple quantum-well (MQW) modules such that one charge carrier leads to generation of multiple photons as it is transported through the repeated modules. Contrary to other conventional semiconductor lasers, QCLs are based on intersubband transition instead of interband transition.

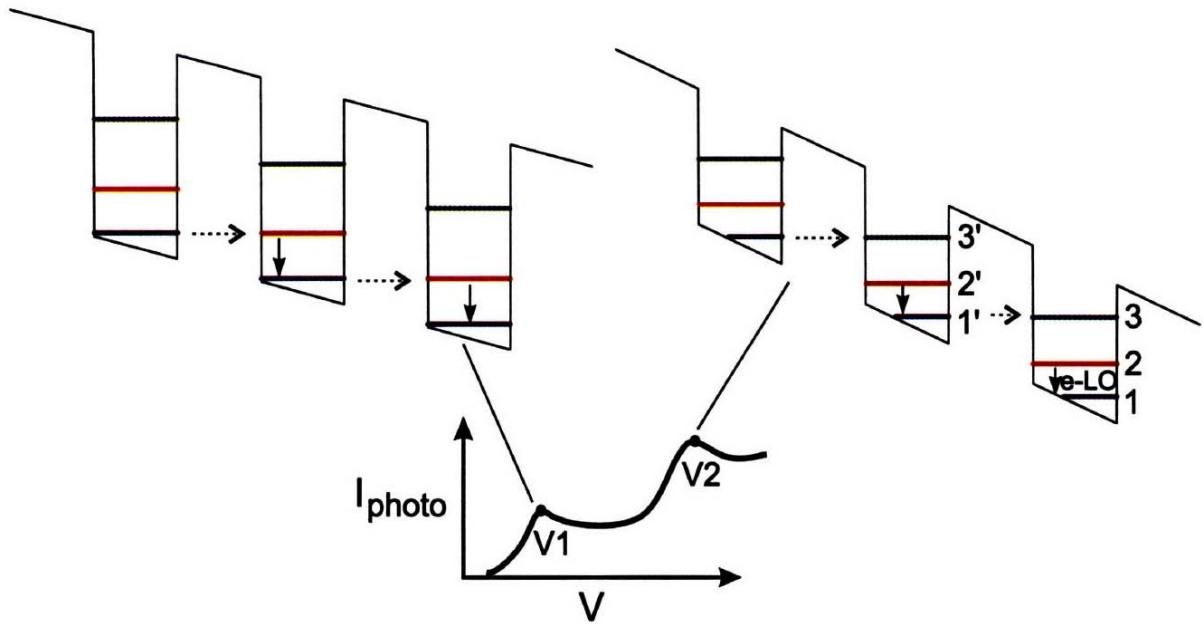


Figure 1.5: First observation of sequential resonant-tunneling in a semiconductor ($\text{In}_{0.53}\text{Ga}_{0.47}\text{As}/\text{In}_{0.52}\text{Al}_{0.48}\text{As}$) superlattice with 35 periods [32]. Conduction band schematics corresponding to two different bias points in the I-V are shown. The I-V shown here is a qualitative sketch of the measured I-V in [32].

1.3 Quantum Cascade Lasers (QCLs)

The original proposal for a QCL originated from the work of R.F. Kazarinov and R.A. Suris [33, 34]. They described a possibility of photon emission by photon assisted tunneling in a superlattice (SL) in strong electric field and analyzed the intersubband transitions in the framework of a Density matrix theory. Unlike Esaki and Tsu in their original proposal of a superlattice [35] they considered a situation when the subbands of the SL are strongly localised in individual levels, i.e. far above the first region of negative differential resistance (NDR). The first superlattice was fabricated by Chang [36] and one year later, Esaki and Chang demonstrated resonant tunneling and the existence of a NDR in a superlattice [37]. The structure, developed by Capasso *et al.* is very important because it is the closet structure to the first superlattice based intersubband laser (i.e. the QCL) that was invented a few years later. In their subsequent paper [38], the authors considered the idea of achieving population inversion between levels 3 and 2 within the same well. At $1' - 3$ resonance (bias point V_2) in Figure 1.5. At the bias of V_2 , the second excited state 3 in a well is selectively populated by the ground state $1'$ of the adjacent well through resonant-tunneling. If a population inversion could be established between levels 3 and 2, stimulated emission is possible through a vertical intrawell radiative transition. Hence, the resonant-tunneling through the barrier no longer needs to be coherent [3].

Since the longitudinal optical (LO) phonon scattering times between levels $3 \rightarrow (2, 1)$ and $2 \rightarrow 1$ are fast, It is not easy to obtained the population inversion in such a scheme [38]. To obtain level spacings corresponding to a large E_{32} , Faist *et al.* [39] developed a structure in which levels 3, 2 and 1 are due to adjacent quantum wells that constitute part of a superlattice period, which is then repeated multiple times to form the whole superlattice. This allows independent control of level spacing by varying the corresponding well widths to obtain $E_{32} > \hbar\omega_{LO}$, as shown in Figure 1.6.

To have a sufficient spatial overlap between the wavefunctions of the levels, the barriers are kept thin. Additionally, a digital-graded alloy, which is essentially a doped multiple quantum-well region, is implemented in the superlattice period. Such a region forms a miniband of levels in the doped region, which helps in extraction of electrons from lower levels 2 and 1 and injects them into the excited state 3 of the next period through resonant-tunneling. The relaxation/injection part is a doped region providing the electron charges needed for the transport. This electron reservoir feeds electrons to the next period and provides a region for electrons thermalization with the lattice. The doping in the active region is generally avoided, to prevent the broadening of the laser transition, introducing a tail of impurity states. In addition, this part limits current flow in the device at fields much lower than the design bias, since the multiple levels in the injector are misaligned

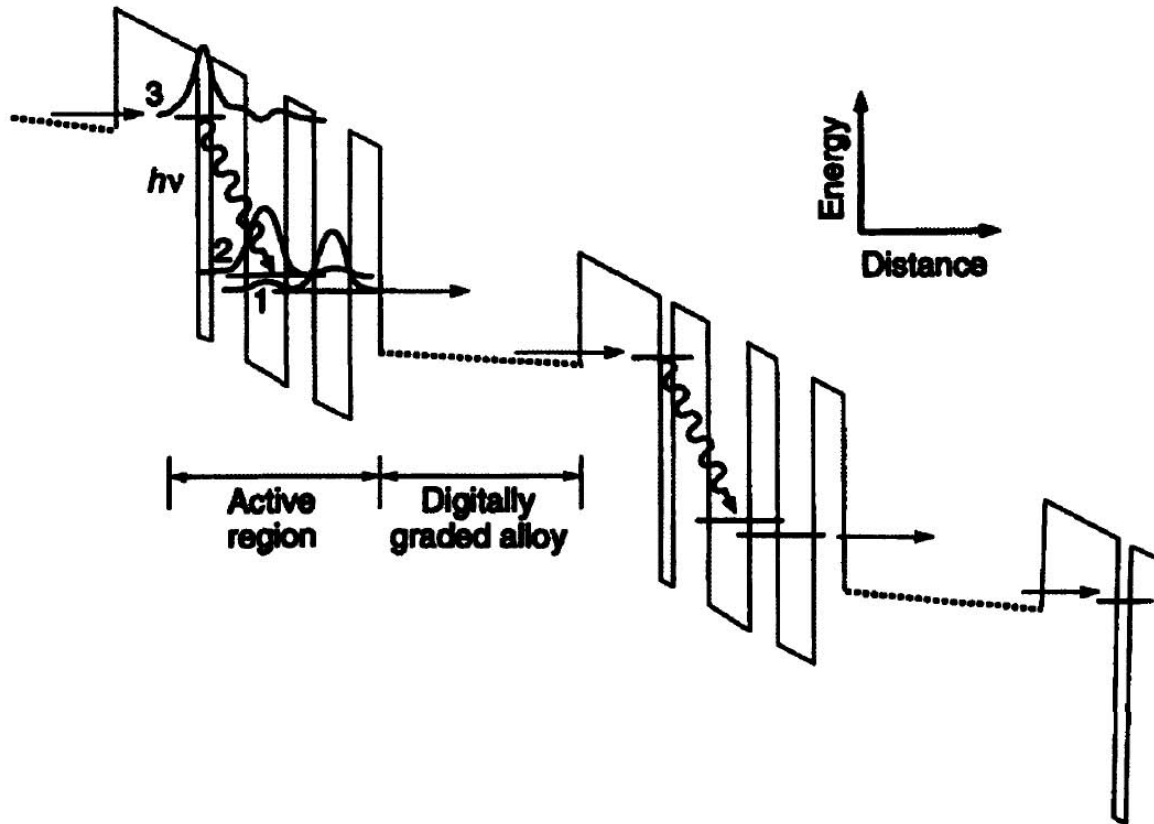


Figure 1.6: Conduction band diagram and magnitude squared wavefunctions for the first intersubband laser in a semiconductor ($\text{In}_{0.53}\text{Ga}_{0.47}\text{As}/\text{In}_{0.52}\text{Al}_{0.48}\text{As}$) superlattice with 25 periods. Adopted from [31]

with respect to each other at lower bias and hence do not conduct current efficiently. This fact suppresses any current conduction channels and the related resonant-tunneling peaks prior to the design bias. This prevents occurrence of a negative differential resistance (NDR) region prior to design bias in the device I-V characteristics, and maximizes current flow in the device at design bias. Finally, a lower static electric field is needed across the superlattice to obtain the desired alignment of levels at the design bias. This is critical to limit the escape time of the electrons from level 3 into the continuum, since level 3 is located close to continuum in the energy space. With the aforementioned design, mid-infrared electroluminescence, and subsequently lasing [38] was obtained for the first time at a wavelength of $4.3 \mu\text{m}$ ($\nu = 70 \text{ THz}$, $\hbar\omega = 290 \text{ meV}$) [3].

1.4 QCL Active Region

The molecular beam epitaxy (MBE) is generally used to grow the multiple-quantum-well active region based on GaAs/ $\text{Al}_x\text{Ga}_{1-x}\text{As}$ material system. Energy levels, wave functions, and scattering rates should be properly engineered to provide population inversion between two states separated by an energy $h\nu$ and guarantee obtaining gain for electromagnetic waves at frequency ν . To have better comparison among different active regions, it is helpful to know that the peak gain for the intersubband transition between level 2 and 1 is $g(\nu_0) \propto \Delta N f_{21} / \Delta\nu$, where $\Delta\nu$ is the transition linewidth, ΔN is the three dimensional intersubband population inversion, and f_{21} (the oscillator strength) is the ratio of the quantum optical strength of the transition to that of a classical electron oscillator. f_{21} depends heavily on the overlap and symmetry of the initial and final wavefunctions. Different active region design scheme are shown in Figure 1.7. The first THz QCL design, demonstrated by Kohler in 2002, is based on chirped superlattice (CSL) structure [4]. After this CSL active region, two major design classes of active regions have emerged: band-to-continuum (BTC) and resonant-phonon (RP) design [2]. As shown in Figure 1.7-a, CSL is based on the coupling of several quantum wells together in the superlattice to create minibands of states when the appropriate electric field is applied. In this active region the radiation takes place when we have a transition between the lowest state of the upper miniband (level 2) to top state of the lower miniband (level 1). In this structure electrons tend to relax quickly to the bottom of the minibands, leaving the lower radiative state (level 1) relatively empty. In CSL the photon will probably be emitted only in the transition between states 2 and 1. Due to relatively small bandwidth of the minibands, LO phonon is not directly involved in the depopulation process.

The BTC structure is similar to CSL, but the upper radiative state is essentially made

to be a bound defect state in the minigap. Comparing with the CSL design, the oscillator strength of the transition drops slightly (from $f_{21} \approx 2.53$ to $f_{21} \approx 1.52$) as the overlap with the miniband states drops, but the upper-state lifetime increases as nonradiative scattering is similarly reduced (Figure 1.7-b). Compared to CSL, this design has better temperature and power performance [2].

Another active region which is commonly used for most mid-infrared QC lasers is the Resonant-Phonon (RP) Scheme. As shown in Figure 1.7-c, in this structure collector and injector states are designed to be below the lower radiative state 1 by approximately $E_{LO} = 36$ meV, so that the electrons in the lower state will scatter very quickly into a injector states by emitting LO-phonons. There is a fundamental difficulty in many early THz QC emitter designs: because of the close subband energy spacing, it was difficult to use LO-phonon scattering to depopulate the lower radiative state without depopulating the upper state too. The key point in the development of the RP scheme was bringing the lower radiative state into a broad tunnelling resonance with the excited state in the adjacent quantum wells, so that its wavefunction is spread over several quantum wells. As a result, the lower radiative state maintains a strong spatial overlap with the injector states and experiences very fast LO-phonon scattering. However, the upper state 2 remains localized and has very little overlap with the injector states, which suppresses scattering to the injector states and preserves a lifetime of several picoseconds. The lack of a miniband causes the RP designs to have a smaller oscillator strength ($f_{21} \approx 0.51$) than the BTC designs, but this is partially compensated by the fact that the length of an RP module is typically half that of a BTC module, which results in a higher density of gain [2]. Active module of a hybrid (interlaced) structure, where phonon-assisted depopulation is combined with the BTC optical transition is shown in Figure 1.7-d. These structures were used to produce longer wavelength radiation [2]

1.5 QCL Waveguide Design

To minimize the overlap of the mode with any doped cladding layers, different waveguides for terahertz QC lasers have been developed. There are two types of waveguides used at present for terahertz QC lasers: the semi-insulating surface-plasmon (SI-SP), and the metal-metal (MM) waveguide, as shown in Figure 1.8. A comprehensive study on laser waveguide to understand the effect of waveguide loss α_ω , confinement factor Γ , which describes the overlap of the mode with the active region, and the mirror loss α_m , which accounts for losses due to optical coupling, is beneficial. At lasing threshold, the modal gain must equal the total losses: $\Gamma g_{th} = \alpha_\omega + \alpha_m$. The mirror loss can be calculated by

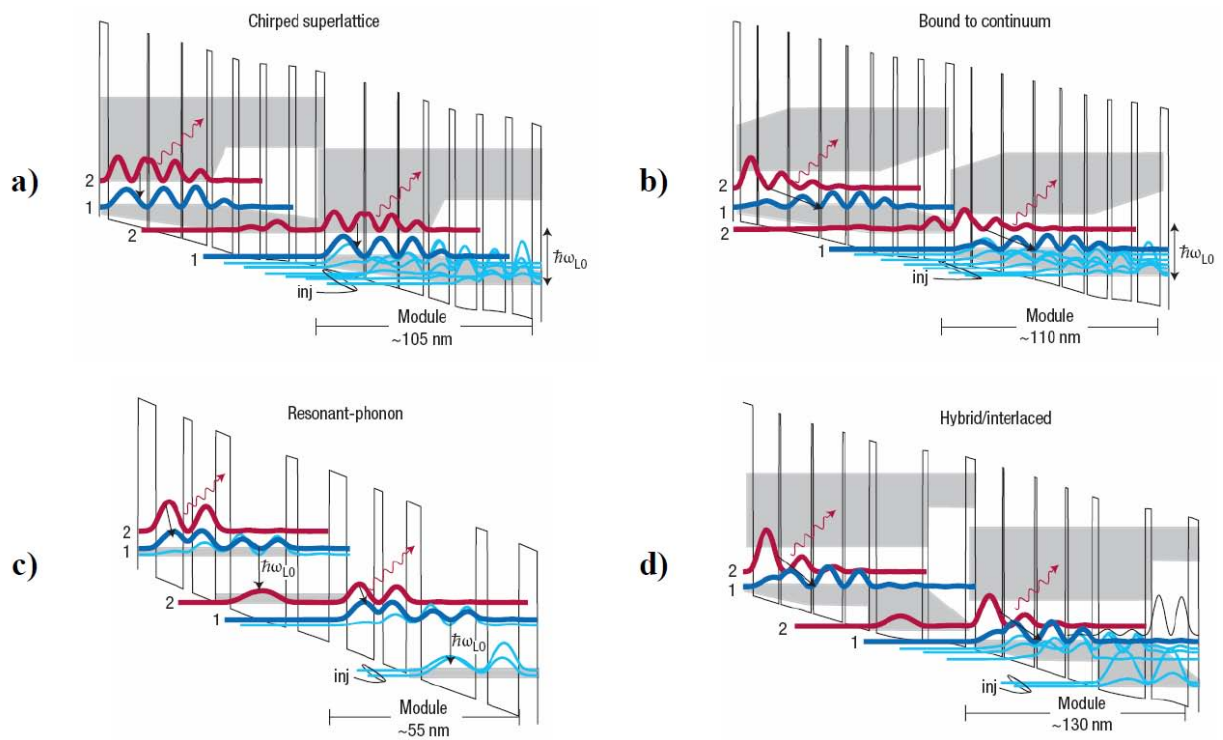


Figure 1.7: Conduction-band diagrams for major terahertz QC design schemes. Examples are shown for: a) CSL, b) BTC, c) RP and d) hybrid/interlaced designs [2].

equation (1.1).

$$\alpha_m = \frac{1}{2L} \ln \frac{1}{R_1 R_2} \quad (1.1)$$

where L , R_1 and R_2 are the length and the reflectivity of each facet of the waveguide. The SI-SP waveguide involves the growth of a thin ($0.2 - 0.8 \mu\text{m}$ thick) heavily doped layer underneath a $10 \mu\text{m}$ -thick active region, but on top of a semi-insulating GaAs substrate. The result is a compound surface-plasmon mode bound to the top metal contact and the lower plasma layer. Although the mode extends substantially into the substrate, the overlap with any doped semiconductor is small, so that the free-carrier loss is minimized [2].

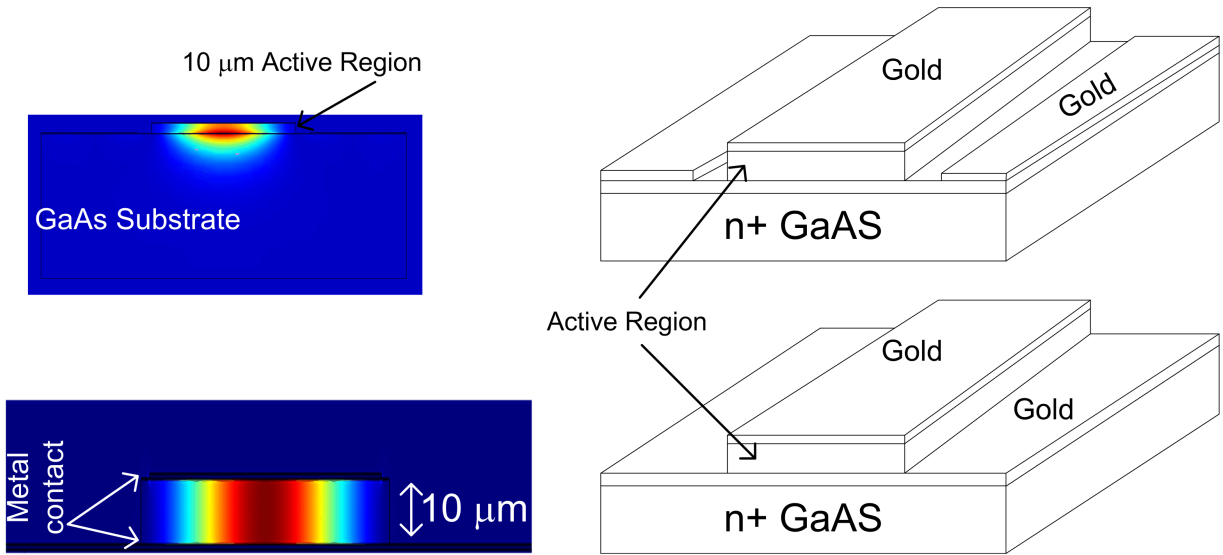


Figure 1.8: Schematic of terahertz QCL waveguides. a) The structure of a SIS-SP-QCL and the corresponding mode profile. b) the structure of a M-M structure and the corresponding mode profile.

The confinement factor typically lies in the range $\Gamma = 0.1 - 0.5$, and in general, modes are somewhat loosely confined. This low confinement factor suppresses excitation of higher lateral modes for relatively wide ridges. The downside is that ridges narrower than about $100 \mu\text{m}$ tend to squeeze the mode into the substrate, which limits the minimum device cross-section area. In contrast to the SI-SP waveguides, the MM waveguide uses metal layers, which are placed immediately above and below the epitaxial active region by metallic wafer-bonding to obtain a mode almost completely confined to the active region ($\Gamma \approx 1$).

After wafer-bonding and substrate removal, the remaining approximately 10 μm thick epitaxial active region is patterned by photolithography and typically etched into ridges to produce a structure similar to a microstrip transmission line. As any doped contact layers are usually quite thin, waveguide losses are dominated by absorption in the metal, and any re-absorption from inside the active region itself (which is often not negligible). At present, the MM waveguides tend to have the best high temperature performance, and the SI-SP waveguides have higher output powers and better beam patterns. Despite their differences in mode confinement, the scaled waveguide loss α_w/Γ , which determines the lasing threshold, is of similar magnitude for both, or even slightly better for MM waveguides. However, because of the impedance mismatch of the sub-wavelength mode at the waveguide facet with free space propagating modes, MM waveguides exhibit enhanced facet reflectivities of $R = 0.5\text{-}0.9$ (depending on the waveguide dimensions as a function of wavelength), which is much higher than the expected Fresnel value of $R = 0.32$ calculated from the index mismatch. As a result, the MM waveguides are characterized by relatively small mirror losses ($1 \sim 2 \text{ cm}^{-1}$), and they often exhibit smaller threshold current densities J_{th} and higher operating temperature [40, 41], although some other groups have observed little difference in J_{th} between the two types [42]. Furthermore, the strong mode confinement of the MM waveguides enables both the vertical and lateral dimensions to be made smaller than the wavelength. This in turn reduces the total thermal dissipation and required cooling power, which enables improved CW operation (up to 117 K [40]).

1.6 Active region design trend

There are some challenging issues in operation of Terahertz QCLs. Firstly, since there is small energy separation between the laser levels, various intersubband scattering mechanisms are activated, and results in difficulty of selectively depopulate the lower laser level. Additionally, as electrons gain enough kinetic energy in the upper laser level thermally activated longitudinal-optical (LO) phonon scattering reduces the level lifetime and makes it difficult to sustain population inversion at higher temperatures. This fact limits the operation of THz QCLs in higher temperature. Several groups around the world are working on different aspects of THz QCL to improve the performance of the device in terms of, maximum operating temperature and output optical power.

The active region design approach depends on the lasing frequency. When the lasing frequency is below 2 THz, injecting carrier to the upper lasing state (ULS) is more challenging since the energy spacing between the ULS and LLS is less than 9 meV. Walther *et. al.* used a BTC structure to design an active region for frequency between 1.2 THz to

1.8 THz [43, 44], while Kumar *et. al.* employed a RP structure [45] and phonon scattering assisted structure [46]. Most of high performance devices whose lasing frequency is higher than 2 THz are based on RP-QCL. The minimum and the maximum lasing frequency of THz QCL without magnetic field are 1.2 THz [44] and 5.2 THz [47], respectively.

The first RP-QCL was demonstrated in 2003 by Williams *et. al.* when each module consists of four wells and barriers [48]. This device was based on two-well injector to reduce the intermediate resonant current to the states below the ULS. In addition the alignment electric field decrease and consequently the injected electrical power will be lowered. The three-well RP-QCL was demonstrated by Luo in 2007 [49]. This structure combined the phonon and injector wells of original four well RP design. This structure is designed to have the oscillator strength in the same range as the original RP scheme design. Three well THz QCL inherits high power and temperature performance of the RP design, but has slightly higher threshold current density. The high current of three-well design is due to inefficient injection of the carriers into upper lasing state and extraction state. The device lased up to 142 K in pulse mode, and no CW operation of this design have been reported so far. Shortly after that, Belkin *et. al.* designed a three-well structure which could lase up to 176 K [50]. The design of this structure was almost the same as the original three-well QCL while the doping concentration was lower. In addition they could reduce the waveguide loss by using the copper bonding process instead of gold.

To improve the performance of this structure, several experimental studies including the injector barrier [51], the extractor barrier [52], and the doping concentration [53] study were done to understand the physics of this structure in detail. Kumar *et. al.* showed that a diagonal design could improve the population inversion of the device at higher temperatures. In 2009, he presented a new diagonal design and improved the maximum operating temperature by 10 K [54]. Even though many groups were working on this design scheme, the maximum operating temperature of three-well QCL did not change for two years. Finally, Fatholouloumi *et. al.* demonstrated a three-well QCL by simultaneously optimizing the injector barrier, the extractor barrier, and the oscillator strength, based on a density matrix model presented in [55], and it lased up to 199.5 K [56]. He designed several active region based on three-well RP structure. Different oscillator strengths were chosen, then the injector and extractor barrier were optimized for each oscillator strength. Experimental results showed that all device have almost the same performance in terms of operating temperature if the cavity loss could be kept low [57].

The limitations of RP-QCLs were addressed by Yasuda *et al.*, [58] Kubis *et al.*, [59] Kumar *et al.*, [46] and Dupont *et al.* [60] Many carriers are stationed in the injector state, ready to be transferred via resonant tunneling to the long-lived, hence heavily populated, upper lasing state (ULS). In this configuration, the bidirectional nature of resonant tunnel-

ing limits the maximum possible population inversion of RP-QCLs to 50%. [61] An efficient injector barrier must be thick enough to suppress wrong carrier injection to the lower lasing state (LLS) or other states lower than ULS and to prevent early negative differential resistance (NDR). On the other hand, it should be thin enough to reduce the tunneling time and increase the maximum current, thereby the dynamic range of the laser. The constraint on the injector barrier becomes even worse when the device lasing frequency approaches 2 THz which corresponds to a photon energy of less than 9 meV. [45] All the aforementioned RP-QCL issues impel designers to find novel approaches to overcome the bottlenecks of THz RP-QCL.

Recently, the indirectly-pumped (IDP) scheme, well implemented in mid-IR QCL, [61] started to be a new design scheme to overcome the limitations of RP-QCLs. To date, several designs based on IDP scheme have been theoretically presented and avowed to have enough gain at higher temperatures to improve the temperature performance and overcome the fundamental limitation of designs based on RP structures. [62, 63, 58] Three groups have demonstrated THz structures based on the IDP scheme, [46, 64, 65, 60] and the best performance THz QCL in terms of $k_B T_{\max}/\hbar\omega$ was achieved in the GaAs/Al_{0.15}Ga_{0.85}As material system by Kumar *et al.* [46]

The structures in the In_{0.53}Ga_{0.47}As/In_{0.52}Al_{0.48}As material system, presented by Yamanishi *et al.*, [64, 66, 65] while not showing the highest operating temperature, exhibited advantages of a high peak output power and smooth current density-voltage (J-V) characteristics with no tunneling resonance before the designed electric field. However, the light-current density characteristics (L-J) showed an optical power roll-over that reduces the temperature performance of the devices. It was proposed that the optical roll-over in power, might come from (i), the excess energy effect of the hot carriers in the injection region and (ii), fast tunneling rate to the next module that could frustrate the thermalization of carriers in the injector. This roll-over effect was not observable in the next generation of IDP structure with an extended tunneling time, which supports this excess energy hypothesis. [66]

So far, several active resign schemes were presented by researchers to overcome the main bottleneck of THz QCL structures, which is the operating temperature. In past decade, the main focus of designers was on optimizing the RP-QCL structure rather than proposing new design scheme. RP-QCLs have some fundamental limitations, addresses in the introduction, which may not be a suitable approach for high performance devices. On the other hand, an IDP-QCL structure were presented based on phonon injection to the upper lasing state. The lower lasing state depopulated through a tunneling followed by phonon scattering mechanism. The performance of one of them was promising [46], but it was not a purely IDP structure. All aforementioned issued encourage us to develop a

new design scheme to overcome those bottlenecks and reach a device with higher operating temperature.

1.7 Research objectives

So far, several active design schemes were presented by researchers to overcome the main limitation of THz QCL structures, which is the operating temperature. In the past decade, the main focus of designers was on optimizing the RP-QCL structure rather than proposing new designs. RP-QCLs have some fundamental limitations, addressed in the introduction, and may not be a suitable approach for high performance devices. On the other hand, all presented IDP-QCL structures which are based on phonon injection to the upper lasing state, depopulate the lower lasing state through tunneling followed by a phonon scattering mechanism. The performance of one structure was promising, but it was not a purely IDP structure. All aforementioned issues encourage us to develop a new design scheme to overcome those limitations and reach a device with a higher performance.

The goal of this project can be separated in three different sections: i) implement a transport model to numerically calculate the most effective parameters in THz QCL; ii) propose a new design scheme to address and hopefully overcome the fundamental limits of RP-QCLs which are the most common active region scheme of the last ten years; iii) design, grow, fabricate, and characterize the proposed scheme to prove the accuracy of our model and the novelty of our proposed lasing scheme.

First, we focus on modeling of THz QCL. Among different transport models, considering the Density Matrix and Rate Equation models, the latter is used to design and predict the performance of THz QCLs. To do so, different intrasubband and intersubband scattering times in quantum well structures are calculated by implementing a MATLAB code. Since this code finally has to be used for an optimization process, we streamline our calculation to be fast and accurate. A reliable model is a key point in the design of a new active region, and it was completed as the first step of our project.

To improve the performance of THz QCL, we are looking for a design which can improve the injection and extraction efficiencies while not compromising population inversion. To this end, we propose a new IDP scheme that injects carrier to the ULS by a phonon scattering mechanism and extracts them from the LLS by a direct phonon mechanism. Contrary to all other IDP structures presented so far, there is no injection/extraction state in our proposed structure to be in resonance with the ULS/LLS. By employing

this simple idea, the broadening of the gain bandwidth due to resonant tunneling can be effectively suppressed. In such a design, we have to optimize all the energy states and the corresponding wavefunctions in one module simultaneously to minimize the wrong injections/extractions and amplify the correct injections/extractions.

Finally, the implementation of different designs based on the IDP scheme will prove that we could predict the behavior of the device and improve the performance of THz QCL. Three generations of this design scheme were implemented during this PhD project. The results presented in this thesis are the payoffs of collaborations between the University of Waterloo (UW), the National Research Council of Canada (NRCC), and the Massachusetts Institute of Technology (MIT), and they demonstrate that this design scheme is a good candidate for future improvement of THz QCLs.

1.8 Thesis organization

The main focus of this thesis is proposing a simple rate equation model to understand the intersubband charge transport and gain in active region. In addition, we investigate different loss mechanisms in two kinds of waveguides. This model helps us to propose a new lasing scheme to overcome the fundamental limits of previous proposed structures. To make our model reliable, we calculate different nonlasing transition times and include them in our model. Finally we grow, fabricate, and characterize our devices and compare their performance, then propose some future improvement for our model and device design strategy. The aforementioned subjects are organized in this thesis as follows.

Chapter 2 discusses some basic parameters which affect the performance of the device either in active region design (quantum design) or in waveguide design. The first section of this chapter explains the resonator part of THz QCLs, which can be further broken up into two main components: a waveguide and mirrors. Different loss mechanisms will be investigated and the method of calculation will be explained. After we present the calculation of waveguide loss, mirror loss, and the confinement factor, the threshold condition will be defined. The effect of top metal gap on suppressing higher modes will be also studied. Based on our loss model calculation, we investigate the effect of different metal on cavity loss of one structure. Since the active region design of all structures are the same, the maximum operating temperature determines which metal process has lower loss. In second section of this chapter, the quantum part of the active region will be addressed. The method that we used to find the energy states and calculate the corresponding wavefunctions introduces, then the tight binding model for calculating the detuning and

coupling between two modules will be commented. In addition, the nonlasing transition time including the LO-phonon , ionized impurity, and interface roughness scattering will be explicated. Finally the oscillator strength and the dephasing time will be defined. All parameters, defined and explained in this section, will be used in our rate equation model.

Chapter 3 presents a rate equation model for carrier transport in our device. We did not make a general model to be used for all design schemes. Since we focus on IDP structures, the presented model can be used for carrier transport of designs based on phonon-photon-phonon scheme independent of number of well and barrier in design. To have better idea about the effect of each scattering time on carrier transport and the gain of the device, a simplified model introduces and those parameters are analytically derived; however in final calculation we do not use the simple analytical model and we include all scattering and leakage passes. The final current density and gain equation are also defined and used in our MATLAB modeling program.

Chapter 4 starts with the design of a new lasing scheme based on phonon-photon-phonon (3P) transition. Since we are proposing a new active region design, the concerns of the design have to be carefully considered and analyzed. First we define the alignment electric field, the doping concentration and the material system to be almost the same for all proposed structures. Different design strategies are used and three active region designs are finally selected to be grown. The wavefunction engineering method is employed to optimize the energy states and the corresponding wavefunctions inside one module. After selecting the design, we evaluate different aspects of the structure at operating electric field and temperatures. We implement the first generation of THz 3P-QCL and characterize it. By carefully analyzing the experimental results and understanding the drawbacks of the first generation, we change our design strategy and propose the second generation of 3P-QCL. Finally the third generation of this lasing scheme will be implemented to improve the performance of the device in terms of optical power and operating temperature. For each design scheme two different fabrication process were used to investigate the effect of lower loss on performance of the device in terms of operating temperature and current density. Finally, we compare different aspects of each device to show the improvements that we reach in each generation.

Chapter 2

Waveguide analysis and scattering mechanism

The design of terahertz quantum cascade lasers can be fairly separated into two fundamental and independent aspects of the laser; the design of the multiple-quantum-well gain medium and the design of the waveguide resonator. The first section of this chapter explains the waveguide resonator, which can be further broken up into two main components: an optical waveguide and cavity feedback mirrors. The waveguide is necessary in order to confine the THz radiation to the gain medium for light amplification. The mirrors are necessary in order to provide optical feedback within the gain medium. The waveguide and mirrors unavoidably contribute optical losses. Waveguide losses (α_ω) are due to the intrinsic lossy electromagnetic properties of the semiconductor materials used in QCLs. Mirror losses (α_m) are due to partial mirror reflectivity and compulsory output coupling mechanism for the laser.

The second section of this chapter discusses a few parameters of the quantum modeling of the gain medium, which consists of multiple semiconductor layers (in the order of 1000) of quantum wells and barriers that are designed in such a way that lasing radiation comes from a selected intersubband transition in the conduction band of the semiconductor heterostructure. A variety of semiconductor gain medium designs have successfully been implemented, including chirped superlattice designs, bound-to-continuum designs, and the resonant-phonon designs [2]. Irrespective of different quantum designs and modeling approaches, general design parameters such as energy states E , wavefunctions ψ , scattering times τ , and oscillator strength f must be calculated. The details of parameter calculation and all assumptions, employed in the calculation, will be explained in this chapter. The key design parameters of the gain medium which affect the resonator design section are

the desired lasing frequency, the doping concentration, and the permittivity of the active region.

The third section of this chapter explains the measurement setup, used in our lab to characterize our devices. The light-current density-voltage and the spectral measurement setup will be separately discussed and the challenging issues will be addressed.

2.1 Waveguide Design of THz QCLs

2.1.1 Loss Mechanisms

To sustain lasing radiation in a laser waveguide, the optical modal gain must overcome the waveguide and the mirror losses of the device. The waveguide losses mechanisms in the THz regime are mainly attributed to free carrier absorption. Absorptive waveguide losses should obviously be kept minimum in order to keep the threshold gain as low as possible. On the other hand, a certain level of the mirror losses should be maintained in order to deliver enough optical output power from the laser facets.

2.1.2 Free carrier absorption loss

Free carrier effects can be modeled by including their contributions to the complex permittivities of active-region materials. Classical Drude theory for permittivity presents the simplest approach for modeling these effects and is described in [67].

$$\epsilon(\omega) = \epsilon_{core}(\omega) + \frac{n_{3D}e^2\tau}{\omega m^*(1 - i\omega\tau)}, \quad (2.1)$$

where $\epsilon_{core}(\omega)$ is the permittivity of the material at given frequency n_{3D} is free carrier density, e is carrier charge, and m^* is electron effective mass.

All simulation in this report are based on material parameter data as shown in Table 2.1 [68]. We first calculate the permittivity of each material in desired frequency, then we insert them in our two-dimensional COMSOL model. The loss can be calculated by having the propagation constant which will be discussed later.

Table 2.1: Scattering times, effective masses, doping concentration, and core permittivities used in THz numerical simulations.

Material	$\tau(fs)$	$m^*(m_e)$	$n(cm^{-3})$	ϵ_{core}
Low doped GaAs	500	0.067	$5 - 8 \times 10^{15}$	12.96
High doped GaAs	100	0.067	$1 - 5 \times 10^{18}$	12.96
Gold	60	1	5.9×10^{18}	1

2.1.3 Facet coupling loss

The cavity facets of THz QCLs are created by cleaving the processed semiconductor monocrystal along a particular crystal plane. This typically leads to atomically-flat planes. The optical mirror loss can be obtained by calculating the reflection and transmission coefficients of the lasing mode at the facets. This loss is then calculated using equation (1.1). There are two different approaches in calculating the reflection coefficients at the facets of the THz QCLs, effective index method and impedance mismatch method.

2.1.3.1 Effective index method

In the regime of optical frequencies (visible and infrared light), the lasing mode is considered, to a good approximation, as a plane-wave and the reflection coefficient at the laser facet is simply given by the Fresnel reflection coefficient, which is determined solely by the effective mode index as shown below:

$$r_{Fresnel} = \frac{n_{eff} - 1}{n_{eff} + 1} \quad (2.2)$$

where n_{eff} is the effective mode index of the device, which can be calculated from the wave propagation constant of the laser waveguide. This method has successfully been used to calculate the mirror reflectivities for mid-infrared QCLs and semi-insulating (SI) surface-plasmon THz QCLs [4, 69]. For a *GaAs/air* interface in which the effective index of *GaAs* is 3.6 and that of air is 1.0, the reflectance is roughly 0.32 ($R = (r_{Fresnel})^2 \approx 0.32$).

2.1.3.2 Impedance mismatch method

When the dimension of the laser waveguide shrinks to the order of the operating wavelength, the infinite plane-wave approximation is not valid anymore. One such example is the THz QCL with a metal-metal waveguide, where the device lasing aperture sizes are much less than the free-space wavelength of the radiation beam, $d \ll \lambda$. This is similar to the case of micro-strip transmission lines. The impedance mismatch method from the transmission line theory can be adopted for the mirror loss calculation in metal-metal THz QCLs [70]. The basic idea of this theory is that a particular input mode is represented by an equivalent transmission line model. In this approach, each of the waveguide modes in a THz QCL [71] has an equivalent transmission line model, with an equivalent voltage and current. In transmission line model, if the load impedance is the same as the line impedance there is no reflection. On the other hand, if the load impedance differs from line impedance we have the reflection loss which can be calculated by equation (2.3):

$$r = \frac{Z_L - Z_1}{Z_L + Z_1} \quad (2.3)$$

where Z_L is the load impedance as seen from the fundamental mode propagated in waveguide. In practice, it is very difficult to calculate the antenna impedance because it requires accurate knowledge of the near field reactive fields.

2.1.4 Confinement factor

Confinement factor is another important parameter in designing the THz QCL waveguide. This factor is the fraction of power inside the active region to the total power guided in the waveguide, defined as:

$$\Gamma = \frac{\frac{1}{2} \iint_{Inside} Re(E \times H^*) dx dy}{\frac{1}{2} \iint_{Total} Re(E \times H^*) dx dy} \quad (2.4)$$

2.1.5 Threshold Gain

The threshold condition for a particular mode in a waveguide to lase is that the wave reproduces itself after one round-trip. Let a particular mode traveling in the z direction be represented by a spatial field profile $h(x, y)$ and assume the mode has a propagation constant k_z as

$$k_z = \alpha + i\beta \quad (2.5)$$

The full field of the mode is $H(x, y, z) = h(x, y) \exp(ik_z z)$. The waveguide loss of this mode is defined as

$$\alpha_\omega = 2\beta \quad (2.6)$$

which includes all absorptive losses contributed by the waveguide. The threshold gain is the minimum gain which is necessary to sustain lasing operation in a laser and can be obtained by

$$G_{th} = \frac{\alpha_\omega + \alpha_m}{\Gamma}, \quad (2.7)$$

where Γ is the confinement factor (equation (2.4)) and α_m the mirror loss (equation (1.1)). After clarifying the basic concepts, we will investigate and compare two important THz waveguides in more detail, namely metal-metal and semi-insulating surface Plasmon waveguides, in the following sections.

2.1.6 Semi-Insulating Surface Plasmon versus Metal-Metal THz waveguides

2.1.6.1 Semi-Insulating-Surface-Plasmon waveguide

The Semi-Insulating-Surface-Plasmon (SISP) waveguide, first described by Ulrich *et al.*, was a key enabling component of the first terahertz QCLs [4]. In this structure, the optical mode is bound to the upper metallic contact and a thin ($0.1 - 1 \mu m$) heavily doped contact layer grown directly beneath the active region but above the semi-insulating (SI) GaAs substrate. Figure 2.1 shows a schematic diagram of the cross-section of a SISP waveguide. A few important dimensional parameters are also labeled in the figure. Because the doped semiconductor layer (the plasma layer) is thinner than its own skin depth at the lasing frequency, the optical mode extends substantially into the SI substrate. As a result, the spatial overlap of the optical mode with the doped semiconductor layer is small, the free carrier loss in the plasma layer is minimized.

Good-performance SISP waveguides rely on proper choices of dimension and physical parameters. For example, the doping concentration of the highly-doped material (the

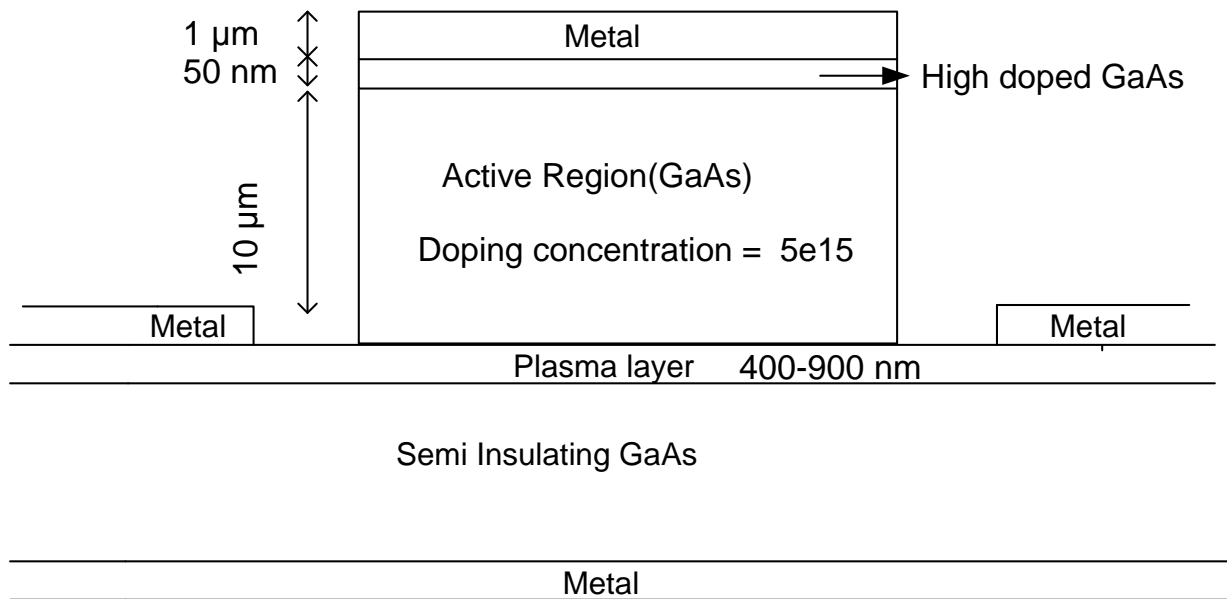


Figure 2.1: Schematic of the cross-section of an SISIP waveguides geometry.

plasma layer) and its thickness play an important role in the waveguide loss and the confinement factor of the confined optical mode. A thicker plasma layer results in a higher confinement factor but higher waveguide loss.

2.1.6.2 Metal-Metal Waveguide

The schematic geometry of a metal-metal (MM) waveguide is shown in Fig. 2.2. The waveguide, different from the SI surface-plasmon waveguide, is based on a double-sided surface-plasmon between the top and bottom metallic contacts. This metal-metal waveguide is essentially a microstrip waveguide, which is used in microwave and millimeter-wave frequency range. Since the skin depth in gold at THz frequencies is only several hundred Angstroms [72, 73, 74], the confinement factor of this waveguide is close to unity.

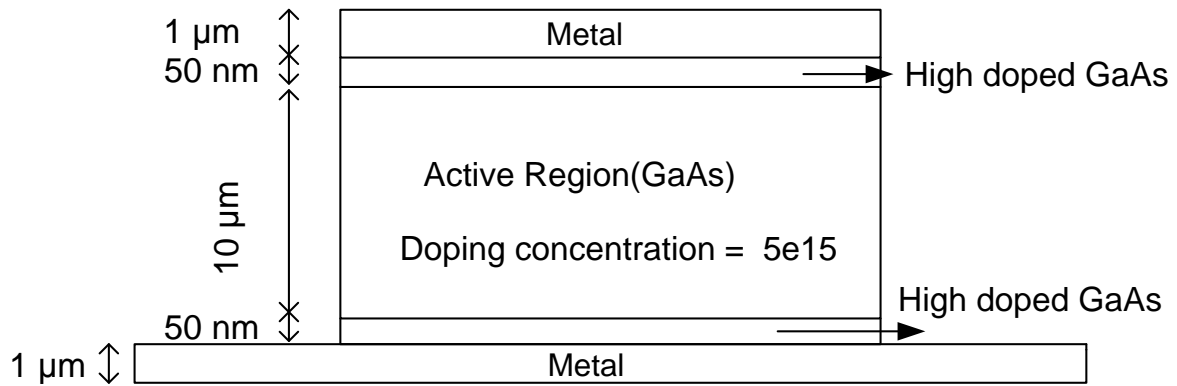


Figure 2.2: Schematic of the cross-section of an MM waveguides geometry.

The heavily doped GaAs layers adjacent to the top and bottom metallic layers are needed for forming ohmic contacts. Unfortunately, these doped semiconductor layers can be a significant source of the optical loss, and their thickness should be minimized. The loss and confinement factor of this waveguide change when the thickness and doping of active region change. For thinner waveguides, the optical loss increases because the long-wavelength radiation penetrates more into the lossy doped semiconductor layer and metallic regions. If the increase of the loss can be tolerated, the active region can be made thinner, which shortens the excessively long MBE growth time. It typically takes more than 12 hours to grow a 10 μm thick epitaxial active region. A thinner active region consists of fewer cascade modules, lowers the threshold voltage and thus dissipates less power. While

the metal-metal waveguide possesses potentially excellent optical properties, great care should be taken during the device fabrication process to ensure adequate thermal and mechanical properties of the device.

2.1.6.3 Waveguide comparison

Even though α_ω of a MM waveguide is higher, the close-to-unity Γ yields a lower α_ω/Γ than that of a SISP waveguide. As such, THz QCLs with a MM waveguide typically exhibit superior performance at all frequencies. Additionally, using a metal-metal waveguide, thinner and narrower waveguides are more feasible, which leads to reduced power dissipation and easier heat removal. Furthermore, the use of lateral heat removal techniques on the laser ridge such as epitaxial regrowth, ion implantation isolation [75], or thick gold electroplating [76], or epi-layer down mounting are more easily facilitated using the metal-metal waveguide. The principal disadvantage for the metal-metal waveguide is the extra processing complexity because of the needed metal-metal wafer-bonding. This may potentially lead to a reduced yield, a higher thermal contact resistance and degraded device performance. However, this issue could be alleviated as the semiconductor device fabrication technique is continuously improved. The thermal conductivity of metals becomes superior than that of semiconductors at higher temperatures. For example, the thermal conductivity of Au is higher than that of GaAs at $T > 100K$. As a result, the metal-metal waveguide can dissipate heat from the active region faster than the SISP waveguide does. The metal-metal waveguide devices typically exhibit better temperature performance. Most of high performance THz QCLs were achieved by using a metal-metal waveguide [50, 54, 56]. Even though both waveguides have been employed for terahertz generation over a wide frequency range (3-6 THz), the metal-metal waveguide becomes increasingly advantageous at lower frequencies, especially at frequencies below 2.5 THz, because of its close-to-unity confinement factor. Nevertheless, the SISP waveguide device can produce higher output power and less-diffractive far-field patterns. In some special cases, the SISP waveguide may show unique properties over the metal-metal waveguide, for example, selectively exciting different optical modes by tuning device bias [77]. Since all the devices presented in this report are based on metal-metal waveguide, we will discuss two effects of MM waveguides designs on the performance of THz QCLs in the following section.

2.1.7 M-M waveguide

Figure.2.3 shows different sections of the MM waveguide. The thickness and the doping of the active region and the high doped material will affect on the loss of the device. Since the skin depths of the top and the bottom contact layers are lower than their thickness, a portion of the field will penetrate in metal. As a result, the type of the metal used in fabrication process is also important. In addition the total height and the width of the device will affect the cavity loss. By decreasing the active region thickness, the waveguide loss increases. This increase in loss is due to an increase in modal coupling with the surface plasmon associated with the metal contacts. There are some growth limits that we cannot have the thickness higher than $10\ \mu\text{m}$. Even though a wider device has a lower waveguide loss, the chance of exciting higher modes is also higher which is undesirable. To reach a lower waveguide loss and not excite the higher modes a common technique presented in [78] will be employed. In this technique, schematically illustrated in Fig.2.3, the top metal contact will not totally cover the top of ridge width. The effect of top metal gap on the loss of the MM waveguide will be investigated in the next section. In addition, the effect of different metal processes on the waveguide loss and performance of device is experimentally and theoretically studied.

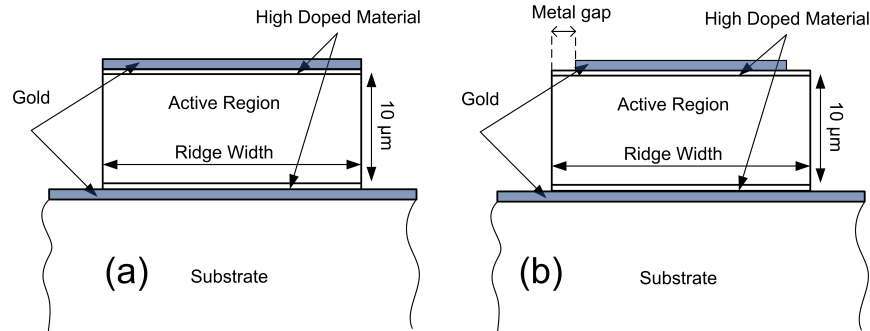


Figure 2.3: Schematic presentation of the simulated MM THz QCL structure. The laser ridge width and the metal gap distance vary for simulating different waveguide mode allocations. a) no metal gap, b) variable metal gap

2.1.7.1 Top metal gap effect

The M-M waveguide demonstrates the lowest threshold gain for THz QCL structures. However, the low threshold gain also leads to excitation of higher order transverse modes

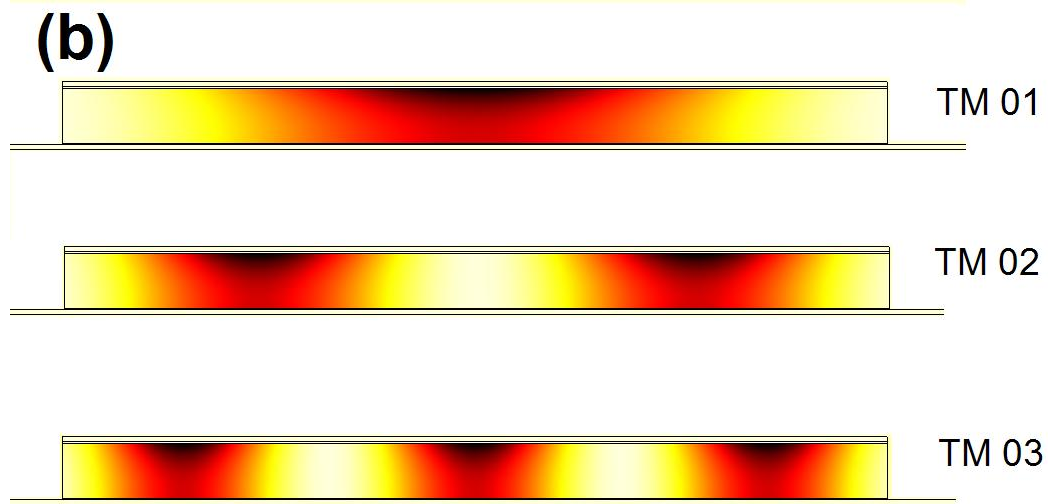
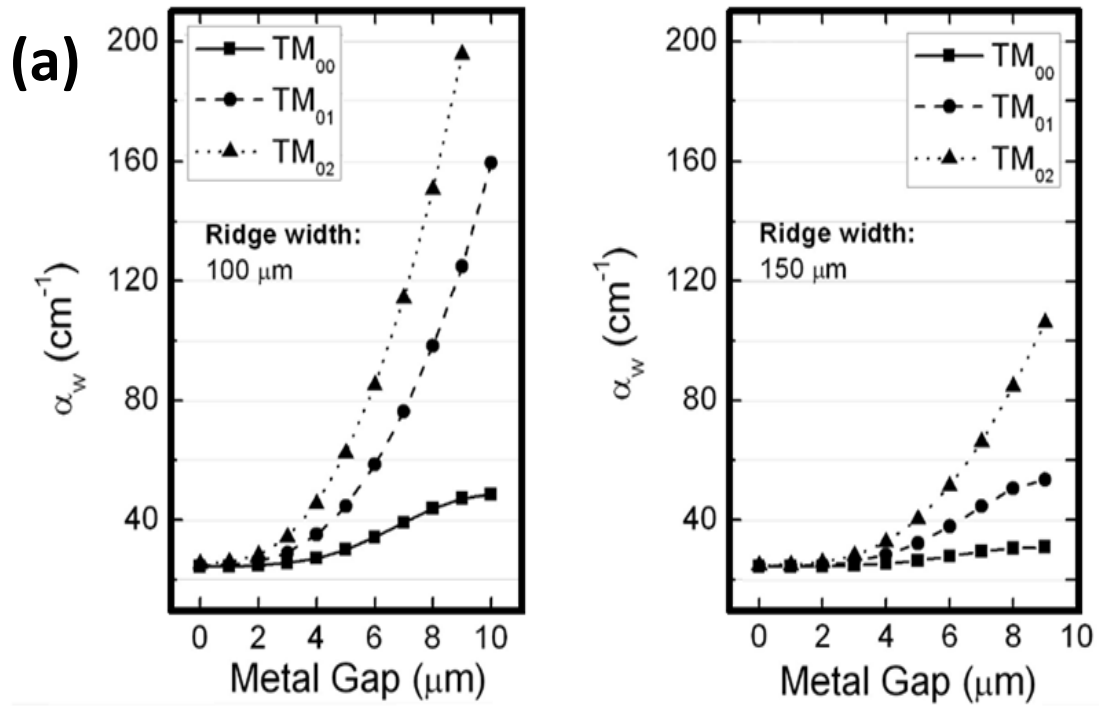


Figure 2.4: a) The total loss of M-M waveguide for 100 and 150 μm width in different metal gap. b) The power intensity of M-M waveguide for the first three TM modes

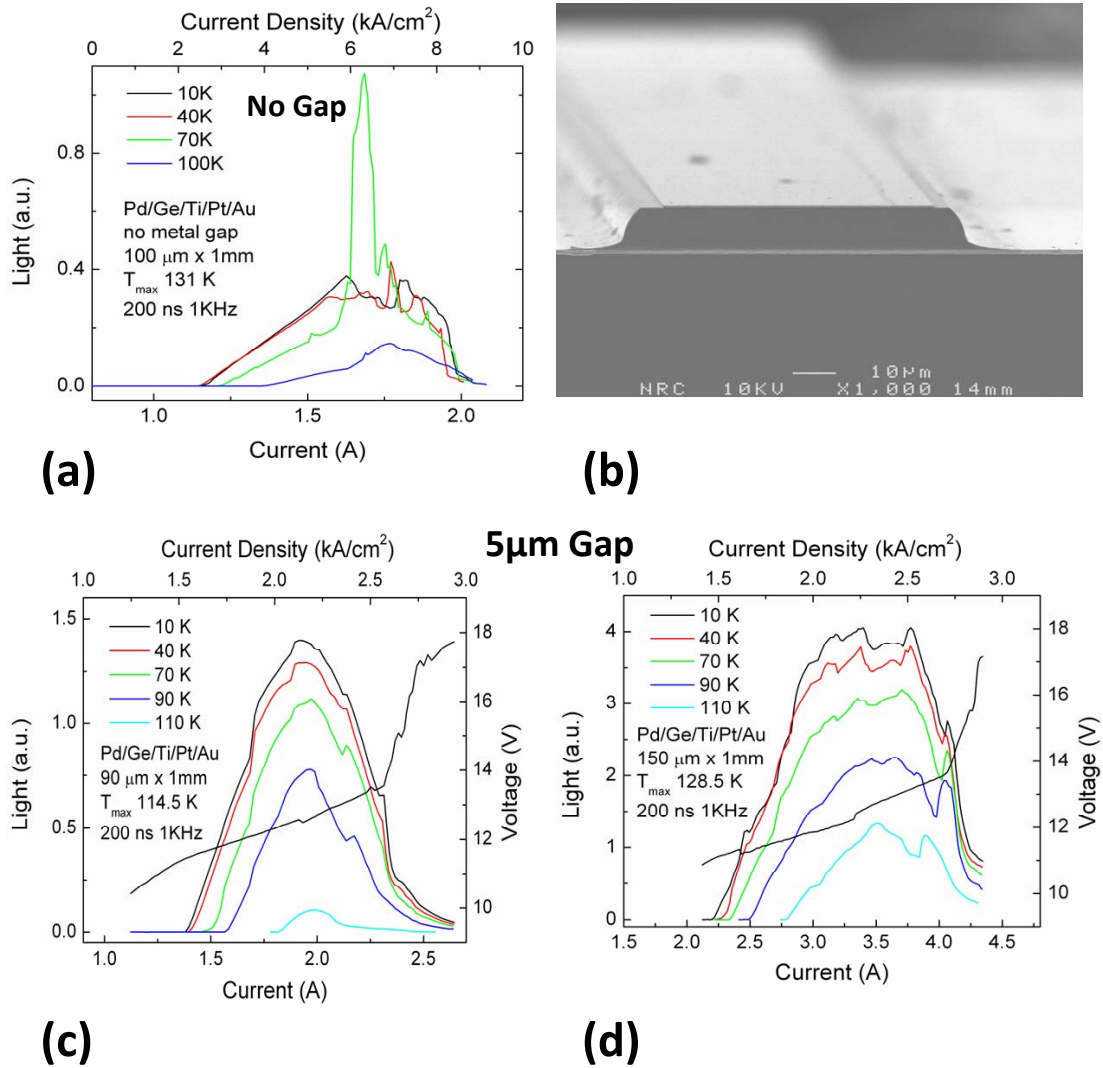


Figure 2.5: The collected THz light (optical output power) versus current curves for MM THz QCLs with a) no metal gap, c) 5 μm metal gap and 90 μm ridge width and d) 5 μm metal gap and 150 μm ridge width and 1 mm length at different heat sink temperatures. The device is fabricated using Pd/Ge/Ti/P t/Au metal contacts and is biased in pulsed mode (pulse width = 200 ns, repetition rate = 1 kHz). The SEM of this waveguide is also shown in b).

(TM). When multiple transverse modes are lasing simultaneously, the optical (such as light vs. current) and electrical (such as current vs. voltage) characteristics of the device often become undesirable; its far field emission pattern is far from ideal. In this section, we systematically study the effect of top metal gap and propose an efficient structure for low loss and single mode operation of M-M THz QCLs. The modal waveguide loss of 100 and 150 μm wide laser ridges, with various sizes of side absorber was calculated in 2D simulation.

The waveguide simulations model the 10 μm active region as pure GaAs, doped to an average bulk doping density of $6 \times 10^{15} \text{ cm}^{-3}$. The entire active region structure is sandwiched between a 100 nm top and 100 nm bottom n^+ GaAs contact layers doped to $5 \times 10^{18} \text{ cm}^{-3}$ and $3 \times 10^{18} \text{ cm}^{-3}$, respectively. The simulations consider a metal layer and an n^+ GaAs substrate below the active region. Figure 2.3 shows the 2D schematic of two typical MM waveguides, one with metal gap (b) and one without metal gap (a).

The modal loss calculation was performed for each waveguide width with indented top metal coverage (shrinking from the both edges of the ridge laterally, up to 10 μm as shown in Fig.2.3(b)). The different increase rates in waveguide loss stem from different spatial overlaps between the side absorbers and the quasi-transverse magnetic (TM) modes; the fundamental mode has the minimum and the third-order mode has the greatest overlap with the side absorbers (Figure 2.4-b). Each quasi-TM mode starts to lase when the optical gain of the active region reaches its total loss. The waveguide loss for various transverse modes are calculated and depicted in Fig. 2.4. By increasing the metal gap from zero up to 2 μm , the waveguide loss for first three modes does not change significantly and remains very close to each other. By further increasing the gap, the loss of all modes including the fundamental mode (TM_{00}) increases. However the introduction of the metal gap increases the loss of the higher order modes much more than the lower order modes. For instance, an 8 μm gap on a 150 μm ridge increases the loss of fundamental mode by only $\sim 6 \text{ cm}^{-1}$, while it increases the loss of TM_{01} and TM_{02} modes by around 36 and 82 cm^{-1} , respectively. The increase of modal loss is more pronounced in the narrower ridge (Figure 2.4-a). In the following, the result of fabricated MM QCL will be discussed, which clearly show the introduction of top metal gap successfully suppress the excitation of higher-order mode, even in narrower waveguide device.

Figure 2.5-a shows the LI characteristic of 100 width MM QCL. By increasing the current, the gain of the active region increases and consequently higher order modes also gets excited. As shown in figure 2.5-a the second peak can be observed after 1.6 A that confirms the excitation of higher modes. Even though the metal gap of 5 μm was selected for both 90 and 150 μm width MM QCL, the LI curve of figures 2.5-c and 2.5-d shows the excitation of higher modes in larger width(150 μm) due to lower waveguide loss. The LI

of a device which only excites the fundamental mode is smooth and has a bell shape (c) while there is a kink in the LI of a device which excites higher-order modes (a and d). A waveguide with 100 μm width and top metal gap will only excite the fundamental mode. This value can be also obtained from figure 2.4-a. The SEM of the fabricated QCL is also shown in Fig. 2.5.

2.1.7.2 Effect of metal on temperature performance of THz QCL

As the lasing frequency approaches to the THz range, the high tangent loss of the metals makes a significant contribution to the overall waveguide loss despite small penetration depth of the electromagnetic mode into the metal layers. As a result, the stack of contact metals needs to be carefully selected based on not only their electrical properties, but also their optical properties [79]. In this section, the waveguide loss of a THz QCLs with four different Au- and Cu-based metal contacts are calculated to investigate the effect of different metal contacts on temperature performance of the structure. The simulation and the experimental result are presented and compared.

The THz QCLs used in this study are based on a GaAs/Al_{0.15}Ga_{0.85}As three-well cascade module with layer thicknesses of **45**/87/**29**/83/**44**/159 Å—the barriers are indicated in bold fonts. The quantum well of 159 Å is doped with Si dopant atoms to a two-dimensional carrier concentration of $3 \times 10^{10} \text{ cm}^{-2}$ per module ($N_{3D} = 6.7 \times 10^{15} \text{ cm}^{-3}$). The whole QCL structure consists of 224 repeats (10 μm thick) of this module and was grown on a semi-insulating (SI) GaAs substrate by using MBE. To facilitate the electrical contacts, the active region is sandwiched between 100 nm of $3 \times 10^{18} \text{ cm}^{-3}$ bottom n^+ GaAs and top stack of 50 nm of $5 \times 10^{18} \text{ cm}^{-3}$, 10 nm of $5 \times 10^{19} \text{ cm}^{-3}$ n^+ and 3.5 nm of low-temperature (LT) grown GaAs. The last two layers are used to form a non-alloyed ohmic contact [79].

Four groups (A—D) of QCL devices with different metal stacks for the electrical contacts were fabricated and tested to examine their effects on device performance. The metal stack employed in group A is Pd/Ge/Ti/Pt/Au (55/100/25/55/300 nm), which was annealed at 380°C for 15 seconds and formed an ohmic contact with the n-type GaAs contact layer. The metal stack employed in group B is Ti/Pt/Au (25/55/300 nm), annealed at 350°C for 15 seconds. The annealing of the first two groups yielded alloyed contacts. The metal stack employed in group C is the simplest, consisting only two layers Ti/Au (5/300 nm, non-annealed). The metal stack employed in group D is Ta/Cu/Au (10/500/100 nm, non-annealed).

The temperature-dependent waveguide losses for the structure with the metal claddings

made of the four aforementioned metal stacks were calculated from simulating the complete 2D structure of the device shown schematically in Fig. 2.6, at a lasing frequency of 3.75 THz. The device model consists of 10 μm thick and 144 μm wide MM THz QCL waveguides. The temperature dependent permittivity and mobility of the active and n^+ regions were calculated using the data in [80, 81], respectively. The optical constants for the metals (plasma and carrier collision frequencies) were taken from [82] and the complex permittivity of various layers was calculated using the Drude-Lorentz approximation as defined in (2.1). The temperature dependence of metal permittivity is extracted from the conductivity temperature dependence data in [82]. The full details of the waveguide structure, including the thin highly doped GaAs layers below and above the 10 μm thick active region and the thin metal layers of platinum, gold and copper in the metal stacks, were taken into account in the simulation. Due to lack of information about the metals of titanium, palladium germanium and tantalum, these layers are modeled by using the temperature-independent parameters of tungsten. The calculated waveguide losses in Fig. 2.6 are in good agreement with the experimental results reported by other groups [83]. (The measured gain for a device with Ta/Cu metal process was 18 cm^{-1} which is comparable with our simulation).

As shown in Fig. 2.6, the metal cladding of Pd/Ge/Ti/Pt/Au exhibits the highest waveguide loss (α_ω) over the temperature range of the simulation. The metal cladding of Ti/Pt/Au shows the second-highest waveguide loss, with a small reduction of $\sim 35\text{ cm}^{-1}$ in α_ω compared to that of Pd/Ge/Ti/Pt/Au over the temperature range from 90 to 250 K. The metal cladding of Ti/Au shows a further reduction of $> 10\text{ cm}^{-1}$ in waveguide loss. The metal cladding of Ta/Cu/Au has the lowest waveguide loss, $\sim 18\text{ cm}^{-1}$ even at 160 K. The effects of the mirror losses of the different metal contacts are not taken into account in the following discussion. This is because that the mirror loss is much smaller compared to the waveguide loss in MM THz QCLs [50], and the variation of the mirror loss due to different metal contacts is therefore negligible. Since the T_{max} of the THz QCLs are strongly affected by the waveguide losses, it is expected that the performance of the devices with different metal claddings could be significantly different.

Maximum lasing temperature is one of the important performance indicators of THz QCL devices. T_{max} is determined when the temperature-degrading optical gain reaches the optical cavity loss (figure 2.6). Devices with lower loss are hence expected to show higher lasing temperatures. The simulation of the optical gain, on the other hand, was performed using the simplified density matrix model presented in [55]. The gain model includes intersubband LO-phonon, ionized impurity and interface roughness scattering mechanisms. Some key simulation parameters deployed in our simulations are electron heating temperature (90 K), pure dephasing time constant (0.36 ps) and lasing dephasing time constant

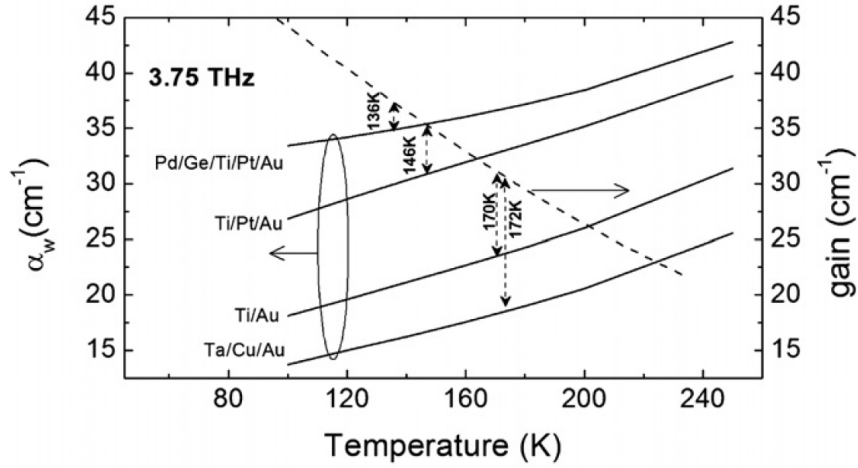


Figure 2.6: Calculated waveguide losses of THz QCLs with different metal claddings. The curves from the top to the bottom correspond to metal claddings made of Pd/Ge/Ti/Pt/Au, Ti/Pt/Au, Ti/Au and Ta/Cu/Au. The waveguide losses increase with temperature for all cases. The device with a metal cladding made of Ta/Cu/Au has the lowest waveguide loss. The right vertical axis shows the simulated optical gain based on a simplified density matrix model [55], which includes intersubband LO-phonon, ionized impurity and interface roughness scatterings. At T_{\max} (136, 146, 170, 172 K) the disagreement between the simulated waveguide loss and optical gain is represented by the vertical double arrows. This disagreement could be explained by the inaccuracy of the models used for optical gain and waveguide loss, as well as waveguide imperfections.

(1.15 ps). Other simulation parameters can be found in [55]. The experimental results show T_{\max} of 136 K for device A, 146 K for device B, 170 K for device C and 172 K for device D. The improvement in temperature performance from devices A to D could mainly be attributed to the reduction of waveguide losses, due to the different metal contacts [68]. Device D reached the highest T_{\max} because it has the lowest waveguide loss.

2.2 Quantum Design of THz QCLs

The numerical simulation of a multiple quantum well structure is the main subject of this section. Figure 2.7 shows the block diagram of our quantum calculation procedure. In our calculation model, we first define the material system, Electric field, Temperature, and doping concentration value and position. Transfer Matrix Method (TMM) is employed to calculate the energy states and the wavefunctions of our quantum design. These calculated values can be used as inputs of the next steps of our calculations which are detuning and coupling calculation, oscillator strength calculation, and scattering time calculation. Finally, we used a rate equation model to estimate the current density and gain spectrum which will be discussed in detail in chapter 3. Since all the structures, presented in this work, are based on GaAs/AlGaAs material system, we first explain all assumptions and methods of the energy state and the wavefunction calculation which are used in our simulations. External electric field and the energy band nonparabolicity are then taken into account in our numerical modeling. Finally, key intersubband and intrasubband scattering mechanisms will be discussed and the numerical calculation of each of them will be presented.

2.2.1 Energy state and wavefunction calculation

The active region of a Terahertz quantum cascade laser consists of a multi-quantum well heterostructure. The quantum wells are formed due to the conduction band offset between alternating thin layers of two semiconductor materials. The electronic wavefunctions that are used in the analyses can be computed within a slowly-varying envelope approximation in the MQW growth direction. Hence the effective mass m^* is the only parameter that describes the energy dispersion of the conduction band, albeit with different values for the quantum-wells and the barriers, respectively. Contrary to most of Resonant-Phonon (RP) THz QCL which are based on GaAs/Al_{0.15}Ga_{0.85}As material system and the non-parabolicity of the band could be ignored, in Indirectly-Pumped THz QCLs, this effect has

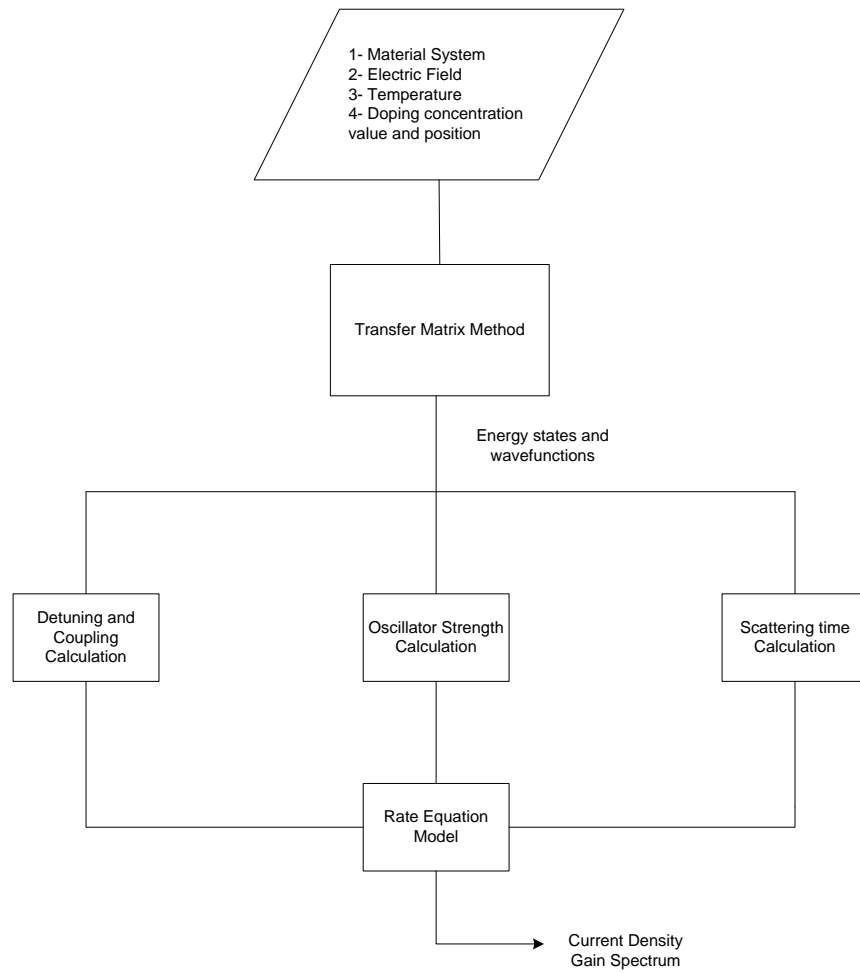


Figure 2.7: The block diagram of the numerical calculation of THz QCLs.

to be included. It means the effective mass assumed to be position and energy dependent even inside the well or barrier. Based on aforementioned assumption, the Transfer Matrix Model (TMM) was employed to calculate the energy states and the wavefunctions of all structures presented in this thesis.[84] Among different methods of calculation, TMM was chosen because it can be easily implemented while the numerical computing time is short. In addition, the band nonparabolicity effect can be easily included in the model without any recursive loop calculation. Since the doping concentration of all THz QCLs presented in this thesis is relatively low, the band-bending, which arises due to spatial separation of the positively charge dopant impurities and the negatively charged electrons is neglected. In all calculation the Poisson equation was not included to be self-consistently solved with Schrödinger equation. The potential barrier height of the conduction band $\Delta E_C = 0.65(1.36 + 0.22x)x$ where x is the fraction of Aluminum in $GaAs/Al_xGa_{1-x}As$ material system. The initial effective masses of the barrier and well are $m_B = (0.067 + 0.083x)m_0$ and $0.67m_0$, where m_0 is the mass of the electron.

2.2.2 Band structure of a Terahertz quantum cascade laser

In this thesis, we only calculate one module of the THz QCL and we assume all modules have the same relative energy states and wavefunctions. This assumption is true as long as the dropped voltages of all modules are the same. The non-linear voltage drop effect, which could substantially affect the performance of a THz QCL, is ignored in our modeling. As an example, the calculated conduction band diagram and the moduli squared wavefunctions of a THz QCL at zero and designed electric field is shown in Fig. 2.8. The range of the operating electric field of a THz QCL starts from 0 kV/cm to an electric field at which the ground state of the left module is aligned with the desired state in right module. This highest electric field is sometimes called *alignment electric field* as it is typically the field where the current density of the lasing device is expected to be maximum. In most high performance THz QCL devices, the injector state is the most populated states and is in resonance with the upper lasing states of the next module at *alignment electric field*.

To include the nonparabolicity effect in our energy state and wave function calculation, the effective mass of the electron was assumed to be energy dependent. Based on the model presented in [85], for each energy state, the mass of the electron was updated in our numerical calculation. The new energy state, calculated by energy-dependent mass, was included in our model to calculate the corresponding wavefunction. TMM would helped us too include the nonparabolicity effect in our numerical model with minimum computational overhead.

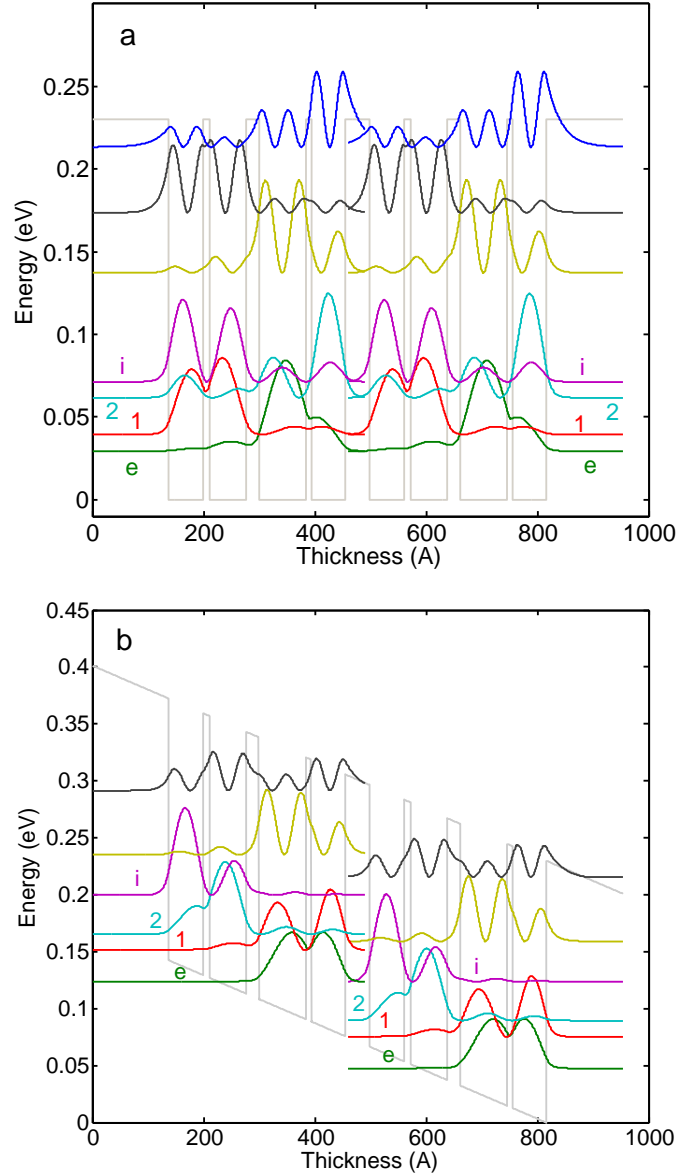


Figure 2.8: Conduction band diagram and the moduli squared of wavefunctions of the THz IDP-QCL, V843 [60], at a) 0 kV/cm and b) alignment electric field (21 kV/cm). The first for states of each module labeled by *e*, 1, 2, and *i*.

2.2.3 Main parameters of the transport model

Even though the detail of the transport model will be discussed in chapter 4, the major concept of the modeling and a few key parameters are explained in this section. The scattering time between different states of the quantum designs consists of two different mechanisms in our modeling: the scattering time between two states of different modules (Intermodule scattering) and the scattering time between two states in one module (Intramodule scattering). The former can be calculated by Tight Binding formalism, while the latter will be calculated based on different scattering mechanisms such as longitudinal optical (LO) phonon scattering, acoustic phonon scattering, alloy scattering, interface roughness scattering, ion impurity scattering. In this section of the thesis, first we explain the method of the calculation of the detuning and coupling between two states in two neighbor modules. It can help us to estimate the tunneling time and different current paths. Different scattering mechanisms and their calculation methods will be presented to see the effect of each mechanism in quantum design and modeling.

2.2.4 Tight binding parameters, detuning and coupling

To estimate the tunneling time between two states separated by a barrier, we have to calculate the detuning and the coupling between those states using a tight binding model [86]. To simplify our calculation, the height of the barrier and the width of the well were chosen to have only one confined state in each well. In reality, All confined states in one module are calculated, then the coupling and the detuning between all left states and right states will be determined. The coupling between those state depends on the shape of the wavefunction, the height and the width of the injector barrier. By having the energy state, E , and the corresponding wavefunction, ψ , of the left and right quantum well, the wavefunctions of the double well can be represented by linear superposition of the two wavefuctions.

$$\psi = \alpha\psi_L + \beta\psi_R, \quad (2.8)$$

Coefficients α and β can be determined by

$$\begin{pmatrix} E_l + s_{ll} - E & (E_r - E)r + t_{lr} \\ (E_l - E)r + t_{rl} & E_r + s_{rr} - E \end{pmatrix} \times \begin{pmatrix} \alpha \\ \beta \end{pmatrix} = \begin{pmatrix} 0 \\ 0 \end{pmatrix}, \quad (2.9)$$

where E_l and E_r are the energy states of the left and right modules. In addition,

r , s and t are overlap, shift and transfer integral, respectively. [86]

$$\begin{cases} s_{ll} = \int \psi_l V_r \psi_l dz, & s_{rr} = \int \psi_r V_l \psi_r dz \\ t_{lr} = \int \psi_l V_l \psi_r dz, & t_{rl} = \int \psi_r V_r \psi_l dz \\ r = \int \psi_l \psi_r dz \end{cases} . \quad (2.10)$$

By having the overlap, shift and transfer integral, the detuning ($\hbar\Delta$) and the coupling ($\hbar\Omega$) between two states can be obtained by

$$\begin{cases} \hbar\Delta = (E_l + s_{ll}) - (E_r + s_{rr}) \\ \hbar\Omega = \frac{1}{2} \sqrt{(E_1 - E_2)^2 - \Delta^2} \end{cases} . \quad (2.11)$$

where E_1 and E_2 are the energy states of the double well which can be determined by solving the determinant of the left matrix in equation (2.9) equals zero.

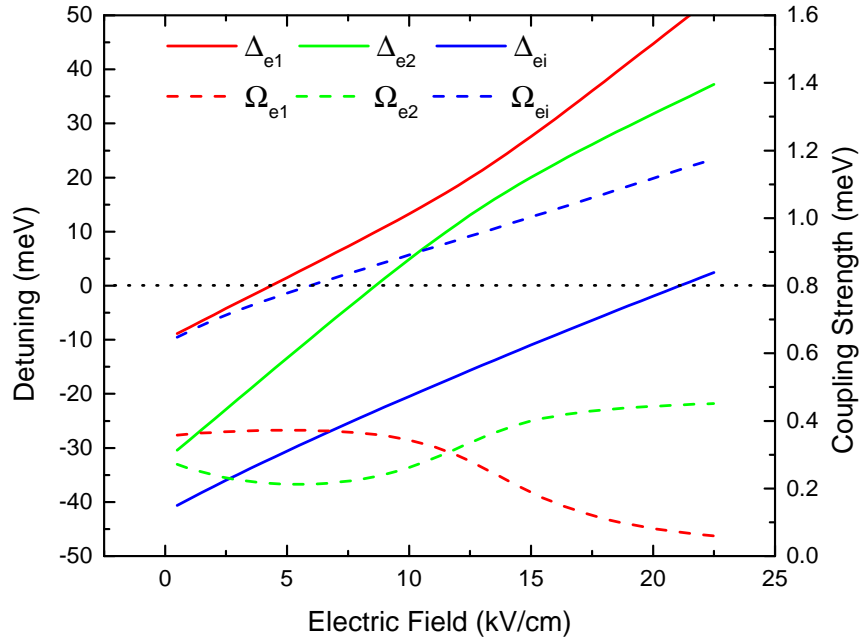


Figure 2.9: The detuning and the coupling strength between different states of the structure presented in [60]. The detuning between two states at their alignment electric field is zero. The coupling strength will affect the tunneling time when the detuning is minimum. Δ and Ω are detuning and coupling between different states, respectively.

To see how detuning and coupling change with electric field, they are calculated for the first IDP structure based on phonon-photon-phonon scheme [60] and illustrated in

Fig. 2.9. Since the current density of the structure is mostly determined by the carrier injected from the ground state of the left module to all other states of the right module, the detuning and the coupling corresponding to those states plotted at different electric field. The detuning and the coupling between states a and b are shown by $\hbar\Delta_{ab}$ and $\hbar\Omega_{ab}$, respectively. The detuning between level e and other states in right module starts with a negative value and it passes the zero line at an electric field which those states are aligned. The coupling between level e and other states in right module depends on the overlap between the wavefunction of those states that can change by electric field.

To investigate the performance of an IDP THz QCL in terms of IV characteristic, the coupling strength between level e and levels 1 , 2 , and i at an electric field which the corresponding detuning is zero has to be calculated. The coupling strength between level e and 1 at alignment electric field of 4.4 kV/cm equals to 0.385 meV ($\hbar\Omega_{e1} = 0.385$ meV). States e will be aligned at electric field of 8.8 kV/cm and 21kV/cm with states 2 and i while the corresponding couplings are 0.24 meV and 1.14 meV ($\hbar\Omega_{e2} = 0.24$ meV, $\hbar\Omega_{ei} = 1.14$ meV), respectively. A good design is a structure which minimizes the coupling between level e and all other states of right module except level i . When state e is aligned with one state in right module (1 , 2 , or i), the detuning is minimized and the current injection correspond to those states is maximized. The effects of the detuning and coupling strength will be discussed in detail in chapter 3 of this thesis.

2.2.5 Scattering time calculation

In this section the intersubband and intrasubband scattering mechanisms in a THz QCL will be introduced. Unuma *et. al.*[87], and Ando[88] have studied various scattering mechanisms in GaAs/AlGaAs quantum structures. Some of which —those play a critical role in THz QCL carrier transport— are described here and implemented in our simulation tool. The band nonparabolicity is not included in all scattering times calculation for simplicity.

2.2.5.1 Intersubband and Intrasubband scattering time

In this section, we present the model described by Unuma in calculation of Γ_{inter} (broadening due to intersubband transition) and Γ_{intra} (broadening due to intrasubband transition) in a superlattice structure. The intersubband transition governs the rate of carrier accumulation or depletion at quantum states while the intrasubband transition controls carrier distribution at one state and determines the energy broadening. Figure 2.10 shows a few typical intersubband transitions (a) and intrasubband transitions (b).

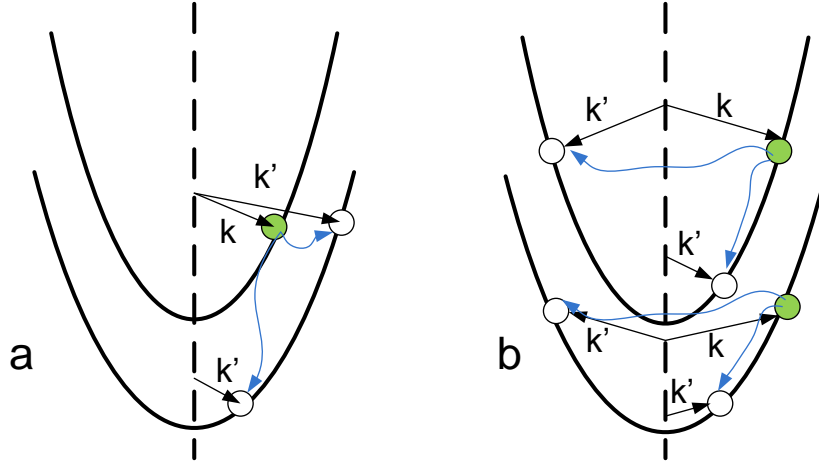


Figure 2.10: a) Intersubband b) Intrasubband scattering from the initial wave-vector k to a final wave-vector k' . Both Intersubband and Intrasubband scattering can be elastic or inelastic.

2.2.5.2 Intersubband scattering time

The energy broadening due to intersubband scattering from state $|a\mathbf{k}\rangle$ to all possible states $|b\mathbf{k}'\rangle$ for a perturbation interaction H is given by

$$\Gamma_{\text{inter}}(E) = 2\pi \sum_{k'} \langle |(a\mathbf{k}|H|b\mathbf{k}')|^2 \rangle \times \delta[\varepsilon_a(\mathbf{k}) - \varepsilon_b(\mathbf{k}') + E_{ab}] \quad (2.12)$$

where the intersubband energy separation E_{ab} is ($E_{ab} = E_a - E_b$) and the subband energy-dispersion of each subband is defined by:

$$\varepsilon_a(\mathbf{k}) = \frac{\hbar^2 \mathbf{k}^2}{2m_a} \quad (2.13)$$

H is the scattering potential Hamiltonian, and $\langle \dots \rangle$ denotes the average over distribution of scatterers. This theory assumes a parabolic energy dispersion, or a constant effective mass for different subbands. Equation (2.12) can be used for all elastic transitions. If we want to calculate an inelastic intrasubband transition (for example Longitudinal-Optical (LO) Phonon scattering), we have to modify the delta function to $\delta[\varepsilon_a(\mathbf{k}) - \varepsilon_b(\mathbf{k}') + E_{ab} \pm \hbar\omega_{LO}]$ where $\hbar\omega_{LO}$ is the phonon energy (36.7 meV in GaAs). The positive and the negative signs correspond to absorption and emission of LO phonons, respectively.

2.2.5.3 Intraband scattering time

By assuming the parabolic conduction band, the energy broadening due to intraband scattering in two subbands a and b is given by

$$\Gamma_{\text{intra}}^{\text{ab}}(E) = 2\pi \sum_{k'} \langle |\langle a\mathbf{k}|H|a\mathbf{k}'\rangle - \langle b\mathbf{k}|H|b\mathbf{k}'\rangle|^2 \rangle \delta[\varepsilon(\mathbf{k}) - \varepsilon(\mathbf{k}')] \quad (2.14)$$

In equation (2.14) the mass of subband a is assumed to be the same as the mass of subband b for simplicity. In addition, it is for elastic process. we have to update the delta function as well as we did for inelastic intersubband transition. the updated functions will be $\delta[\varepsilon(\mathbf{k}) - \varepsilon(\mathbf{k}') \pm \hbar\omega_{LO}]$, where the positive sign and the negative sign denote the absorption and the emission process, respectively.

Since the spontaneous emission lifetime in the THz range is typically in microsecond range, the sub-threshold carrier transport in a typical RP based THz QCL (both sub-threshold and supra-threshold carrier transport in a typical IDP based THz QCL), is dominated by non-radiative fast scattering mechanisms with lifetime in picoseconds range. Among all scattering mechanisms, discussed in [87], the most important scattering time which can affect the carrier transport in THz QCL structure based on GaAs/AlGaAs will be explained in this section. LO-phonon scattering is the most important mechanism which strongly affects the carrier depopulation in RP QCLs and the carrier injection and depopulation in IDP QCLs. The interface roughness (IR) scattering which can be ignored in typical RP QCLs due to low Aluminum fraction, starts to play a more substantial role in IDP QCLs (the typical Aluminum fraction in RP QCL is 15% while it is 25% in our IDP QCLs). Another important scattering mechanism is the ionized impurity scattering, arising from ionized Si dopant in quantum cascade structures. These three scattering mechanisms will be explained and their corresponding equations will be presented in the following sections.

2.2.5.4 Longitudinal optical phonon scattering time

The most effective scattering mechanism in carrier transport of quantum cascade lasers is the LO phonon scattering. The carriers can be depopulated fast from the lower lasing state in a RP QCL through LO phonon scattering, which is advantageous in sustaining population inversion. On the other hand, at higher temperatures (e. g. 150 K or above) the carriers of the upper lasing state can be depopulated through the same mechanism, which

could significantly reduce the population inversion. This becomes a bottleneck of high-performance operation of THz QCLs. The accurate and fast calculation of this scattering time is crucial for the modeling of the THz QCLs.

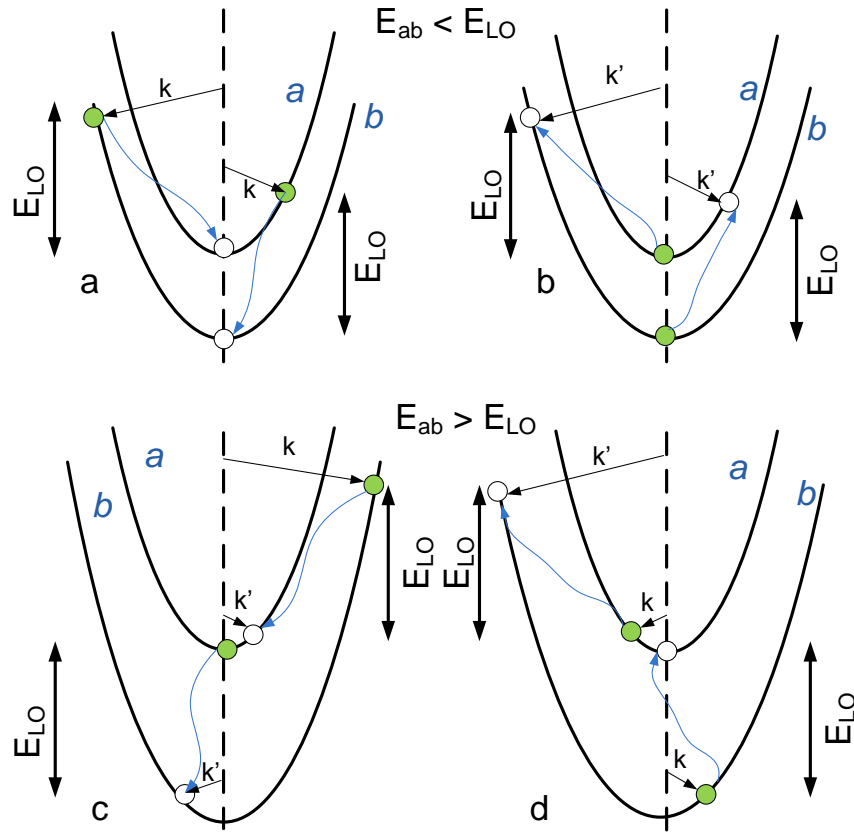


Figure 2.11: The intersubband LO-phonon scattering of the carrier. a) LO-phonon emission when the energy spacing between two subbands is less than the LO-phonon energy. b) LO-phonon absorption when the energy spacing between two subbands is less than the LO-phonon energy. c) LO-phonon emission when the energy spacing between two subbands is higher than the LO-phonon energy. d) LO-phonon absorption when the energy spacing between two subbands is higher than the LO-phonon energy.

Figure 2.11 shows four different cases for intersubband LO phonon scattering of carriers, a LO phonon is emitted in (a) and (c) and a LO phonon is absorbed in (b) and (d). Both LO-phonon emission and absorption can be discussed in two different situations which depend on energy spacing between two subbands.

- $E_{ab} < E_{LO}$:
If the energy spacing between two subbands is less than the phonon energy (figure 2.11. a, b), electron at Γ -point are not allowed to relax to lower subband through LO-phonon emission process. Only electrons that are thermally activated could have LO-phonon transition. There is a possibility for electrons in lower subband to emit LO-phonon to the upper subband if their temperature is so high (2.11.a). In this case, electron in both subband a and b can go to the next subband by LO-phonon absorption. As shown in Fig. 2.11. b, electron in Γ -point of the lower subband could jump to the upper subband by LO-phonon mechanism. There is a possibility for electron in upper subband to go to the lower subband by LO-phonon absorption mechanism (Fig. 2.11.b).
- $E_{ab} > E_{LO}$:
If the energy spacing between two subband is larger than the LO phonon energy (figure 2.11. c, d), LO-phonon emission will become dominant which occurs typically less than 1 ps. As shown in Fig. 2.11. c, the electron could relax to the lower subband even from Γ point of upper subband. The chance of LO-phonon emission from lower subband to upper subband is not zero, but it strongly depends on thermal excitation to higher-energy states (d). The LO-phonon absorption from Γ -point of the lower subband to the upper subband is forbidding since the energy spacing is more than phonon energy (Fig. 2.11.d).

In this section, a brief derivation of LO-phonon scattering time in polar semiconductor heterostructures, described in detail in [84], will be explained. For two dimensional carrier transport, the use of bulk phonon modes for GaAs is reasonably accurate. Based on aforementioned assumptions, the electron-phonon interaction Hamiltonian can be written as [84]

$$\mathcal{H} = e \sum_{\mathbf{K}} \left(\frac{\hbar\omega P}{2|\mathbf{K}|^2} \right)^{\frac{1}{2}} \frac{e^{j\mathbf{K}\cdot\mathbf{r}}}{V^{\frac{1}{2}}}, \quad (2.15)$$

where \mathbf{K} is phonon wave vector, ω is the angular frequency of the phonon, V is the volume of the crystal, and P is

$$P = \frac{1}{\epsilon_{\infty}} - \frac{1}{\epsilon_r}, \quad (2.16)$$

while $\epsilon_r = 12.91$ and $\epsilon_{\infty} = 10.92$ are the static dielectric constant and optical dielectric constant, respectively. By applying equation (2.15) to the *Fermi's Golden Rule*, the transition time between the initial subband and final subband can be calculated. As shown in Fig.

2.11, there are two possible transitions between subband a and b . The electron in initial subband i (It can be either a or b) can go to the final subband (It can be either a or b) by absorption or emission mechanism. If the initial and the final wave vectors are k_i and k_f , the phonon absorption and emission can happen when they satisfy equation (2.17).

$$E_f + \frac{\hbar^2 k_f^2}{2m^*} = E_i + \frac{\hbar^2 k_i^2}{2m^*} \pm \hbar\omega_{LO} \quad (2.17)$$

The positive and the negative signs represent LO phonon absorption and emission, respectively. After summation over all permitted initial and final states, shown in Fig. 2.11, the phonon absorption and emission rate can be determined by equation (2.18).

$$W_{i \rightarrow f} = \frac{m^* e^2 \omega P}{4\pi \hbar^2} (n_{LO} + \frac{1}{2} \mp \frac{1}{2}) \Theta(k_i^2 - \frac{2m^* \Delta}{\hbar^2}) \int_{-\infty}^{+\infty} \frac{|G_{if}(K_z)|^2}{\sqrt{K_z^4 + 2K_z^2(2k_i^2 - \frac{2m^* \Delta}{\hbar^2}) + (\frac{2m^* \Delta}{\hbar^2})^2}} dK_z, \quad (2.18)$$

where $\Delta = E_f - E_i \mp \hbar\omega_{LO}$, the upper and lower signs describe phonon absorption and emission, respectively. n_{LO} and $G_{if}(K_z)$ are the Bose-Einstein distribution factor and *form factor*, presented in equations (2.19) and (2.20), respectively.

$$n_{LO} = \frac{1}{e^{\hbar\omega/k_B T} - 1}, \quad (2.19)$$

$$G_{if}(K_z) = \int \psi_f^*(z) e^{-iK_z z} \psi_i(z) dz. \quad (2.20)$$

The initial- and final-state wavefucntions, ψ_i and ψ_f , in this system are real, then $|G_{if}(K_z)|^2$ is symmetric about $K_z = 0$ and hence it can be only calculated for positive K_z . the Heaviside function in equation (2.18) ensures that there are only finite lifetimes (non-zero rate) for absorption when

$$E_i + \frac{\hbar^2 k_i^2}{2m^*} + \hbar\omega > E_f, \quad (2.21)$$

and for emission:

$$E_i + \frac{\hbar^2 k_i^2}{2m^*} > E_f + \hbar\omega, \quad (2.22)$$

. Equation (2.18) gives the scattering rate of a carrier in a particular subband with a finite in-plane wave vector k_i into another subband through the assistance of a LO phonon. In reality, there is not only one carrier in the initial subband; there is a Fermi-Dirac distribution. It is then more useful to know the mean scattering rate (or lifetime) of a

carrier. we can use a simple weighted mean over the distribution of the carriers in the initial subband and calculate the scattering time by using

$$\frac{1}{\tau_{i \rightarrow f}} = \frac{\int W_{i \rightarrow f}(E)F(E)dE}{\int F(E)dE}, \quad (2.23)$$

where $F(E)$ denotes the Fermi-Dirac distribution. Since in THz QCL structures the doping concentration is low, the Boltzmann approximation can be employed for simplicity.

2.2.5.5 Interface Roughness Scattering

The source of the interface roughness mainly comes from the growth imperfection at the junction of two semiconductors. Independent of the growth methodology, the deposition of one alloy over another one causes a fluctuation in composition of the interface. Even though high-quality growth would reduce the surface roughness, we cannot have a perfectly flat interface with no fluctuation. In this section we introduce the method of calculating intersubband interface roughness scattering rate, which is borrowed from [87].

We assume the height of the roughness to be given by a function $\Delta(\mathbf{r})$ where $\mathbf{r} = (x, y)$ are the in-plane coordinates. We model the $\Delta(\mathbf{r})$ function by its auto-correlation function. We assume that the latter is Gaussian

$$\langle \Delta(\mathbf{r})\Delta(\mathbf{r}') \rangle = \Delta^2 \exp\left(-\frac{|\mathbf{r} - \mathbf{r}'|^2}{\Lambda}\right), \quad (2.24)$$

where Δ is the mean height of the roughness and Λ is the correlation length. The conduction band edge has an offset with absolute value of V_0 between two semiconductor alloy. The scattering matrix element is given by

$$\langle a\mathbf{k}'|H|b\mathbf{k} \rangle = \int F_{ab}\Delta(\mathbf{r})e^{i\mathbf{q}\cdot\mathbf{r}} d^2r, \quad (2.25)$$

where $\mathbf{q} = \mathbf{k} - \mathbf{k}'$ is the exchanged momentum. The strength of the interaction is given

$$F_{ab} = V_0\psi_a(z_0)\psi_b(z_0) \quad (2.26)$$

where z_0 is the position of the interface. Substituting equation (2.25) into equation (2.12) we can get

$$\Gamma_{\text{inter}}^{\text{IR}}(E) = \frac{m^*\Delta^2\Lambda^2}{\hbar^2}F_{ab}^2 \int_0^\pi e^{-\tilde{q}^2\Lambda^2/4} d\theta \quad (2.27)$$

where the absolute values of the 2D scattering vectors \tilde{q} is given by

$$\tilde{q}^2 = 2k^2 + \frac{2m^*E_{ab}}{\hbar^2} - 2k\sqrt{k^2 + \frac{2m^*E_{ab}}{\hbar^2}} \cos \theta. \quad (2.28)$$

The interface roughness scattering time can be determined by

$$\tau(E) = \hbar/\Gamma_{\text{inter}}^{\text{IR}}(E) \quad (2.29)$$

The same as what was presented for LO-phonon mechanism, equation (2.29) gives the scattering time of a carrier in a particular subband with a finite in-plane wave vector k with respect to scattering with an LO phonon into another subband. Substituting equation (2.29) into (2.23), the mean scattering time caused by interface roughness mechanism can be obtained.

2.2.5.6 Ionized impurity scattering

Quantum cascade structures base on III-V semiconductors alloys are doped with Si donors. The dopants are concentrated far from the optically active region to minimize the effect of reduced mobility and large optical losses at the laser transition energy caused by uniformly distributed dopants inside the structure. The distance between the optically active subbands and the doped region is therefore maximized. In mid-infrared QCLs, the dopants are typically located in a few layers in the middle of the injector region while in Tetahertz QCLs, the dopants are located either in injector barrier or injector well. Even though the dopants in the injector well in THz QCL would reduce the lifetime and affect the population inversion, there is no comprehensive study on how different doping position would affect the performance of THz QCLs [89, 90].

The scattering matrix element due to an ionized impurity at position Z is given by

$$\langle a\mathbf{k}'|H|b\mathbf{k}\rangle = \frac{e^2}{2\epsilon_0k_0q} \int \psi_a(z)\psi_b(z) e^{-q|z-Z|} dz. \quad (2.30)$$

Substituting equation (2.30) into equation (2.12), we have

$$\Gamma_{\text{inter}}^{\text{Ion}}(E) = \frac{m^*e^4}{4\pi\epsilon_0^2\epsilon_r^2\hbar^2} \int N(Z) \int \left[\frac{1}{\sqrt{\tilde{q}^2 + q_s^2}} \int \psi_a(z)\psi_b(z) e^{-\sqrt{\tilde{q}^2 + q_s^2}|z-Z|} dz \right]^2 d\theta dZ \quad (2.31)$$

where $N(Z)$ is the 3D impurity concentration at position Z and \tilde{q} is defined in equation (2.28). For inter-subband scattering the exchanged wave-vector is usually not zero. But the singularity \tilde{q}^2 may cause artificially high scattering rates in the vicinity of $q = 0$. We follow [91] by considering a screening wave-vector q_s . The latter is determined by a simple Debye model as:

$$q_s = \sqrt{\frac{e^2 N_s}{\epsilon_0 \epsilon_r k_B T_e}} \quad (2.32)$$

The intersubband scattering time due to ionized impurity mechanism can be calculated by

$$\tau(E) = \hbar / \Gamma_{\text{inter}}^{\text{Ion}}(E). \quad (2.33)$$

Finally, by substituting equation (2.33) into (2.23), the mean scattering time caused by ionized impurity mechanism can be obtained.

2.2.5.7 Dephasing time calculation

The dephasing time between two subband a and b can be determined by calculating the energy broadening between those states, as shown in equation (2.34). Since the dephasing time will be used in calculation of tunneling time in our rate equation formalism, explained in chapter 3, we used Γ_{tun} notation in our equation.

$$\Gamma_{\text{tun}}^{\text{ab}} = \frac{1}{2} \Gamma_{\text{intra}}^{\text{ab}} + \frac{1}{2} (\Gamma_{\text{inter}}^{\text{a}} + \Gamma_{\text{inter}}^{\text{b}}) \quad (2.34)$$

In equation (2.34), the intrasubband term can be written by

$$\Gamma_{\text{intra}}^{\text{ab}} = \sum_m \Gamma_{\text{intra}}^{\text{m-ab}}, \quad (2.35)$$

where m denotes a specific scattering mechanism. In this thesis, the intrasubband interface roughness and the intrasubband ion impurity scattering are included since those scattering are dominant in GaAs/AlGaAs based quantum well structures [87]. The intersubband term of the equation (2.34) for each states can be written as

$$\Gamma_{\text{inter}}^{\text{a}} = \sum_{i \neq a} \Gamma_{\text{inter}}^{\text{a} \rightarrow i}, \quad (2.36)$$

where i can be any states in one module of a THz QCL except a . In addition, the intersubband rate between two states in one module is the summation of all scattering mechanisms between those states, which is defined by

$$\Gamma_{\text{inter}}^{a \rightarrow i} = \sum_m \Gamma_{\text{inter}}^{m-a \rightarrow i}, \quad (2.37)$$

where m denotes a specific scattering mechanism. Finally the pure dephasing time can be defined as

$$\tau^* = 2\hbar/\Gamma_{\text{intra}}^{\text{ab}}, \quad (2.38)$$

In this thesis, the intersubband LO-phonon, intrasubband interface roughness, and the intersubband ion impurity scattering are included since those scattering rates are dominant in THz QCLs.

2.2.6 Oscillator strength calculation

The oscillator strength is a dimensionless quantity that indicates the strength of an optical transition. The gain of the transition between two subbands level is proportional to the oscillator strength. The value of the oscillator strength shows how those wavefunctions are overlapped in real space. A structure with an high oscillator strength will be called vertical transition while a design with a low oscillator strength is named diagonal transition. Even though some theoretical and experimental studies have been done to investigate the effect of oscillator strength on the performance of THz QCL, no clear conclusion can be easily drawn from the published works [92, 57].

The calculation method for oscillator strength in this thesis is based on the model presented in [93]. The oscillator strength follows the sum rule for all initial states "a" and for the sum over all final states "b" as

$$\sum_{a \neq b} f_{ab} = 1 \quad (2.39)$$

Equation (2.39) is valid when the effective mass of the structure is constant. Optical transitions between stationary states of a system (oscillator strength), defined as [93]

$$f_{ab} = \frac{2}{m^*} \frac{|\langle \Psi_a | P | \Psi_b \rangle|^2}{E_a - E_b} \quad (2.40)$$

where P is the momentum operator. If we consider the constant effective mass, equation (2.40) is simplified to

$$f_{ab} = \frac{2m^*\omega}{\hbar} Z_{ab}^2 \quad (2.41)$$

where Z_{ab} is the matrix dipole momentum between two states.

The nonparabolicity of the band will also affect the optical properties of the subbands. Based on the model presented in [93], an energy dependent effective mass was employed to collapse the nonparabolicity into a single band treatment using $\psi_c z$. By including the nonparabolicity effect, one can show, after some algebra, that the momentum matrix element in equation (2.40) is simply related to the conduction components of the total wavefunction as [93]

$$\langle \Psi_a | P | \Psi_b \rangle = \frac{1}{2} \langle \psi_c^a | p_z \frac{m_0}{m(E_a, z)} + \frac{m_0}{m(E_b, z)} p_z | \psi_c^b \rangle \quad (2.42)$$

The value of the oscillator strength, calculated by (2.42), is generally less than what is calculated by equation (2.41). In this thesis all oscillator strengths were calculated by equation (2.42) while non-extended wavefunctions were used for calculation.

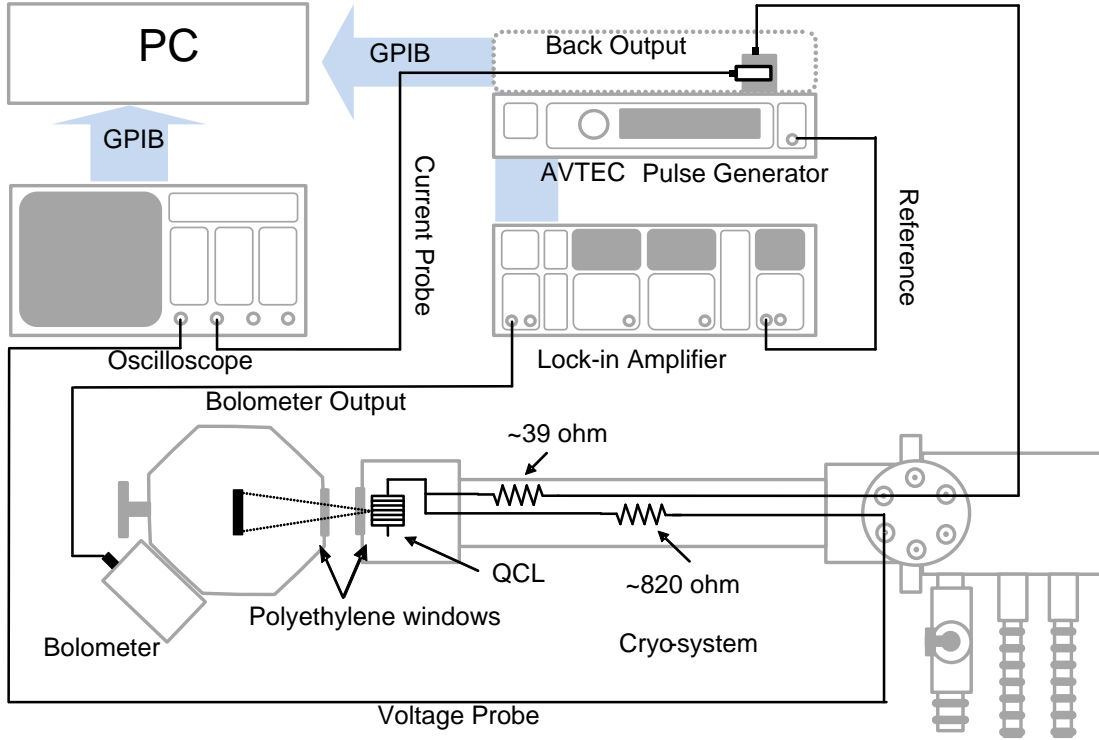


Figure 2.12: Schematic diagram of characterization setup for QCL LJV measurements.

2.3 Measurement setup

In this section of the thesis, the experimental setup, used to characterize THz QCLs, will be described. The current density and the output optical power of each device have to be collected at different electric fields and different temperatures. After we finalized the LJV measurement, the lasing frequency of the device will be determined by our spectral measurement setup.

2.3.1 Light-current density-voltage (LJV) setup

All QCL devices are mounted on a 7-pin package and placed in a closed cycle liquid Helium cooled cryostat for various measurements. There are two sensors in the Cryostat which read the temperature in two positions and connected to the temperature controller. A proportional-integral-derivative (PID) controller is used in system to set the temperature of the device in desired value. All parameters in temperature controller can be defined by Labview program to easily manage the measurement process. Two different detectors were used in our LJV measurement setup. A liquid-He cooled Silicon Bolometer (IR-lab Inc.) which has much higher sensitivity in THz frequency domain. Even though the sensitivity of this detector is high, It is not convenient for LJV measurement. The dewar of the detector has to be in vacuum. In addition it has to be cooled with liquid Helium which makes the preparation of the measurement process time consuming. There is another detector with lower sensitivity compared to the Silicon bolometer while it can be used in room temperature. I implemented both measurement setups in our lab and I characterized all devices with both detectors. The detector is managed to be as near as possible to the window of the cryostat to reduce the vapor absorption and increase the light collection efficiency.

Figure 2.12 shows the schematic diagram of LJV measurement setup. Since all the characterized devices are working in pulse mode, a high power pulse generation with a very small rising time is needed for this measurement setup. AVTECH (AVO-6C-B) pulse generator with a 1 KHz frequency and a 200 ns pulse width is used for LJV measurement by Bolometer. In the case of Golay cell, an extra pulse generator was used to modulate low frequency pulse (25 Hz), since the response time of Golay cell is not as fast as Bolometer. The circuit inside the cryostat consists of the injection current into the device and reading the voltage on top of the device. To have a nice pulse shape with a minimum overshoot and a fast rise time the injection current cable inside the cryostat was connected to a

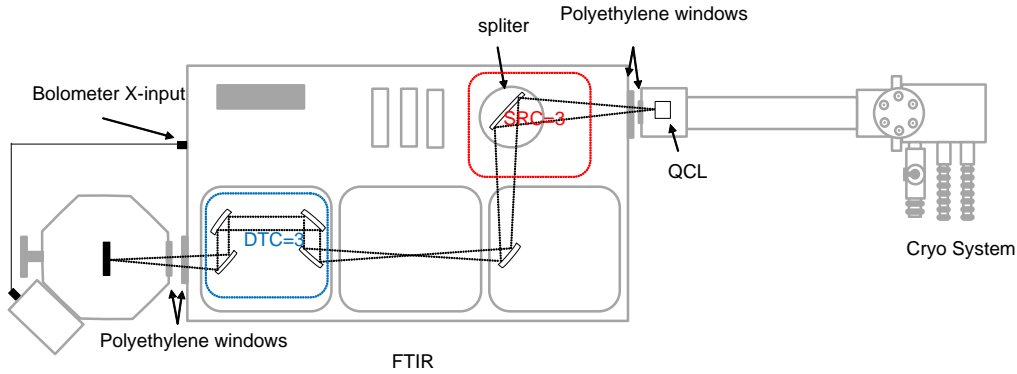


Figure 2.13: Schematic diagram of characterization setup for QCL spectroscopy measurement.

circuit with 39Ω resistance. This circuit will terminate the coaxial cable with almost 50Ω resistance to reduce the reflection pulse. Since the oscilloscope is terminated by a 50Ω resistance we cannot directly connect the coaxial cable to the Oscilloscope. A 820Ω resistance was used to reduce the current leaks into the oscilloscope not to damage our facility and not to affect the current measurement. To measure the current of the device a Tektronix current prob was connected to the pulse generator.

2.3.2 Spectrum measurement setup

Figure 2.13 shows the spectrum measurement setup which is used to determine the lasing frequency of the THz QCL. The circuit inside the cryostat will not change while the position of the detector and the arrangement of the optical setup will be different. The emission beam is coupled into a Bruker Fourier transform infrared spectrometer (FTIR) system. The spectrometer's computer reads the output of the Si bolometer at each position of the translating mirror and converts the data to spectrum through a Fourier transform. The THz QCL source is in one side of the FTIR system and the Bolometer detector is in the opposite side. To reduce the loss of THz wave, passing through all mirrors inside the FTIR, the FTIR system keeps in vacuum and all mirrors are perfectly aligned to maximize the collected light by Bolometer. A good vacuum system and a nice alignment setup would help us to do the spectral measurement near the maximum operating temperature.

2.4 Summary

In this chapter the important parameters that can affect the performance of both SISP and M-M waveguides were investigated. In addition, introducing the top metal gap in MM QCL increases the higher order modes' loss and suppress the excitation of higher-order modes except the fundamental mode. This enables steady optical/electrical characteristics such as smooth LI curves at the expense of slightly higher loss for the fundamental mode. This might slightly reduce T_{\max} [94], but makes the LI curve experimentally repeatable and better far-field emission pattern. It was found that the top metal gaps with width of 5 to 10 μm for ridges below 150 μm eliminates the higher order mode losses without significantly changing the fundamental mode loss. The effect of different metal process on temperature performance of THz QCL was assessed. The two-dimensional finite element method (FEM) was employed to calculate the waveguide loss of all structures. Since the quantum designs of all waveguides in this study were the same, the maximum operating temperature will be determined by the loss of the structure. In the second section of this chapter, important design parameters of a THz QCL were defined and the method of calculation was explained. The transfer matrix model (TMM) was used for energy state and wavefunction calculation of a multi-quantum well structures. The nonparabolicity effect in GaAs/AlGaAs was considered. The analytical expression of detuning, coupling, different scattering times (LO-phonon, interface roughness, ion impurity), pure dephasing time and oscillator strength were introduced. Finally, the experimental setup which is employed for characterization of THz QCL was presented.

Chapter 3

Transport Modeling of Indirectly-Pumped Terahertz Quantum Cascade Laser

In this chapter, we present the transport modeling, which is employed to predict the carrier distribution, current density, and gain spectrum in an IDP-THz QCL. To understand the detail of charge transport and to calculate optical gain, several theoretical models such as density matrix formalism, [95, 96, 55] nonequilibrium Greens function (NEGF), [97, 98, 99] and Monte Carlo techniques, [100, 101, 102] were employed. Each method has some pros and cons. Even though NEGF method includes all quantum effects in transport modeling, it is computationally intensive. In this thesis, A rate equation (RE) formalism, which is easy to implement and fast to calculate was used to simulate three different IDP QCLs. In addition, it could nicely predict the performance of IDP QCLs.

3.1 Rate equation model

The simplified RE model presents in this chapter does not self-consistently solve the electron temperature and the coupled Schrödinger-Poisson equation. We assume that the electron temperature is constant in all subbands and 50 K higher than that of the lattice temperature [60]. This assumption could help us to predict the performance of our IDP structures in terms of current density and gain estimation as long as the injection barrier of the structure is thick enough. Solving the coupled Schrödinger-Poisson equation, a

technique which is generally used in transport modeling of Mid-IR QCL, can be ignored in THz QCL structures with minimal effect on simulation results due to a very low doping concentration of THz active region (The active region of THz QCL structures are generally doped an order of magnitude lower than that of Mid-IR QCLs).

Independent of the number of the states included in our RE model, the equation can be written as

$$\frac{d\rho_i(t)}{dt} = -\frac{\rho_i(t)}{\tau_i} + \sum_j \frac{\rho_j(t)}{\tau_{j \rightarrow i}} \quad (3.1)$$

The total lifetime of subband i , as mentioned in equation (2.36), is $\tau_i^{-1} = \sum_{i \neq j} \tau_{i \rightarrow j}^{-1}$. This transition from states i to all other states includes either all intersubband transition mechanisms discussed in chapter two (LO-phonon, ion impurity, and interface roughness scattering) or the tunneling time between two modules.

3.2 Simplified model for an IDP QCL

We can simplify the general equation (3.1) to analyze an IDP QCL. This simplification helps us to investigate the effect of different scattering times and the thickness of some wells or barriers on performance of the structure. If we assume that the injector barrier of the structure is thick enough to eliminate injecting carrier to some states far from the ground state (which is valid in most of the design) and we assume that most of the carriers in each module accumulate in lowest state of each module, we can conclude with a simple model which only includes one tunneling between two modules. Using a thick injector barrier also reduces the injection of carrier to higher states in each module. To specify our equations, we can start our model with an IDP-QCL, presented in [60]. The schematic diagram of this IDP-QCL which includes the main scattering times, detuning, and coupling strength between two modules at an electric field near the alignment electric field is shown in Fig. 3.1.

The rate equations of this four-level system for two cascade modules will be written.

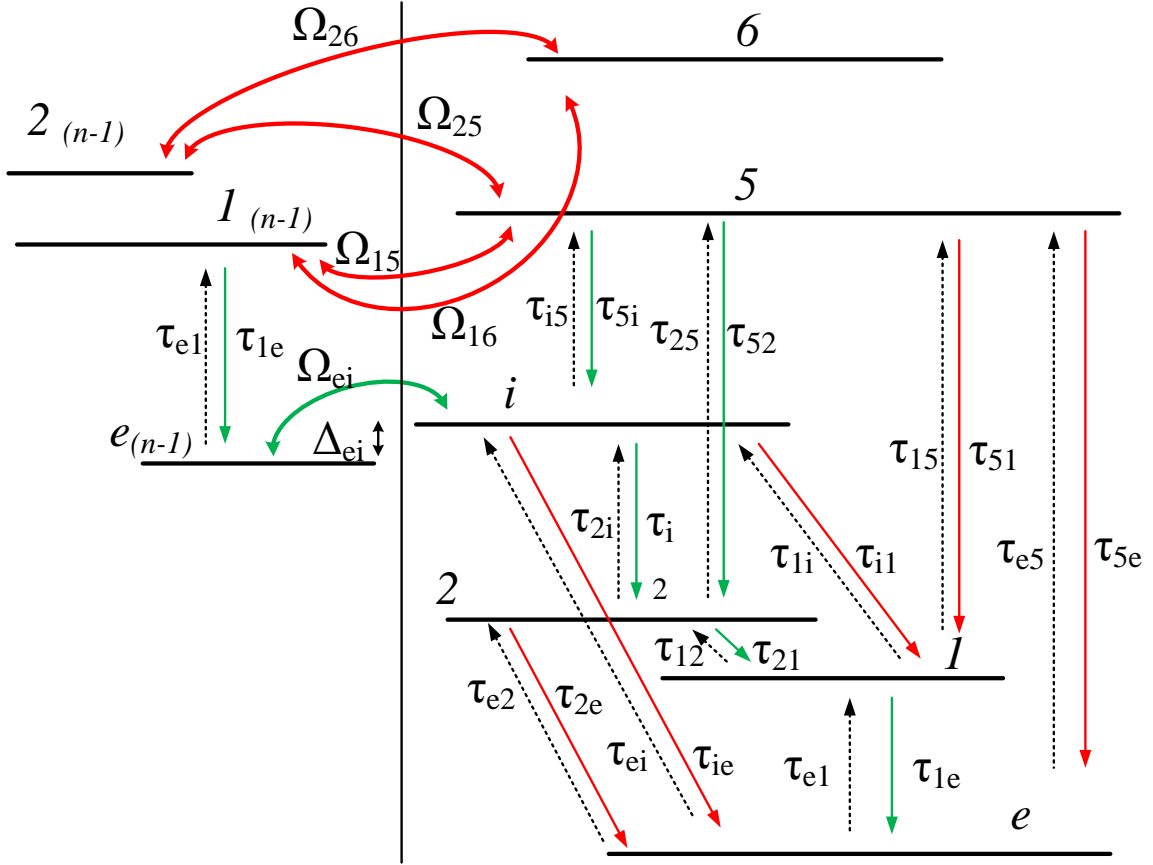


Figure 3.1: Schematic diagram of an IDP QCL active region based on a phonon-photon configuration. Throughout this thesis and whatever the electric field, the states within a module are labeled in energy ascending order e , 1 , 2 , and i . The solid lines show the forward scatterings, while the dashed lines indicate the back scatterings. Δ and Ω are the detuning and the coupling between two states, respectively. The green lines indicate the correct injection and extraction, while the red lines show the wrong injection and extraction in each module. 2 and 1 are the ULS and LLS, respectively.

$$\begin{aligned}
\frac{d\rho_e(t)}{dt} &= -\frac{\rho_e(t)}{\tau_e} - \frac{\rho_e(t)}{T_{ei}} + \frac{\rho_1(t)}{\tau_{1e}} + \frac{\rho_2(t)}{\tau_{2e}} + \frac{\rho_i(t)}{\tau_{ie}} + \frac{\rho_i(t)}{T_{ie}} \\
\frac{d\rho_1(t)}{dt} &= \frac{\rho_e(t)}{\tau_{e1}} - \frac{\rho_1(t)}{\tau_1} + \frac{\rho_2(t)}{\tau_{21}} + \frac{\rho_i(t)}{\tau_{i1}} \\
\frac{d\rho_2(t)}{dt} &= \frac{\rho_e(t)}{\tau_{e2}} + \frac{\rho_1(t)}{\tau_{12}} - \frac{\rho_2(t)}{\tau_2} + \frac{\rho_i(t)}{\tau_{i2}} \\
\frac{d\rho_i(t)}{dt} &= \frac{\rho_e(t)}{\tau_{ei}} + \frac{\rho_e(t)}{T_{ei}} + \frac{\rho_1(t)}{\tau_{1i}} + \frac{\rho_2(t)}{\tau_{2i}} - \frac{\rho_i(t)}{\tau_i} - \frac{\rho_i(t)}{T_{ie}}
\end{aligned} \tag{3.2}$$

where τ_{ij} is the intersubband scattering time between states i and j in one module (the detail of intersubband scattering time was presented in chapter 2.), T_{ij} is the tunneling time between states i and j while they are not in same module. If we assume the first order tunneling (The rate of tunneling is independent of the distribution of the carriers in each state), the tunneling time can be calculated by

$$T = (1 + \Delta^2 \tau_{\parallel}^2) / 2\Omega^2 \tau_{\parallel} \tag{3.3}$$

where $\hbar\Delta$ and $\hbar\Omega$ are the detuning energy and the coupling strength between two states and τ_{\parallel} denotes the dephasing time. The detail of calculation of detuning, coupling, and dephasing time was explained in section 2.2.4 and 2.2.5.7, respectively. In equation (3.2), if we assume that the system is in the steady state and the carrier density in each state is time independent, we can simplify the equation and re-write it in the matrix format, yielding

$$\begin{pmatrix} -\tau_e^{-1} - T_{ei}^{-1} & \tau_{1e}^{-1} & \tau_{2e}^{-1} & \tau_{ie}^{-1} + T_{ie}^{-1} \\ \tau_{e1}^{-1} & -\tau_1^{-1} & \tau_{21}^{-1} & \tau_{i1}^{-1} \\ \tau_{e2}^{-1} & \tau_{12}^{-1} & -\tau_2^{-1} & \tau_{i2}^{-1} \\ \tau_{ei}^{-1} + T_{ei}^{-1} & \tau_{1i}^{-1} & \tau_{2i}^{-1} & -\tau_i^{-1} - T_{ie}^{-1} \end{pmatrix} \times \begin{pmatrix} \rho_e \\ \rho_1 \\ \rho_2 \\ \rho_i \end{pmatrix} = \begin{pmatrix} 0 \\ 0 \\ 0 \\ 0 \end{pmatrix}, \tag{3.4}$$

In this 4×4 matrix, one of the equation is linearly dependent of the others. We replaced one line of this matrix by the charge conservation law ($\rho_e + \rho_1 + \rho_2 + \rho_i = 1$). The carrier density of each state can be easily calculated by solving the inverse of 4×4 matrix. If we further simplify our calculation by ignoring all back scatterings (dashed-lines in Fig. 3.1), we can obtain some analytical expressions for population inversion, differential resistance, internal quantum efficiency, and current density of the structure.

When the device is below the threshold and the stimulated emission rate is zero ($\tau_{sti} = \infty$), the normalized population inversion can be derived as

$$\rho_2 - \rho_1 = \frac{\tilde{\tau}_{2\text{eff}}}{\tau_{\text{tun}} + \tau_{\text{tr}}^<} \tag{3.5}$$

where $\tilde{\tau}_{2\text{eff}}$ is *modified effective lifetime* of the upper lasing state, defined as

$$\tilde{\tau}_{2\text{eff}} = \tau_{1e}\tau_2\tau_i \left(\frac{1}{\tau_{i2}} \frac{\tau_{21} - \tau_{1e}}{\tau_{1e}\tau_{21}} - \frac{1}{\tau_2\tau_{i1}} \right) \quad (3.6)$$

and $\tau_{tr}^<$ is the transit time without stimulated emission, the average time for electrons passing through one module excluding the tunneling time, defined as

$$\tau_{tr}^< = \tau_{1e}\tau_2\tau_i \left(\frac{1}{\tau_{i2}} \frac{\tau_{1e} + \tau_{21}}{\tau_{1e}\tau_{21}} + \frac{1}{\tau_2} \frac{2\tau_{i1} + \tau_{1e}}{\tau_{1e}\tau_{i1}} \right) \quad (3.7)$$

The population of level i and e , which have the main contribution to current density of the device, can be presented by

$$\rho_e = \frac{\tau_{\text{tun}} + \tau_i}{\tau_{\text{tun}} + \tau_{tr}^<} \quad (3.8)$$

$$\rho_i = \frac{\tau_i}{\tau_{\text{tun}} + \tau_{tr}^<} \quad (3.9)$$

If the injector barrier is thick enough, the individual wavefunction in each module does not expand to the next module. In this case, the intersubband scattering between state from different modules can be ignored and the current density can be determined by calculating the tunneling current across the injector barrier. This tunneling current depends on carrier population of the level i and e as well as the tunneling time between these states, which is given by

$$J^< = eN_{2D} \frac{\rho_e - \rho_i}{\tau_{\text{tun}}} \quad (3.10)$$

where N_{2D} is the two-dimensional carrier density per module. By substituting equation (3.8) and (3.9) into equation (3.10), the current density will be simplified to

$$J^< = \frac{eN_{2D}}{\tau_{\text{tun}} + \tau_{tr}^<} \quad (3.11)$$

If we assume that all carrier leakage channels can be ignored (τ_{i1} , τ_{2e} , and τ_{ie} are sufficiently long—which may not be always valid—), the transit time and the population inversion—without stimulated emission—can be simplified to $\tau_{tr}^< \approx 2\tau_{i2} + \tau_{21} + \tau_1$ and $\Delta\rho \approx (\tau_{21} - \tau_1)/(\tau_{\text{tun}} + \tau_{tr}^<)$, respectively. If we could increase the transition time between lasing states, τ_{21} , (e. g. in a very diagonal transition structure) to be much longer than all other transitions (such as intersubband transition times and tunneling time), the population inversion of near 100% is achievable ($\Delta\rho \approx \tau_{21}/\tau_{21} = 1$). This is the largest advantage of an IDP-QCL over a RT-QCL design. In ideal case, the maximum population

inversion in a RT-QCL is no more than 50%. In addition, in IDP QCLs, we can reduce the accumulation of the carrier at level e by reducing the tunneling time. This could minimize the back scattering to the LLS, which is another problem encountered in RT QCLs. Short tunneling time can be achieved by either narrowing the injector barrier or engineering the wavefunctions so that $\tau_{\text{tun}} \ll \tau_i$.

For a lasing device, at a current density higher than threshold current density, the population inversion is pinned to $\Delta\rho_{\text{th}}$ in the presence of stimulated emission. At the threshold, the optical gain equals to cavity loss. The current density above threshold can be written as

$$J^> = eN_{2D} \frac{1 - \Delta\rho_{\text{th}} \frac{\tau_{2e} - \tau_{1e}}{\tau_{2e} + \tau_{1e}}}{\tau_{\text{tun}} + \tau_{\text{tr}}^>} \quad (3.12)$$

where $\tau_{\text{tr}}^>$ is the transit time with stimulated emission and is defined as

$$\tau_{\text{tr}}^> = 2\tau_i \left(1 + \frac{\tau_{1e}\tau_{2e}(\tau_{i2} + \tau_{ie})}{\tau_{i2}\tau_{ie}(\tau_{1e} + \tau_{2e})} \right) \quad (3.13)$$

Another important performance indicator is the discontinuity in differential resistance at threshold. This parameter can determine the output power and the current dynamic range. The relative differential resistance discontinuity at threshold is defined by

$$\frac{\Delta R_{\text{th}}}{R_{\text{th}}} = \frac{R_{\text{th}}^> - R_{\text{th}}^<}{R_{\text{th}}^<} = \Delta\rho_{\text{th}} \frac{\tau_{2e} - \tau_{1e}}{\tau_{2e} + \tau_{1e}} \quad (3.14)$$

Since the current density before threshold depend on transit time ($\tau_{\text{tr}}^<$), and it mostly affected by intersubband transition between lasing states. Above threshold, more current flows through due to stimulated emission, leading to a decrease in differential resistance. In deriving equation (3.14) we employed two assumptions. First, we assumed that the population inversion, near the threshold point, is voltage independent (constant product of oscillator strength and gain bandwidth). Secondly, we assumed that the transit times (before and after threshold) and $\frac{\tau_{2e} - \tau_{1e}}{\tau_{2e} + \tau_{1e}}$ are not heavily voltage dependent. These assumptions may not be always valid (for example, in highly diagonal structure); but equation (3.14) gives us a simple and straightforward guideline for design an active region.

All aforementioned equations show directly the effect of different scattering times on the performance of the quantum structure. More details will be provided in chapter 4, when the simulation results of three different THz IDP-QCLs. we will show how to improve the device design by defining a reasonable figure of merit. In the next section of this chapter, we present the actually implemented rate equation model in this PhD project and investigate the first- and the second-order tunneling mechanism in THz IDP-QCL. Finally we define a simple gain equation model which is employed to calculate the gain of different

designs.

3.3 Implemented rate equation model for IDP structures

The analytical expressions, presented in section 3.2, provide a good guideline in designing IDP QCLs, they cannot accurately predict the behavior of the laser in many cases. In this section we will present a RE model that includes the first 6 states of one module. The RE equation are then simultaneously solved for three consecutive cascade modules through a numerical approach. The tunneling channels between any two states are included. Figure 3.2 shows the schematic diagram of the energy levels and all relevant scattering processes in this model. The intersubband scattering times (which are not shown in Fig. 3.2) are the same as those shown in Fig. 3.1. The RE model for these three modules can be determine by including all 6 states and the corresponding detuning and coupling in equation (3.1). In steady state situation, the carrier density in each state will be time independent. We can simplify the equation and re-write it in a martix format. The final equation that has to be calculated is defined by

$$\begin{pmatrix} -\tau_e^{-1} - T_e^{-1} & \tau_{1e}^{-1} + T_{1e}^{-1} & \tau_{2e}^{-1} + T_{2e}^{-1} & \tau_{ie}^{-1} + T_{ie}^{-1} & \tau_{5e}^{-1} + T_{5e}^{-1} & \tau_{6e}^{-1} + T_{6e}^{-1} \\ \tau_{e1}^{-1} + T_{e1}^{-1} & -\tau_1^{-1} - T_1^{-1} & \tau_{21}^{-1} + T_{21}^{-1} & \tau_{i1}^{-1} + T_{i1}^{-1} & \tau_{51}^{-1} + T_{51}^{-1} & \tau_{61}^{-1} + T_{61}^{-1} \\ \tau_{e2}^{-1} + T_{e2}^{-1} & \tau_{12}^{-1} + T_{12}^{-1} & -\tau_2^{-1} - T_2^{-1} & \tau_{i2}^{-1} + T_{i2}^{-1} & \tau_{52}^{-1} + T_{52}^{-1} & \tau_{62}^{-1} + T_{62}^{-1} \\ \tau_{ei}^{-1} + T_{ei}^{-1} & \tau_{1i}^{-1} + T_{1i}^{-1} & \tau_{2i}^{-1} + T_{2i}^{-1} & -\tau_i^{-1} - T_i^{-1} & \tau_{5i}^{-1} + T_{5i}^{-1} & \tau_{6i}^{-1} + T_{6i}^{-1} \\ \tau_{e5}^{-1} + T_{e5}^{-1} & \tau_{15}^{-1} + T_{15}^{-1} & \tau_{25}^{-1} + T_{25}^{-1} & +\tau_{i5}^{-1} + T_{i5}^{-1} & -\tau_5^{-1} - T_5^{-1} & \tau_{65}^{-1} + T_{65}^{-1} \\ \tau_{e6}^{-1} + T_{e6}^{-1} & \tau_{16}^{-1} + T_{16}^{-1} & \tau_{26}^{-1} + T_{26}^{-1} & +\tau_{i6}^{-1} + T_{i6}^{-1} & \tau_{56}^{-1} + T_{56}^{-1} & -\tau_6^{-1} - T_6^{-1} \end{pmatrix} \times \begin{pmatrix} \rho_e \\ \rho_1 \\ \rho_2 \\ \rho_i \\ \rho_5 \\ \rho_6 \end{pmatrix} = \begin{pmatrix} 0 \\ 0 \\ 0 \\ 0 \\ 0 \\ 0 \end{pmatrix}, \quad (3.15)$$

where T_{ij}^{-1} consists of tunneling times from level i of module n to the level j of module $n+1$ and level j of module $n-1$. It can be calculated by

$$T_{ij}^{-1} = T_{i_n \rightarrow j_{n+1}}^{-1} + T_{i_n \rightarrow j_{n-1}}^{-1} \quad (3.16)$$

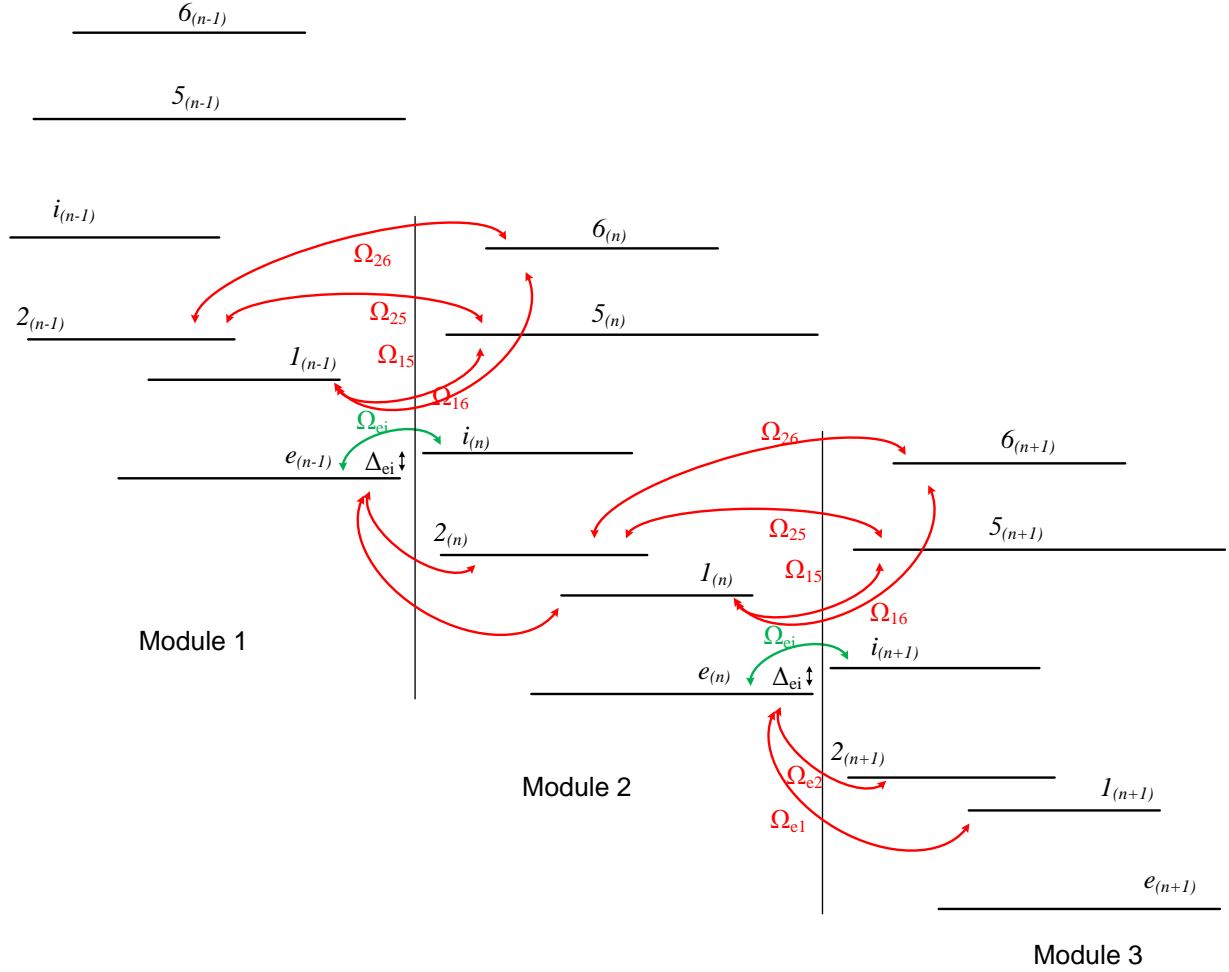


Figure 3.2: Schematic diagram of three cascade IDP QCL active region based on a phonon-photon-phonon configuration. The main coupling between states are indicated in figure. The green arrows and the red arrows show the desired and undesired coupling strength, respectively. Even though the coupling between all 6 states of the left module and all 6 state of the middle and right module were included in our RE model, the main coupling which drastically affect the current density and the gain are plotted. Ω and Δ are the coupling strength and detuning energy between states.

T_i^{-1} in equation (3.15) is the summation of all tunneling rates from state i of module n to all other states in modules $n-1$ and $n+1$ and can be defined as

$$T_i^{-1} = \sum_{j \neq i} T_{ij}^{-1} \quad (3.17)$$

The same procedure, employed in equation (3.4), will be applied to equation (3.15) to find the population of each state. After calculating the population of each state, we can calculate the current density and the gain spectrum of the device at different electric field and temperatures which will be explained in the following sections.

3.4 Current density calculation

In this section, we explain the calculation method for current density of IDP QCLs. We first introduce the current density calculation of a simple resonant tunneling structure [34]. The first- and second-order tunneling methods will then be presented and implemented for an IDP QCL.

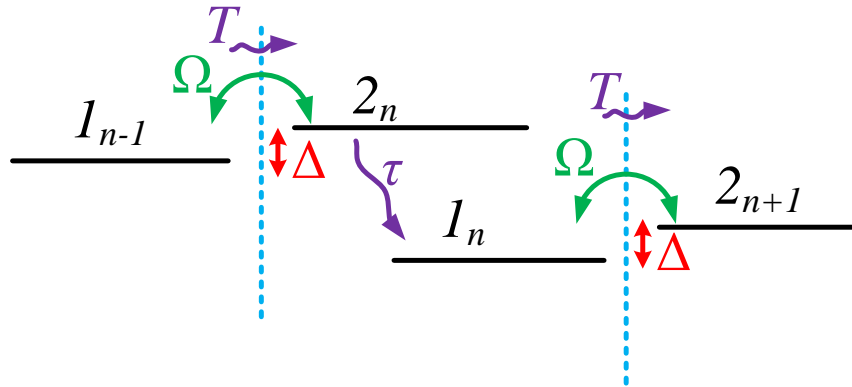


Figure 3.3: Schematic diagram of a two-level system. Δ and Ω are the detuning energy and the coupling strength between states 1_n and 2_{n+1} . τ is the non-lasing transition lifetime of level 2_n . T is the tunneling time between states 1_n and 2_{n+1} .

3.4.1 Resonant tunneling in a two level system

Figure 3.3 shows the schematic diagram of a two-level system at an electric field near the alignment of states 2_{n-1} and 1_n . At the alignment electric field, the ground state of module n (1_n) will be in resonance with second state of module $n+1$ (2_{n+1}). The detuning energy and the coupling energy between those states can be calculated by equation (2.11). The non-lasing transition lifetime between level 2_n is the intersubband transition time between level 2_n and 1_n which was discussed in detail in chapter 2. The tunneling time between level 1_n and 2_{n+1} is given as

$$T_{\text{tun}} = \frac{1 + \Delta_{12}^2 \tau_{\parallel 12}^2}{2\Omega_{12}^2 \tau_{\parallel 12}} \quad (3.18)$$

where Δ is the detuning and Ω is the coupling between levels 1 and 2 . The tunneling time, calculated by equation (3.18) is based on a first-order tunneling mechanism. If we employ the RE model for this simple structure, the population of each state, the population inversion, and the current density can be easily determined. Equation (3.5) shows the population difference between level 2 and 1 while equation (3.20) gives the current density across the barrier.

$$\Delta_n = \rho_2 - \rho_1 = \frac{-T}{2\tau + T} \quad (3.19)$$

$$J = eN_{2D} \frac{\rho_1 - \rho_2}{T} \quad (3.20)$$

where T and τ are the tunneling time and non-lasing scattering time between levels 2 and 1 . Since both the tunneling time and the non-lasing scattering time are positive, the population inversion of two-level system is always negative. Combining equations (3.18), (3.19), and (3.20), the current density is reduced to

$$J = eN_{2D} \frac{2\Omega_{12}^2 \tau_{\parallel 12}}{1 + \Delta_{12}^2 \tau_{\parallel 12}^2 + 4\Omega_{12}^2 \tau_2 \tau_{\parallel 12}} \quad (3.21)$$

which is exactly the same as presented in [103] for a two level system. As shown in equation (3.21), the current will be maximized when levels 1_n and 2_{n+1} are aligned ($\Delta_{12} = 0$). In this case, current density calculation can be further simplified under two extreme situations:

- Strong coupling injection: if the coupling injection is high enough ($4\Omega_{12}^2 \tau_2 \tau_{\parallel 12} \gg 1$), the current density is independent of the coupling strength injection and only depends on life time of state 2 ($J \approx \frac{eN_{2D}}{2\tau_2}$). Most of high performance THz QCLa are working in this regime at alignment electric field. This regime, called coherent regime, ensures fast electron injection in the upper state without being limited by the tunneling rate.

- Weak coupling injection: if the coupling injection is low ($4\Omega_{12}^2\tau_2\tau_{\parallel 12} \ll 1$), the current density will depend on coupling strength injection and pure dephasing time ($J \approx 2eN_{2D}\Omega_{12}^2\tau_{\parallel 12}$). In this situation, only a small fraction of electrons tunnel through the barrier. Most of carrier injection before the alignment electric field are in this regime which is called incoherent regime.

Coherent and incoherent regimes in different IDP structures and their effects on device performance will be investigated in detail in chapter 4.

3.4.2 First-order current density calculation

As discussed in section 3.2, the current density between two states a and b can be determined by

$$J = \frac{2\Omega_{ab}^2\tau_{\parallel ab}}{1 + \Delta_{ab}^2\tau_{\parallel ab}}(\rho_a - \rho_b) \quad (3.22)$$

In our rate equation model, we can calculate the population of each state at different electric fields and temperatures. By having the population of each state, the current density between each two state can be calculated by equation(3.22). The current density of the model, shown in Fig. 3.2, is defined as

$$J = \sum_{a=1}^N \sum_{b=1}^N \frac{\rho_a - \rho_b}{T_{tun(a \rightarrow b)}} = \sum_{a=1}^N \sum_{b=1}^N \frac{2\Omega_{ab}^2\tau_{\parallel ab}}{1 + \Delta_{ab}^2\tau_{\parallel ab}}(\rho_a - \rho_b) \quad (3.23)$$

where N is the number of states (6 in our modeling) which are included in RE formalism. In most of IDP QCLs, presented in this thesis, only first four states are effectively involved in carrier transport. Even though all first six levels were included in our RE modeling, level 5 and 6 were ignored in some structures due to their negligible effects on current density and gain calculation. Since the carrier population of ground state of each module is high, the tunneling current from this state to all other states has the major contribution in total current density. If the injector barrier of IDP structure is thick enough to prevent injecting carriers to states 5 and 6, one can show that the current density can be simplified as

$$J = \sum_{j=2}^4 \frac{\rho_1 - \rho_j}{T_{tun(1 \rightarrow j)}} = \sum_{j=2}^4 \frac{2\Omega_{1j}^2\tau_{\parallel 1j}}{1 + \Delta_{1j}^2\tau_{\parallel 1j}}(\rho_1 - \rho_j) \quad (3.24)$$

There are three terms in equation (3.24). A desired design will be a structure with an highly incoherent tunneling current in first two terms (for $j=2$ and 3) and highly coherent

tunneling current in last term ($j=4$). There is a trade off and it can not be easily satisfied. As mentioned in [104, 105], the first-order tunneling model is not an accurate model to predict the current density, since the carrier injection rate also depends on the distribution of carrier in each state. Our calculation shows that the current density of the device is non-zero at zero electric field due to Lorentzian shape of the current (first order approximation). To solve this issue, we will introduce the second-order tunneling current model which will be discussed in the next section.

3.4.3 Second-order current density calculation

The effect of carrier distribution in each state on tunneling current between two states is shown in figure 3.4. Let's consider two different situations of the tunneling between states a and b , given that we know the intrasubband distribution of the carriers in the subband a and b as a function of kinetic energy. In the first case ($\Delta_{ab} < 0$) only a fraction of electrons in the state a that have enough kinetic energy (the red circles) can contribute in tunneling from state a to b and electrons with low kinetic energy (the blue circles) cannot tunnel. However, all electrons in state b (the green circles) are allowed to tunnel to state a . In the second case ($\Delta_{ab} > 0$), all electrons from state a can tunnel to the states b while only hot electrons in state b can contribute to tunneling current from state b to a . To include the effect of second-order tunneling in our modeling, the effective coupling can be defined as

$$J_{ab} = \frac{2\Omega_{ab}\tau_{||ab}}{1 + \Delta_{ab}^2\tau_{||ab}^2} (\overline{\Omega_{ab}\rho_a} - \overline{\Omega_{ba}\rho_b}) \quad (3.25)$$

where $\overline{\Omega_{ab}}$ and $\overline{\Omega_{ba}}$ are the effective coupling and depend on the detuning energy between the two levels and the carrier distribution of each state. We can define a parameter, which is a function of detuning energy and distribution of the electron to explain the effective coupling parameter:

$$\sigma_b(\Delta_{ab}) = \Theta(-\Delta_{ab}) + \Theta(\Delta_{ab})N_b^{-1}D_\epsilon \int_{\hbar\Delta_{ab}}^{\infty} f_b(\epsilon)d\epsilon \quad (3.26)$$

where Θ is the Heaviside function (This function was used in calculation of LO phonon scattering too (equation (2.18)). To avoid the discontinuity in tunneling rate when detuning energy is zero, we introduce the Heaviside function the same as what MATLAB software defined ($\Theta(0) = 0.5$). D_ϵ is the density of states and N_b is the total population of subband b which is defined as $N_b = D_\epsilon \int_0^\infty f_b(\epsilon)d\epsilon$. Fermi-Dirac distribution, $f_{FD}(\mu, \beta, \epsilon) = (1 + \exp(\beta(\epsilon - \mu)))^{-1}$, is a good approximation for f_b in quantum cascade lasers, where μ is

the Fermi-level and $\beta = 1/k_B T$. Since in THz QCLs the doping concentration is an order of magnitude lower than that of MIR QCL, the Boltzmann distribution is a good approximation to replace Fermi-Dirac distribution in equation (3.26)

Finally, we can define the effective coupling as a function of σ :

$$\overline{\Omega_{ab}} = \Omega_{ab}\sigma_a(\Delta_{ba}) \quad \text{and} \quad \overline{\Omega_{ba}} = \Omega_{ab}\sigma_b(\Delta_{ab}) \quad (3.27)$$

where Ω_{ab} is the coupling strength between levels a and b . In second-order tunneling current model, the distribution of electrons in each subband, Which is largely relies on electron temperature(T_e), can drastically affect on current density. As we did not use the self-consistent model to estimate the electron temperature of each subband separately, the calculation of the current density by using this second-order model could still be quite off the target. The comparison between the first- and the second-order tunneling model for three different IDP THz QCLs will be discussed in detail in chapter 4.

3.5 Gain calculation in IDP THz QCLs

Since in all IDP THz QCLs, that are addressed in this study, neither the upper lasing state is in resonance with a state in module nor the lower lasing state, the broadening of the gain spectrum due to resonant tunneling effect can be ignored. The gain of the structure can be simply estimated by multiplying the dipole momentum between the lasing state (or the oscillator strength) and the population inversion between lasing states. Even though the full-width-half-maximum (FWHM) of the structure can be estimated by including the intrasubband scattering time between the lasing state (As discussed in chapter 2), it is safe to assume 1 THz for all structures presented in this thesis.

The optical absorption coefficient for a given photon energy between states a and b can be determined using *Fermi's golden rule* which is [3]:

$$\alpha(\hbar\omega) = \frac{\pi e^2}{n_r c \epsilon_0 (m^*)^2 \omega} \frac{2}{V} \sum_{k_a} \sum_{k_b} |\hat{e} \cdot P_{ab}|^2 \delta(E_a - E_b - \hbar\omega) (f_a - f_b) \quad (3.28)$$

where P_{ab} is the momentum matrix element, c is the speed of light in vacuum, V is the volume of the material interacting with optical field, and n_r is the refractive index of the material (3.6 for GaAs system). The delta function in equation (3.28) can be replaced by an either a Lorentzian or Gaussian function in presence of scattering relaxations, yielding

$$\alpha(\hbar\omega) = \frac{\pi e^2}{n_r c \epsilon_0 m^{*2} \omega} \frac{2}{V} \sum_{k_a} \sum_{k_b} |\hat{e} \cdot P_{ab}|^2 \frac{\Gamma/2}{(\Delta_{ab} - \hbar\omega)^2 + (\Gamma/2)^2} (f_a - f_b) \quad (3.29)$$

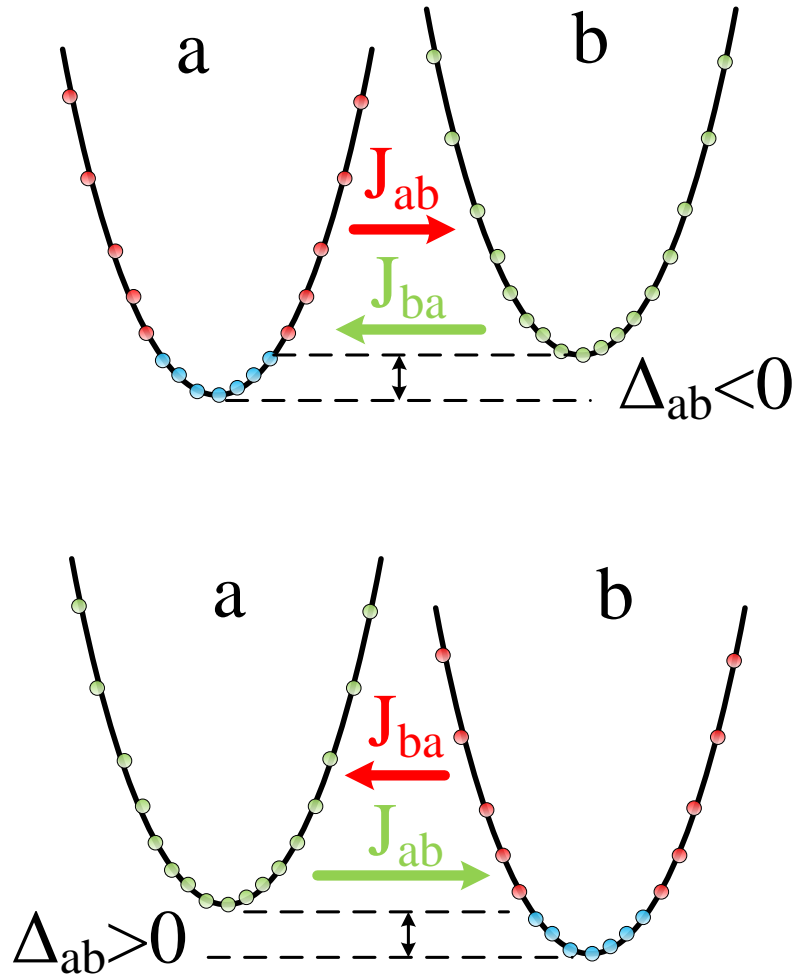


Figure 3.4: Different tunneling cases in two-level system. if the detuning energy is negative, only small fraction of electrons in state a which have enough kinetic energy (the red circles) can contribute in tunneling from state a to b and electrons with low kinetic energy (the blue circles) have no permission to tunnel, while all electron in state b (the green circles) have this opportunity to tunnel to state a . If the detuning energy is positive, all electrons from state a can tunnel to the states b while only hot electrons in state b contribute in tunneling mechanism from state b to a .

Substituting equation (2.40) into equation (3.29) and simplify the summation, the inter-subband gain coefficient can be defined as

$$g(\omega) = \frac{\pi \hbar e^2}{2n_r c \epsilon_0 m^*} f_{ab} \Delta N \mathcal{L}(\hbar\omega - \Delta_{ab}) \quad (3.30)$$

where \mathcal{L} is a Lorentzian function with FWHM of Γ and ΔN is the population inversion between the lasing states. As shown in equation (3.30), the gain of the structure depend on the oscillator strength and the population inversion between lasing states if we assume the broadening of the gain spectrum is independent of the design structure.

3.6 Summary

In this chapter a rate equation formalism was introduced to model the carrier transport in THz IDP-QCLs. Some simplifications were assumed to find an analytical expression for important parameters that play a critical role in design performance. The first- and second-order tunneling current models were explained and both of them will be employed to calculate the current density of the structure. Finally the gain calculation equation was presented and the key parameters that govern the gain of a quantum structure were discussed..

Chapter 4

Design and Analysis of Indirectly-pumped THz QCLs

A rate equation formalism was presented in chapter 3 to explain the carrier transport in THz IDP-QCL and to calculate the gain spectrum of the design. In this chapter, we propose three devices, based on a totally new lasing scheme, and investigate the performance of each design and compare them in terms of the optical power, threshold current density, intermediate resonance before the threshold, current dynamic range, differential resistance at threshold, lasing spectrum, and the maximum operating temperature. Since this is the first time that this design scheme is used for THz QCL active region, all aspects of the design must be carefully analyzed to ensure that the selected quantum structure will lase and its performance is comparable to or even higher than other proposed schemes. In the first part of this chapter we present the design strategy for each structure and analyze the theoretical calculation for each design. The growth and fabrication parameters will be introduced and finally the experimental results of those structure will be explained and analyzed. The comparison between our modeling and experiment will be shown in the last part of this chapter.

4.1 Design of THz IDP-QCLs

The limitations of RP-QCLs, discussed in detail in chapter 1, encouraged researchers to find a new approach to overcome those effects and open a new window to improve the

performance of THz QCLs. All IDP-QCLs, presented in this chapter, are based on phonon scattering injection to the upper lasing state and direct phonon relaxation from the lower lasing state. Since electrons experienced a consecutive phonon, photon, and phonon transition in each module, these IDP structures are also called phonon-photon-phonon (3P) QCLs. A simple design based on 3P-QCL can be a structure which includes four states in one module to accommodate these three transitions. If only the ground state of each well contributes to carrier transport, we need a minimum of four wells for a design based on 3P-QCL.

To understand how this scheme works, we can assume that the four-well structure consists of two phonon double wells separated by a radiative barrier. The more spatially overlapped wavefunctions in each double well lead to a faster phonon scattering process. In addition, the energy spacing of each double well should be as close as possible to the LO-phonon energy of GaAs (36.7 meV). The thickness of the radiative barrier strongly affects the oscillator strength, which, in turn, directly affects the gain and the population inversion. Even though there is no tunneling for carrier injection to the ULS and carrier depopulation from the LLS, the wrong injection and extraction channels still exist. To overcome this problem, those undesired scattering rates must be minimized to decrease the chance of the wrong injection to the LLS or non-radiative relaxation from the ULS. That is, the scattering times (red arrows in Fig. 3.1) must be increased. From the point of view of population inversion, the optimum structure of this scheme is a design that has a short τ_{i2} and τ_{1e} to maximize the correct injection and extraction, and secondly, a long τ_{i1} and τ_{2e} to minimize the wrong injection and extraction, respectively. In addition, it needs to have a fairly long relaxation time between the lasing states to keep the population inversion high enough even at higher temperatures. Therefore, in 3P structures all four eigenenergies and their corresponding wavefunctions have to be carefully and simultaneously tailored to efficiently inject carriers into ULS and extract them from LLS. To satisfy those requirements a genetic algorithm (GA) was employed to optimize the design candidates.

4.1.1 New design concerns

Three minor issues arise when the GA is employed to find the optimum structure.

1. The fifth energy state, which was not an issue in the RT structure, may play an adverse role in 3P designs. In a conventional THz RT-QCL, the total potential across one module, which equals the sum of a THz photon energy and a LO-phonon energy, is typically less than 57 meV (considering 36 meV for LO-phonon energy and maximum 21 meV for THz photon energy [47]). In a THz 3P-QCL, this energy spacing

increases to almost 90 meV so as to put the fifth energy state closer to the ULS and LLS of the previous (upstream) module at an electric field lower than the designed electric field. This situation can substantially enhance the leakage current through tunneling to this state and decrease the population inversion. In addition, this state can be a reason for early NDR if the injector barrier is thinned too much in order to reach a high maximum current. Moreover, as the injector state cannot be totally depleted, the dipole moment between levels i and 5 should be kept low in order to minimize the free-carrier absorption; [106, 107] this is typically achieved by a thick radiative barrier.

2. The six energy state of each module may also impact the performance of the structure. This energy state cannot be so low to be the reason of early NDR, but it can be the reason of leakage path from upper lasing state of the left module. we have to push the six energy state to be much higher than the upper lasing state of the left module. Since at low temperature, the upper lasing state is highly populated, electrons can escape to the sixth energy state of right module instead of lasing transition to the LLS. This may be avoided if the injector barrier of the structure is thick enough.
3. The third issue that must be noted is the effect of tunneling between level e of the left module and levels 2 or 1 of the right one. If this tunneling is stronger than that of levels e and i at the desired threshold electric field we may confront an early NDR, which could block the lasing operation of the structure or cause voltage instabilities.[57] It has been demonstrated that an IDP structure with a two-well injector can substantially reduce all resonances prior to the threshold. [65]

4.1.2 General parameters of 3P QCL design

Since the scheme of the 3P-QCL structure is different from that of the RP-QCL design, the range of the operating electric field, alignment electric field, and the growth material may change. Those parameters (They are typically called general design parameters since they need to be fixed first before any other design parameter can be determined) have to be carefully chosen to satisfy our requirements and to minimize the adverse effects.

4.1.2.1 Growth material

The growth materials for all 3P-QCLs in this thesis are the same and based on GaAs/ $\text{Al}_x\text{Ga}_{1-x}\text{As}$ material system. The only difference between this new scheme and most of high performance RP-QCLs, is the fraction of Aluminum in barriers. The Aluminum fraction in each design has to be carefully chosen to one the hand be high enough to reduce the escaping rate of the electron to the continuum band, and on the other hand should be low to reduce the effect of roughness scattering which may limit the performance of the device by either increasing the gain bandwidth or reducing the non-lasing transition time between the lasing states. As mentioned in section 4.1.1, the total potential across one module at desired electric field is almost 30 meV higher than that of RP-QCLs. This difference forces us to increase the height of the barrier. 15% Aluminum fraction, used in most high performance QCLs, is not enough any more to suppress the leakage current. In all THz 3P-QCLs, discussed in this thesis, the Aluminum fraction is 25% which makes the height of the barrier ~ 100 meV higher than that of the devices based on 15% Aluminum. This value can be lower if the lasing frequency is lower than 2 THz.[46] Since at low lasing frequency, the effect of roughness scattering is more dominant than that of high lasing frequency ($f > 4$ THz) devices, choosing an optimum barrier height is a challenging issue.

4.1.2.2 Alignment electric field

Alignment electric field of the device is the electric field at which the ground state of the module $n-1$ will be aligned with either the upper lasing state (in directly-pumped QCLs) or a state above the upper lasing state (in indirectly-pumped QCLs) of module n . It can be roughly determined by $\Delta V/L$ where L is the length of the module and ΔV is the total energy spacing between the ground state and the aligned state. The module length of the 3P-QCL is similar to that of a RP-QCL structure. Since the energy spacing between the aligned state and the ground state increases by $\sim 70\%$ in 3P QCLs, the alignment electric field will be 70% higher. The alignment electric fields of all 3P-QCLs, presented in this thesis, are 21 kV/cm. In the optimization process, to find the final thickness of the wells and the barriers, we can either fix the electric field to a specific value (for example 21 kV/cm) and tune the barrier and well thickness, or vice versa.

4.1.2.3 Doping concentration

We did not do any study on the doping concentration value and position in the active region design of 3P-QCLs. It has been shown that a doping position near the upper lasing

of the device not only does reduce the scattering time of the lasing states (increase the threshold current) but also increase the gain bandwidth of the design by lowering the pure dephasing time between the lasing states.[87] The position of the Si doping in the active region of all structures set to be far from the upper lasing state not to reduce the non-lasing scattering time of that state. It could be either in the middle of the injector barrier or the first well after the injector barrier. We choose this strategy based on a study that investigated the effect of doping value and migration on performance of RP-QCL.[53, 108] In this thesis, the value of the doping concentration was chosen not to be higher than 10^{16} cm^{-3} . The two-dimensional doping concentration of all 3P-QCLs are between $3 \times 10^{10} \text{ cm}^{-2}$ to $3.5 \times 10^{10} \text{ cm}^{-2}$.

Starting from next section (section 4.2), we will present our experimental and simulation results of three novel 3P-QCLs and will show how the device performance is gradually improved. At the end of this chapter, we compare those structures from different aspects to see the advantages and the weak points of each design. This analysis and comparison can help us to find a new approach to improve the performance of this new design scheme.

4.2 First 3P-QCL design (V843)

To engineer the wavefunctions of the first iteration of THz 3P-QCL, we fixed the design parameters such as the alignment electric field, the material system, the doping concentration, and the injector barrier and tuned the thicknesses of all other quantum wells and barriers were free to change. In the first 3P-QCL design (The wafer name is V843 and we name this design after the wafer) a figure of merit proportional to the gain per number of carriers in a module was optimized. This figure of merit is defined as the product of population inversion, oscillator strength, and the inverse of the superperiod length. An injector barrier of 44 Å and a three-dimensional doping concentration of $9 \times 10^{15} \text{ cm}^{-3}$ were chosen for this device.[60] The optimization process was performed at a lattice temperature of 150 K. The electron temperature was assumed to be 50 K higher than that of the lattice temperature and it was fixed for all subbands with Boltzmann carrier distribution. For simplicity, only the LO-phonon scattering was included in the device optimization GA process. The electron-LO-phonon, electron-impurity and interface roughness (IR) inter-subband scatterings are considered in all simulation results of the V843 structure.

The quantum wells and barriers from the GA optimization converged to (starting with the injector barrier): **44**/62.5/**10.9**/66.5/**22.8**/84.6/**9.1**/61 Å, where the bold font indicates the barriers. Fixing the 3D doping of the structure and obtaining the quantum wells and barriers widths determine the period of one cascade module and the two-dimensional dop-

ing concentration. The injection barrier was delta-doped with Si to $n_s = 3.25 \times 10^{10} \text{ cm}^{-2}$ at the center. The energy spacings of the first four energy states included in our rate equation model are 27.7, 14.3, and 34 meV at 21 kV/cm, respectively (see Figure 4.1). The energy spacing of 27.7 meV between state 1 (lower lasing state), and the extractor state, e , is 9 meV smaller than the LO-phonon energy of GaAs material. This can be attributed to that the optimization process was performed at electron temperature of 200 K at which the electron can be thermally activated to higher energy states to facilitate LO-phonon scattering assisted relaxation. The tunnel coupling strength of this structure is 1.14 meV which is not as high as the first demonstrated THz IDP-QCL ($\hbar\Omega = 1.5 \text{ meV}$). [46] The conduction band diagram and the moduli wavefunctions of V843 at 21 kV/cm are shown in Fig. 4.1. The excellent wavefunction overlap between i -2 and 1 - e results in a short scattering time from level i to the ULS (fast injection) and from LLS to level e . Using a radiative barrier of 22.8 Å makes the ULS and LLS fairly diagonal. The oscillator strength of V843 at alignment electric field is 0.39. The thick radiative barrier also limits the free carrier absorption from level i to higher states (for example level 5). The oscillator strength study, which was nicely performed in RP-QCLs,[57] can be employed for this new scheme and the effect of radiative barrier can be investigated. Energy spacing between the ULS and the extraction state is 42 meV which is only 5 meV higher than the phonon energy. Even though the overlap of those wavefunctions is not high, the non-radiative transition between the ULS and state e can adversely affect the performance of this structure.

4.2.1 Numerical simulation of V843

To investigate the effectiveness of our wavefunction engineering, the scattering times between the six states in one module, included in our RE model, and the tunneling rate between two modules, should be calculated. The calculated parameters included the scattering times among the first six states in one module, the population of each state, the current density, and the gain-bandwidth product based on the rate equation model at each electric field, starting from 0.5 kV/cm to 23 kV/cm at different operating temperatures. Figure 4.2 shows the simulation results at two electron temperatures: 70 K (lattice temperature = 20 K) and 200 K (lattice temperature = 150 K) versus electric field.

The most relevant time constants are shown in Fig. 4.2(a) for $T_e=70 \text{ K}$ and $T_e=200 \text{ K}$, where τ_i is the lifetime of the injection state and τ_{tun} is the tunneling time between level e and i . $\tilde{\tau}_{2\text{eff}}$ is the *modified* effective lifetime which is defined in equation (3.6). The variables $\tau_{\text{tr}}^<$, and $\tau_{\text{tr}}^>$ are transit time—excluding the tunneling time—through the four quantum wells, *without* stimulated emission, and transit time—excluding the tunneling time—through the four quantum wells, *with* stimulated emission. The definition of all

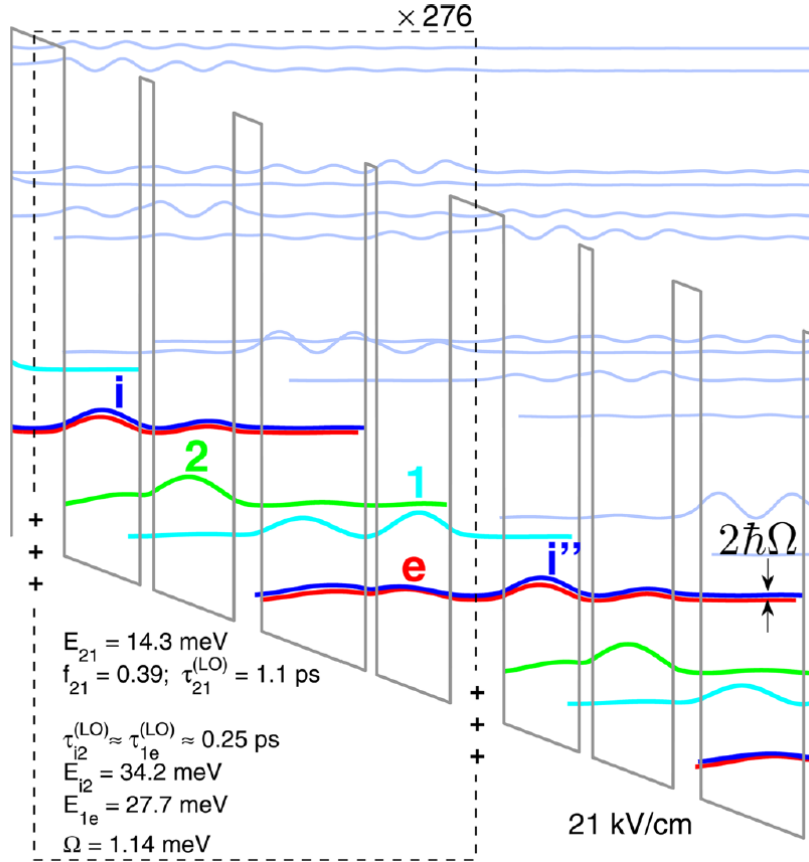


Figure 4.1: Conduction band diagram and the moduli squared of wavefunctions of the THz 3P-QCL, V843, at 21 kV/cm. The “+” signs denote the position of Si doping in each module. The intersubband lifetimes by LO-phonon emission are given at the resonant in-plane kinetic energy.[60]

aforementioned scattering times was discussed in section 3.2. As shown in Fig. 4.2(a), the tunneling time is fairly longer than the injection life time, τ_i , at designed electric field. This results in an accumulation of the carrier in extraction state, e , and increases the backfilling to the LLS and limits the population inversion. Since the transition time before threshold, $\tau_{tr}^<$ is not very different from the transition time after threshold, $\tau_{tr}^>$, due to a not highly diagonal design between the lasing states, the difference between the current density before and after threshold may not be very high.

Figure 4.2(b) shows the carrier density of each state at different electric fields. As expected, the carrier density at level e , n_e , is dominant almost over the entire bias range. This shows that most of the carriers are piled up at level e , even near the designed electric field of 21 kV/cm. Even though using a relatively thick injector barrier in this design accumulates carriers in level e , it can be shown that the population of the ULS, level 2, is higher than that of level e at low temperature which does not happen in RP-QCL designs. The population inversion of the design, shown in solid circles, decreases with temperature. The reduction of population inversion can be either from increasing the electron density of level 1 due to backfilling from level e , or from decreasing the electron density of the ULS due to faster non-radiative transition time (mostly the LO phonon scattering rate) of the ULS. The gain-bandwidth product, current density, and lasing frequency are shown in Fig. 4.2(c). The value of the gain-bandwidth product changes modestly, from 20 K to 150 K. The optical gain increases with the electric field at a slower pace than the population inversion; this is due to the electric field dependence of the oscillator strength, for instance, between 19 and 21 kV/cm, it reduces from 0.47 to 0.39. The slight decrease in current density at higher temperature is related to backfilling to the LLS, meaning that fewer carriers get involved in the transport. The lasing frequency of the design which can be estimated by energy spacing between the lasing state, changes from 2.9 THz to 3.4 THz when the electric field increases from 19 to 21 kV/cm. We will discuss the experimental results in the next section.

4.2.2 Experimental results

The whole QCL structure V843 consists of 267 repeats of the module presented in Fig. 4.1 and was grown on a semi-insulating GaAs substrate using molecular beam epitaxy with a total thickness of 10 μm . The active region is sandwiched between a 100 nm of $3 \times 10^{18} \text{ cm}^{-3}$ bottom n^+ GaAs and a top stack of 20 nm of $8 \times 10^{17} \text{ cm}^{-3}$, 50 nm of $5 \times 10^{18} \text{ cm}^{-3}$, 10 nm of $5 \times 10^{19} \text{ cm}^{-3} n^+$ and 3 nm of low-temperature (LT) grown GaAs. The first layer of the top stack is meant to adjust the Fermi level so as to align with the injector state of

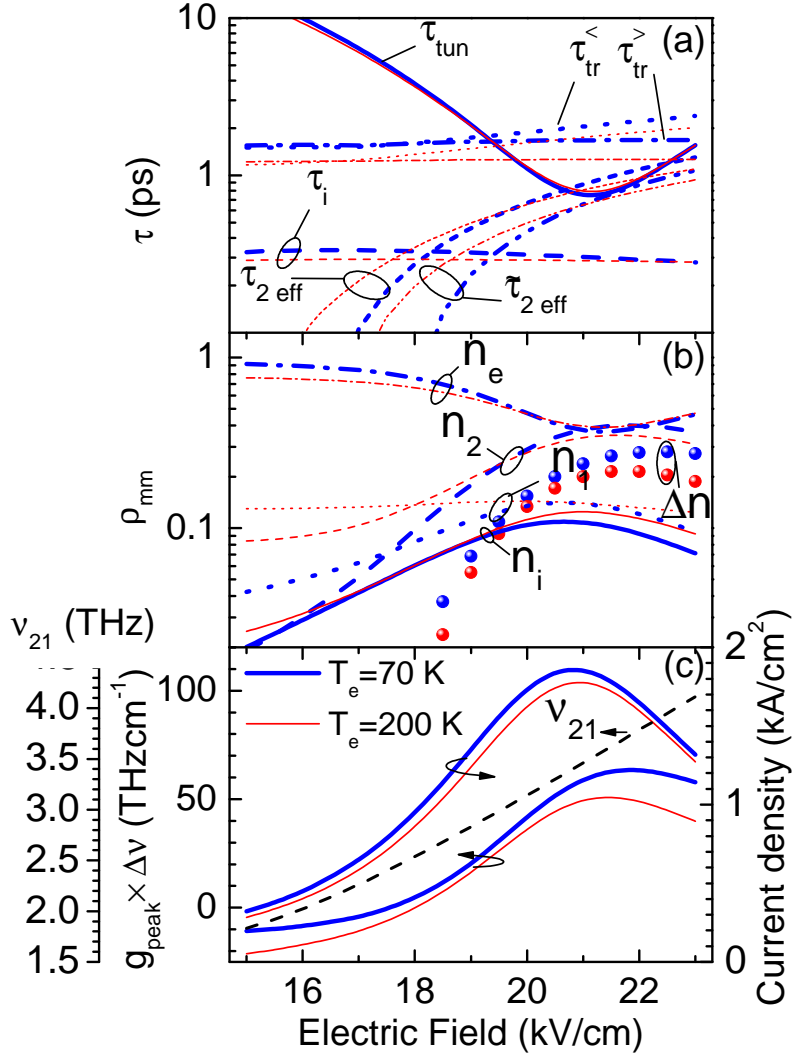


Figure 4.2: The 4-level RE simulation results of V843. (a) Different characteristic times at 20 K ($T_e = 70$ K, thick blue lines) and 150 K ($T_e = 200$ K, thin red lines). The scattering time presented in figure are defined as follows: τ_{tun} is tunneling time (solid line), $\tau_{\text{tr}}^<$ (dot line) and $\tau_{\text{tr}}^>$ (dash dot line) are the transit times—excluding the tunneling time—across the four wells before and after threshold, respectively; τ_i is injection state lifetime (dash line); and $\tilde{\tau}_{2\text{eff}}$ is the *modified* effective lifetime (dash dot dot line). (b) Normalized populations of the four states at 20 K (thick blue lines) and 150 K (thin red lines) lattice temperatures and the population inversion ($n_2 - n_1$) at 20 K (blue solid circles) and 150 K (red solid circles), (c) Current density, lasing frequency (dashed line), and optical gain-bandwidth product vs electric field at 20 and 150 K lattice temperatures.

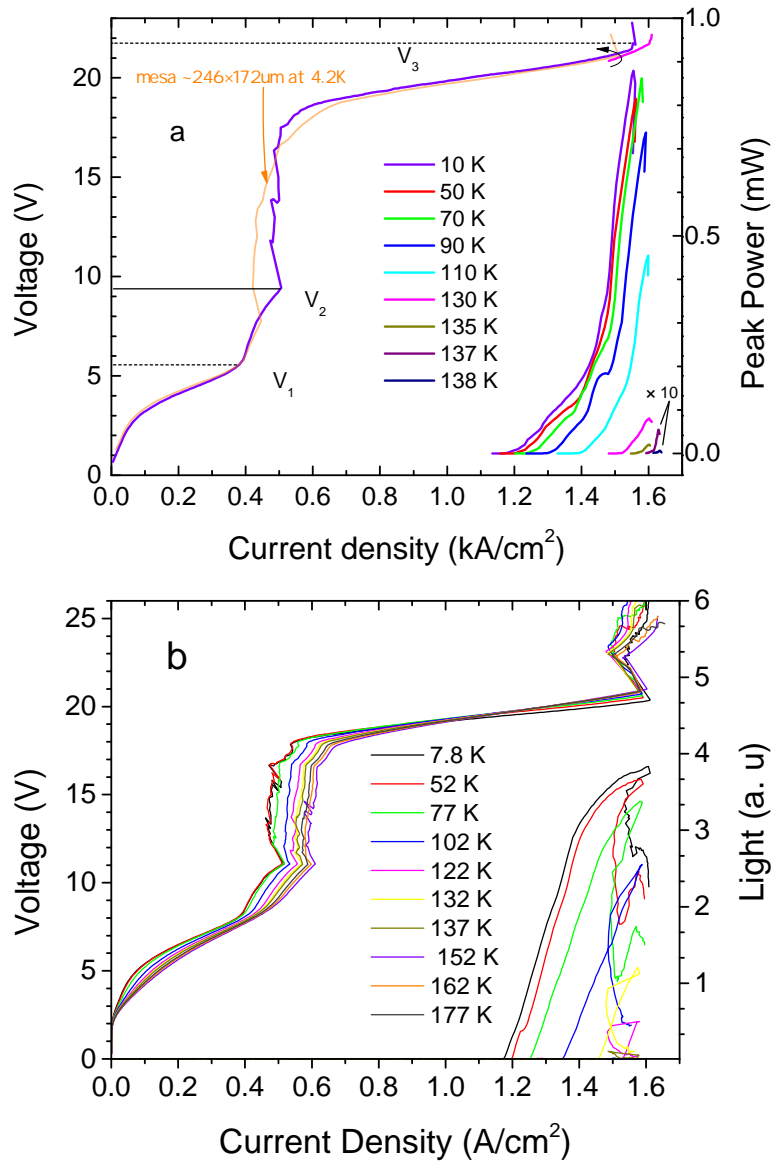


Figure 4.3: Left axis: The bias voltage of THz 3P-QCL V843 versus the current density, a) Device A b) Device B. Right axis: Collected THz light (optical output power) versus current density at different heat sink temperatures. Since the measurement set-up and the waveguide properties are different, the collected light, and the maximum current density, are different in plots a) and b). Drop voltage on device B is higher than on device A, the latter having the top 100 nm n^+ contact GaAs layer hence, a top Schottky contact with a short depleted region (~ 18 nm).

the first module, and the last two layers are used to form a non-alloyed ohmic contact. Two different fabrication processes were employed to compare the effect of waveguide loss on device performance of this structure. Since the oscillator strength of this 3P structure is not so low, the maximum operating temperature may not be enhanced substantially by reducing the waveguide loss. [92, 57] The first fabrication process, device A, used a Au-Au ridge waveguide with a 144 μm width and ~ 1 mm length while the second fabrication process, device B, has a wider (159 μm) and longer (1.79 mm) waveguide. The 100 nm thick top contact layer was removed in device B to lower the waveguide loss. The Ti/Au metalization process and In-Au bonding technique were employed for device A, while device B was fabricated using a Ta/Au metallization process and a Au-Au bonding process. The laser bars were indium soldered (epi-layer side up) on silicon carriers and then mounted in a He closed-cycle cryostat for measurements (See section 2.3.1).

Figure 4.3(a) shows the pulsed light-current density-voltage (L-J-V) characteristics of device A from 10 K to 138 K, with a pulse duration of 250 ns and repetition rate of 1 kHz. The threshold current density of 1.17 (1.17) kA/cm^2 was measured for device A (device B) package, while the maximum current density was 1.55 (1.61) kA/cm^2 . The higher maximum current density which enhances the dynamic range of device B and improves the maximum operating temperature may be attributed to a faster stimulated emission rate in device B due to its lower cavity loss. The maximum operating temperatures of 138.5 K and 141 K were achieved with devices A and B, respectively. The maximum collected optical power in devices A and B was 0.9 mW and 3.8 mW at lattice temperatures of 10 K and 7.8 K, respectively (The optical set up and the injected electric power were different in device A and B).

The device starts lasing at 20.2 V and stop at 21.8 V. The current density-voltage plot of the device at 10 K shows a small shoulder at 5.6 V, the first NDR at 9.5 V, and the final NDR at 21.8 V. By subtracting the Schottky voltage drop on the top contact (0.8V), [60] the shoulder point voltage (V_1), the first NDR (V_2), and the final NDR voltage (V_3) corresponds to electric fields of 4.8 kV/cm, 8.7 kV/cm, and 21 kV/cm, respectively. The Schottky drop voltage (0.8 V) of top contact was obtained by comparing the V-J measurements of the lasing and non-lasing devices. The width and length of the non-lasing device were reduced to 248 μm and 174 μm , respectively to increase the loss of the cavity, and hence to suppress the stimulated radiation. In addition, the non-lasing device was annealed to form PdGeTiPtAu ohmic contacts, which had the advantage—for this particular application—to increase the waveguide loss. [79] Besides, these ohmic contacts reduce the potential drop across the metal/semiconductor interfaces and help to achieve accurate V-J curve measurements. [109, 60] To investigate the origin of the small shoulder and the first

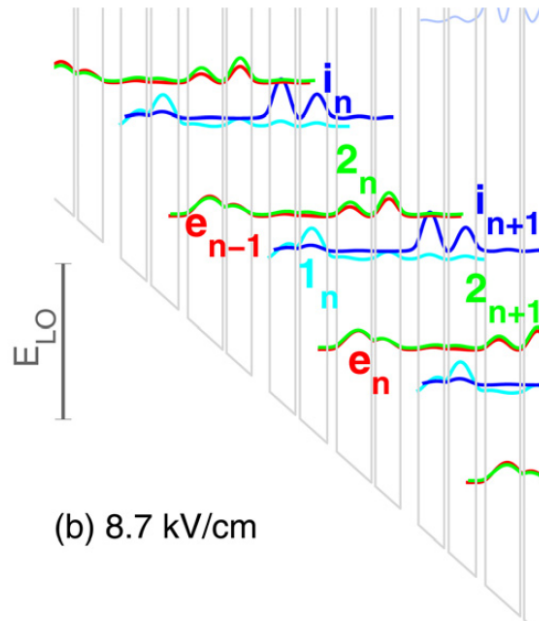
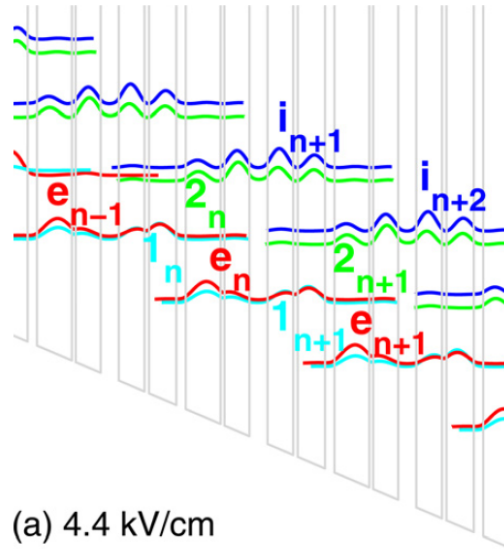


Figure 4.4: Conduction band diagram and the moduli squared of wavefunctions of V843 at a) 4.4 kV/cm and b) 8.7 kV/cm. States in left module (upstream), middle module, and right module (downstream) are represented by subscripts $n - 1$, n , and $n + 1$, respectively. The extraction state (e) of each module is in resonance with states 1 and 2 of next module at electric fields of 4.4 kV/cm and 8.7 kV/cm, respectively.

NDR feature, the wavefunction of the design at electric field of 4.4 kV/cm was calculated and plotted in Fig. 4.4 (a) when level e_{n-1} and I_n are aligned with a coupling strength of $\Omega = 0.385$ meV. Interestingly, at the same electric field, levels 2_{n+1} and i_{n+2} anticross and are also aligned with I_n and e_{n-1} . These four states could form a weakly coupled miniband (see Figure 4.4(a)). One could imagine transport occurring across two periods directly from e_{n-1} to 2_{n+1} . Therefore, one can propose that the shoulder in V-J plot at ~ 5.6 V, which is also slightly higher than e -1 alignment voltage ($4.4+0.8=5.2$ V), corresponds to an electric field at which $2qL\mathcal{E} \approx E_{LO}$ (4.8 kV/cm when taking into account the Schottky voltage drop). At 8.7 kV/cm, when $qL\mathcal{E} = 32$ meV $\approx E_{LO}$, levels e_{n-1} and 2_n are aligned with a small coupling strength $\Omega_{e2} = 0.24$ meV. Transition to the next lower extraction state e_n should be efficient, leading to the first NDR. This low coupling strength shows that this transport channel is incoherent, and hence very dependent on phase coherence time constant[60].

The light measurements of both device A and B show that the maximum amount of the optical power was collected at a current density right before the final NDR. The roll-over of output optical power in current ranges below maximum currents, observed in [65], is not observed in devices V843 A and V843 B. The origin of the roll-over in IDP structures was explained in chapter 1. Since, on the one hand, the coupling injection strength of V843 is lower than that of the one presented in [65] (1.14 meV compared to 2 meV), and on the other hand, the excess energy (voltage drop per module minus $2E_{LO}$) of V843 is low (2.6 meV at designed electric field that could compensate for the small extraction energy E_{1e}), our device does not suffer from the roll-over effect that can degrade the performance of THz IDP-QCLs.

The spectral measurements of this structure at different current injections and different temperatures are illustrated in Fig. 4.5. At 10 K, the lasing frequency started from ~ 2.83 THz at near threshold voltage and blue-shifted to ~ 3.23 THz at 21.7 V considering the highest amplitude longitudinal mode. At a current injection of 1.56 kA/cm², corresponding to 21.8 V, the device exhibits multiple Fabry-Perot modes ranging from 2.83 THz to 3.23 THz at 10 K. The simulations (the dash line in Fig. 4.2(c)) predict that the lasing frequency is 3.05 THz at 19.7 kV/cm (an actual device bias of 20.5 V); experimentally, 2.83 THz was observed. At 21 kV/cm the lasing frequency is 3.46 THz (simulation) vs. 3.23 THz (experiment). At 141 K and near the J_{max} , the spectral measurement shows a single lasing frequency of ~ 2.87 THz.

We simulated the V843 design, and fabricated and characterized laser devices. V843 introduces a new design scheme of the active region of THz QCLs, which is totally different from other three main-stream designs. Nevertheless, this first generation based on IDP QCL suffers from a low optical power, low current dynamic range, high intermediate resonant current, small $k_B T / \hbar \omega$ parameter, and no discontinuity in differential resistance at

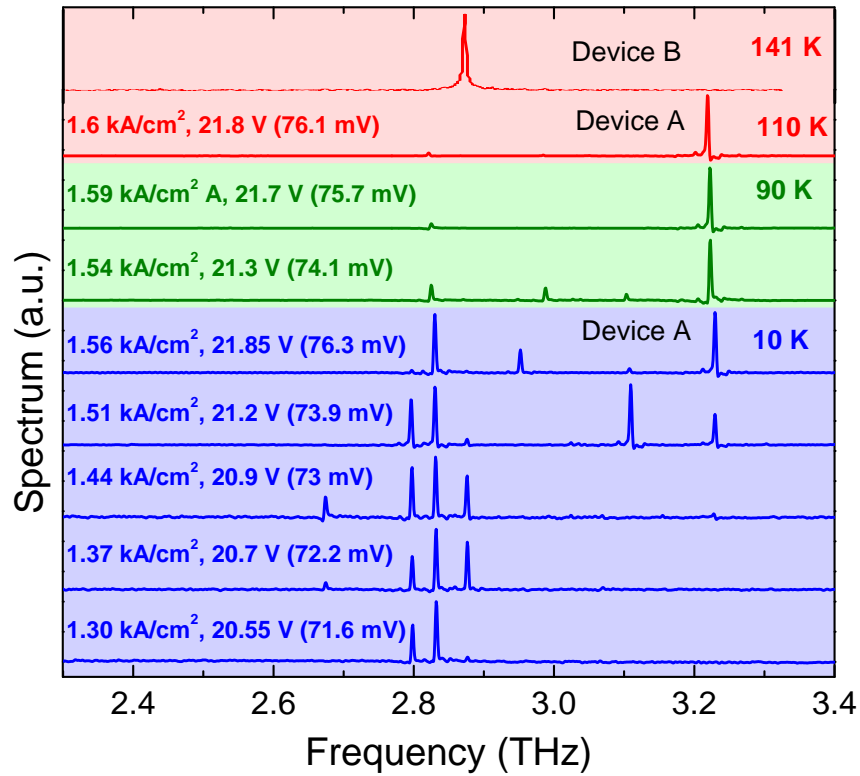


Figure 4.5: THz spectra recorded for different biases and temperatures. The current density, the applied voltage bias, and voltage drop per module are reported in the figure. Spectrum at 141 K was collected from device B while all other spectra were measured from device A.

threshold. The maximum operating temperature of this new scheme (138.5 K) is not far from the first generation of three-well THz RP-QCL (142 K) [49] which is recently (after 5 years of its first generation) lased up to ~ 200 K [56]. To improve the performance of our device in terms of output power, dynamic range, and intermediate resonant current, we propose a new 3P design based on a new optimization figure of merit. The results of the second generation of THz 3P-QCL will be presented in the next section.

4.3 Second 3P-QCL design (V845)

In the second generation of 3P-QCL design, we targeted to maximize the ratio of the gain versus injection current at a lattice temperature of 150 K. The figure of merit used during the GA optimization of this work was defined as a product of (gain - cavity loss), average transit time per period, and inverse of the superperiod length at 150 K. The cavity loss was set at 23 cm^{-1} , which might be slightly underestimated. The gain was calculated by using a 4-level rate equation model and by assuming $\Delta\nu = 1 \text{ THz}$ for the full width at half maximum. Even though during the GA design optimization the gain was estimated for a 3D doping of $7 \times 10^{15} \text{ cm}^{-3}$, at the last minute, before the MBE growth, it was finally increased to $9 \times 10^{15} \text{ cm}^{-3}$. The three-dimensional doping concentration, the injector barrier, the desired electric field, and the material (GaAs/Al_{0.25}Ga_{0.75}As) were fixed (same as V843) while the quantum well and barrier widths were free to change. The scattering mechanisms, included in this design, are the same as what were included in V843. Both forward and backward scattering channels were computed in our simulation. The converged quantum well and barrier widths from the GA optimization process are (starting with the injector barrier): **44**/64.5/**16.2**/71.5/**27.9**/104.45/**6**/49.65 Å, where the bold font indicates the barriers. Fixing the 3D doping of the structure and obtaining the quantum wells and barriers widths determine the superlattice length and the two-dimensional doping concentration. The first well after the injection barrier was delta-doped with Si to $n_s = 3.45 \times 10^{10} \text{ cm}^{-2}$ near the center. This structure was grown by using MBE with a wafer number V845.

The energy spacings of the first four energy states contributing to carrier transport are 36.6, 13.9, and 30.3 meV at 21 kV/cm, respectively. The oscillator strength ($f = 0.276$) and the injection coupling strength ($\hbar\Omega = 0.85 \text{ meV}$ at 21 kV/cm) of this structure are lower than those of V843, respectively. Such a low injection coupling indicates incoherent tunnel through the injection barrier and thus limits the maximum lasing current of the device. This low value of tunnel coupling strength is resulted from the specifically defined figure of merit, whose target is to maximize the modal gain over the current ratio. Both

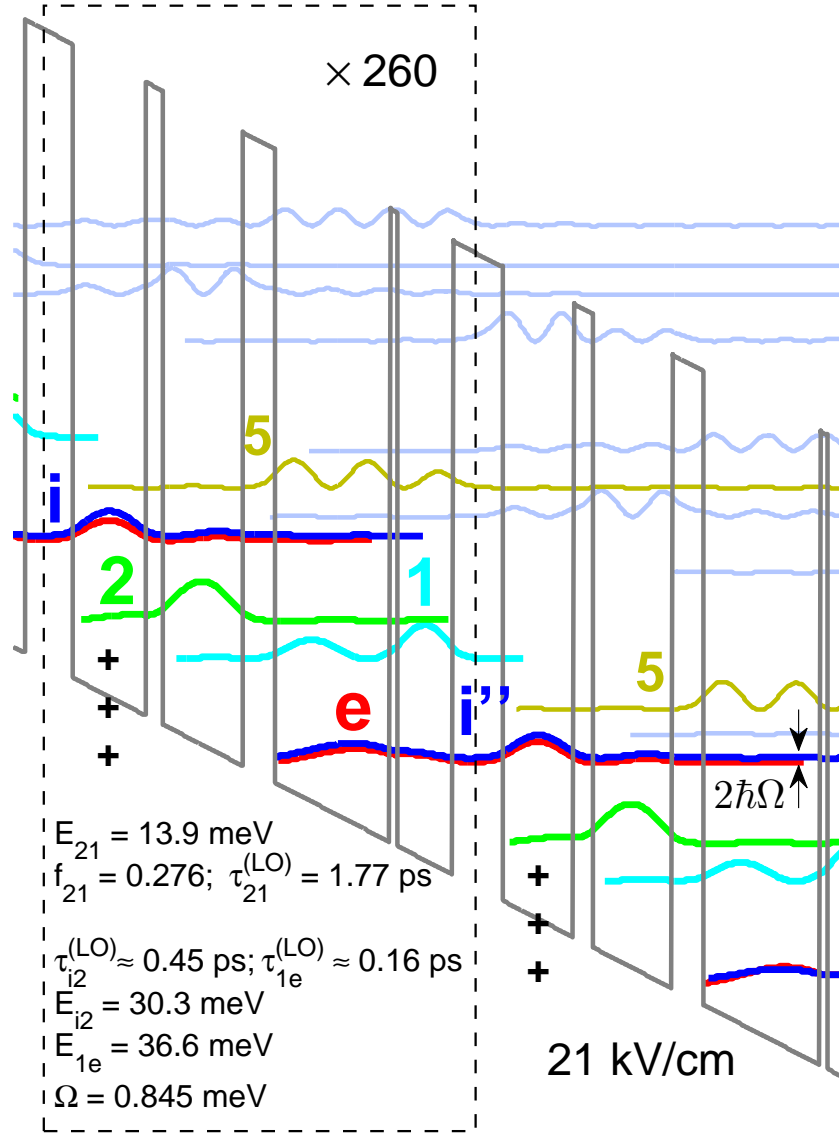


Figure 4.6: Conduction band diagram and the moduli squared of wavefunctions of the THz 3P-QCL, V845, at 21 kV/cm. The “+” signs denote the position of Si doping in each module. The intersubband lifetimes by LO-phonon emission are given at the resonant in-plane kinetic energy.

the threshold current and the maximum current of V845 are lower than those of V843, respectively. The energy spacing of 36.6 meV between levels l and e results in a much short relaxation time of 0.21 ps at 150 K compared to 0.41 ps in V843. A longer scattering time between the lasing states (2 and 1) can increase the population inversion at higher temperatures. This is achieved by spatially separating wavefunctions of the lasing states a bit more. The conduction band diagram and moduli wavefunctions of the corresponding energy states in two adjacent modules at 21 kV/cm are shown in Fig. 4.6. Since we have defined a specific figure of merit to find a structure with higher gain at lower current and also forced the algorithm to set the injector barrier thickness at 44 Å, the new design concerns (injecting carrier to the fifth and sixth states and tunneling before threshold), presented in section 4.1.1, may not affect our optimization process. If we decrease the thickness of the injector barrier and enhance the coupling strength between levels e and i (what we did in third generation of 3P-QCLs) to reach a high current dynamic range and operating temperature, the effect of the fifth and sixth energy states and tunneling before the threshold must be considered. The results of V845 RE model including the 4 levels, 5 levels, 6 levels were almost the same, suggesting the 5th and 6th states of this design has a marginal impact on transport.

4.3.1 Numerical simulation of V845

To investigate the design performance, the most relevant time constants, the same as what was discussed in V843, were calculated for V845 and presented in Fig. 4.7(a). Since the injector barrier is thick (44 Å), and due to the specifically defined figure of merit, the coupling between the wavefunctions of level e and i is small; the tunneling between these states is incoherent. This incoherency in transport could result in carrier accumulation at level e , increasing the backfilling, specially at higher temperatures. The faster scattering from the injector state i (τ_i), compared to the tunneling time τ_{tun} shown in Fig. 4.7(a), under various electric fields suggests the population on the extractor state will be significantly higher than that of the injector state. Both $\tau_{\text{tr}}^<$ and τ_{tun} are longer in V845 than in V843, which is due to a higher diagonality of the structure and a smaller coupling strength. Nevertheless, the population on the extractor state, n_e , remains almost the same for V845 and V843 as n_e is proportional to $\tau_{\text{tun}}/\tau_{\text{tr}}^<$. Since by design, the lifetime of the injection state, τ_i , is short, and the transit time without stimulated emission is rather long, there is no need to reach coherent transport through the injection barrier, i.e., $\tau_{\text{tun}} \ll \tau_i$. However, we would recommend to have τ_{tun} comparable to τ_i , i.e., $\tau_{\text{tun}} \gtrsim \tau_i$, to lower significantly the population on the extractor state, which can be achieved by increasing the tunnel coupling

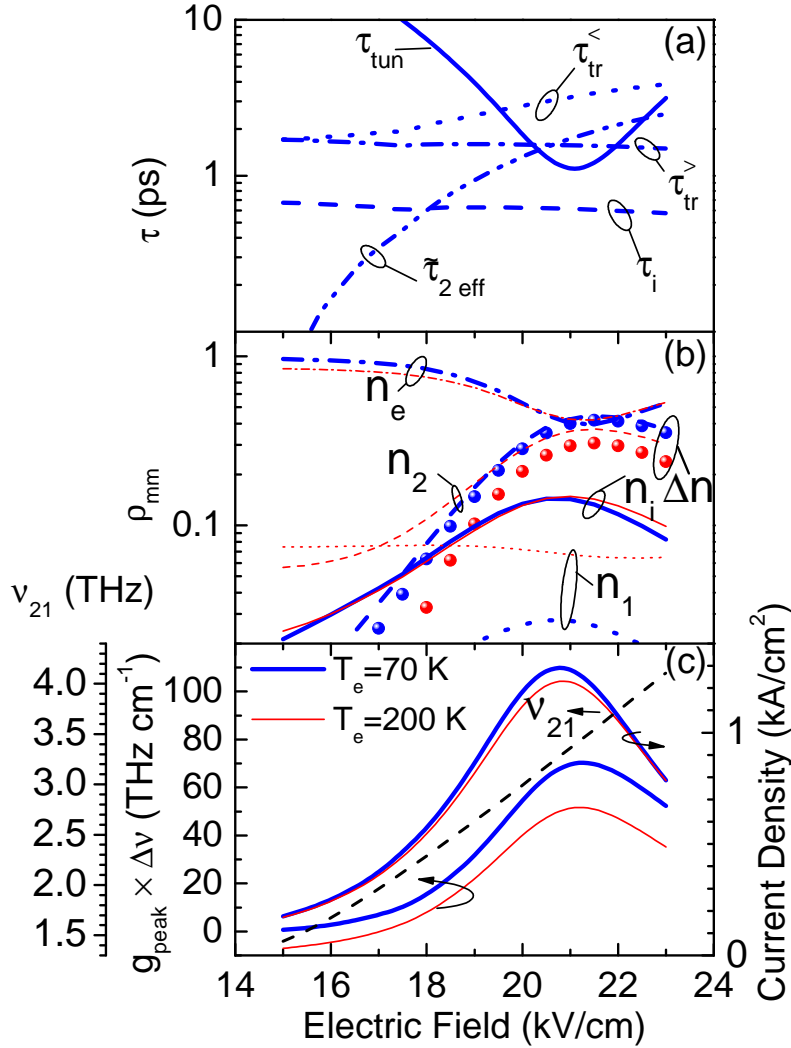


Figure 4.7: The 4-level RE simulation results of the structure presented in Fig. 4.6. (a) Different characteristic times at 20 K ($T_e = 70$ K, thick blue lines). The scattering time presented in figure are defined as follows: τ_{tun} is tunneling time (solid line), $\tau_{\text{tr}}^<$ (dot line) and $\tau_{\text{tr}}^>$ (dash dot line) are the transit times—excluding the tunneling time—across the four wells before and after threshold, respectively; τ_i is injection state lifetime (dash line); and $\tilde{\tau}_{2\text{eff}}$ is the *modified* effective lifetime (dash dot dot line). (b) Normalized populations of the four states at 20 K (thick blue lines) and 150 K (thin red lines) lattice temperatures and the population inversion ($n_2 - n_1$) at 20 K (blue solid circles) and 150 K (red solid circles), (c) Current density, lasing frequency (dashed line), and optical gain-bandwidth product vs electric field at 20 and 150 K lattice temperatures.

strength. At 21 kV/cm the energy spacing between states i and 2 (E_{i2}) in V845 is 6.4 meV below the GaAs phonon energy, as a result the injection of carriers on ULS is slowed down: $\tau_{i2} \sim 0.56$ ps vs 0.33 ps for V843 at 150 K. This increase in injector state lifetime explains why n_i is even worse (i.e. larger) in V845 as $n_i \sim \tau_i/\tau_{tr}^<$. The current at e - i alignment, calculated as the product of $n_e - n_i$ and the inverse of τ_{tun} will be lower than that of V843 due to lower $n_e - n_i$ and higher τ_{tun} simultaneously.

As shown in Figure 4.7(b), V845 also suffers from accumulation of carriers at level e . Consequently, due to the backfilling from level e , the density of carriers at level 1 (LLS) increases dramatically when the temperature increases from 20 K to 150 K. The population inversion (solid circles) decreases when the temperature increases from 20 K to 150 K but it is still higher than that of V843 [60] due to a longer *modified* effective lifetime $\tilde{\tau}_{2eff}$. At lower temperatures since the backward scattering is not fast, level 1 is almost empty. The gain-bandwidth product, current density, and lasing frequency are shown in Fig. 4.7(c). The value of the gain-bandwidth product changes modestly, from 20 K to 150 K. The maximum value of the gain-bandwidth product is 60.4 THz cm⁻¹ at 20 K, while it decreases to 48.1 THz cm⁻¹ and 43.1 THz cm⁻¹ at temperatures of 125 K and 150 K, respectively. The backfilling to the level 1 at higher temperatures, due to the piling-up at level e , is the main reason for the population inversion reduction and hence gain reduction. Even though the tunneling time τ_{tun} is exactly minimized at 21 kV/cm, i.e., at the electric field when e - i are perfectly aligned, the current density is peaked at ~ 20.7 kV/cm rather than at 21 kV/cm. This is because $(n_e - n_i)$ starts to decrease as the the electric field approached to 21 kV/cm. Figure 4.7(c) shows that the lasing frequency will vary from 2.8 THz near the threshold to 3.2 THz at the electric field near the NDR by assuming the product of the gain bandwidth ($\Delta\nu$) and the cavity loss (α_{cav}), to be $\Delta\nu \times \alpha_{cav} \sim 42$ THz cm⁻¹. [109]

4.4 Experimental results of V845

The whole QCL structure V845 consists of 260 repeats of the module presented in Fig. 4.6 and is grown on a semi-insulating GaAs substrate using molecular beam epitaxy with a total thickness of 10 μ m. The top and bottom contact layers of the V845 device are the same as V843 except the doping concentration of the first layer of the top stack, which is now 7×10^{17} cm⁻³ meant to adjust the Fermi level so as to align with the injector state of the first module.

We should point out that this V845 wafer was grown using a nearly depleted Ga cell.

Indeed the cell ran out of gallium during the flux measurement procedure conducted on the next day. Since the evaporation in such a situation is often taking place from several remaining droplets of gallium, the evaporation surface area can change in a random fashion. Thus, despite the MBE grower attempted to stabilize the flux by appropriate ramp of the cell temperature during the growth, the average Ga flux decreased by more than 2% during the active region growth process. The analysis of X-ray Diffraction (XRD) data of the grown wafer (V845) revealed step-like changes in the Ga flux, which resulted in three distinct sections of quantum cascade modules with different periodicities: the main section with 1.4% shorter period than the target value, and the other two sections with about 30 repeats each in which the periods were 0.4% shorter and 0.6% longer than the target value.

Two different fabrication processes (device A and device B), the same as what was presented in V843, were employed to compare the effect of waveguide loss on device performance of V845 structure. Since the oscillator strength of this 3P structure is lower than that of V843, the maximum operating temperature may be enhanced more substantially by lowering waveguide loss. [92, 57]

Figure 4.8(a) shows the pulsed light-current density-voltage (L-J-V) characteristics of device A from 10 K to 128.5 K, with the same pulse duration and frequency as V843 to ensure fair comparison. The threshold current density of 0.87 (0.8) kA/cm² was measured for device V845 A (device V845 B) package, while the maximum current density was 1.25 (1.34) kA/cm². The lower cavity loss results in a lower threshold current density (i.e., 0.8 kA/cm² at 7.8 K for device B vs. 0.87 kA/cm² for device A at 10 K) and a higher maximum current density which enhances the dynamic range of device B and improves the maximum operating temperature. The maximum operating temperature increases from 128.5 K (V845 A) to 152.5 K (V845 B) due to a lower waveguide loss. The maximum collected optical power in devices A and B was 1.5 mW and 5.8 mW at lattice temperature of 10 K and 7.8 K, respectively (The optical set up and the injected electric power were different in device A and B).

The solid orange V-J curve (device A) in Fig. 4.8(a) shows the first NDR at 8.5 V and the final NDR at 21.8 V. By deducting a 0.75 V Schottky drop voltage from the top contact [79] we will reach 21.05 V as the final NDR voltage of V845, which nicely matches with our designed electric field (21 kV/cm). The first NDR at 8.5V (7.75 kV/cm) comes from the resonance tunneling between levels e and 1 . The dashed-magenta curve in Fig. 4.8 (a), shows the V-J characteristic of a non-lasing V845, and the difference between the V-J curves of the lasing and non-lasing devices becomes distinguishable only after the threshold voltage indicated by a vertical arrow. The dashed-magenta curve was shifted upward along the voltage axis by a Schottky drop voltage of 0.75 V so as to overlap with the lasing V-J curve of the device A. At the final NDR voltage, the difference in current density between the lasing device and the non-lasing mesa is small, only ~ 60 A/cm². We also note that,

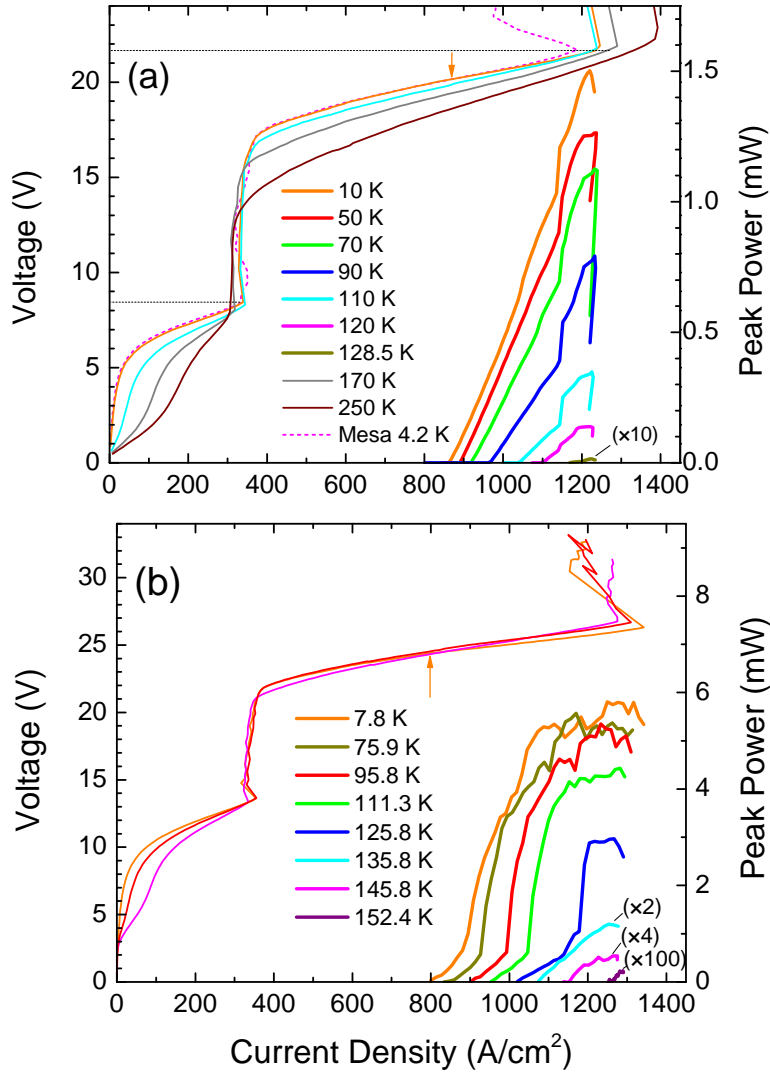


Figure 4.8: Left axis: The bias voltage of THz 3P-QCL V845 versus the current density, a) Device A b) Device B. The short vertical arrows show the change in the slope of the V-J curves at laser threshold and the lowest temperature (10 K for device A or 7.8 K for device B). Right axis: Collected THz light (optical output power) versus current density at different heat sink temperatures. Since the measurement set-up and the waveguide properties are different, the collected light, the maximum current density, and the threshold current are different in plots a) and b). Drop voltage on device B is higher than on device A, the latter having the top 100 nm n^+ contact GaAs layer.

above 130 K, a small resonance in the J-V characteristics develops slightly above 2 V. At low temperatures there are two important anticrossing resonances before the main resonance between states e and i . Since both simulated current peaks at electric fields of 7.7 and 10.5 kV/cm are far less than the threshold current, the two pre-threshold tunneling resonances ($e-1$ and $e-2$) impose a minimum impact on device lasing performance. This calculation should be performed for all structures based on the 3P scheme to ensure that the leakage currents at resonances of e to 1 and e to 2 are substantially lower than the threshold current, without sacrificing the dynamic range of the laser. To show how the quantum states couple and mix up when the leakage current density due to the $e-1$ tunneling resonance is peaked, the conduction band diagram and moduli wavefunctions of V845 is calculated and plotted in Fig. 4.9. The lowest energy state of the left module (e_{n-1}) is in resonance with the second energy state of the right module (1_n) at an electric field of 7.7 kV/cm, which is lower than the threshold electric field. The coupling strength between these states is $\hbar\Omega_{e1} = 0.235$ meV. Since the tunneling between level e and 1 is incoherent ($4\Omega_{e1}^2\tau_{||e1}\tau_1 = 0.35$ at 20 K), the dephasing time constant can affect the tunneling current. [96, 46] The carriers passing through the injector barrier (tunnel from e_{n-1} to 1_n) will quickly relax to the next extraction state (e_n). The second resonance should be observed at 10.5 kV/cm, where the states e and 2 are aligned. For this resonance, the transport is clearly incoherent, with a very low coupling strength between the states e to 2 ($\hbar\Omega_{e2} = 0.147$ meV) and a short relaxation time of level 2 ($\tau_{2e} = 0.25$ ps) that result in very low coherence in tunneling ($4\Omega_{e2}^2\tau_{||e2}\tau_{2e} \sim 6 \times 10^{-3}$ at 20 K). Therefore, the current through the $e-2$ channel is smaller than that of $e-1$ channel because of its smaller coupling strength and, to a lesser extent, due to its shorter dephasing time. We note that the relaxation times of levels 2 and 1 are inverted at these low electric fields, i.e. fast for level 2 (0.18 ps) and slow for level 1 (3.48 ps) as the two lasing states did not anticross yet (2 and 1 are aligned at 13.3 kV/cm). The observed small shoulder in the J-V curves around 2 V that slowly develops above 130 K (Fig. 4.8(a)) is related to tunneling between levels 2_{n-1} and i_n . At such high temperatures, level 1 is more populated and the channel $1 \rightarrow i$ (resonant at ~ 6.6 kV/cm) is more activated, which, when combined with the $e \rightarrow 1$ channel (resonant at 7.7 kV/cm), results in slightly shifted, slightly less intense and broader peaks of the J-V characteristics (lower conductance) before the first NDR. Such alterations of the electrical characteristics before the first NDR have been experimentally observed here at high temperatures

The same as what observed in V843, the light measurement of device A shows that the maximum amount of the light was collected at a current density near the NDR. The coupling injection strength in V845 (0.85 meV), and low excess energy (voltage drop per

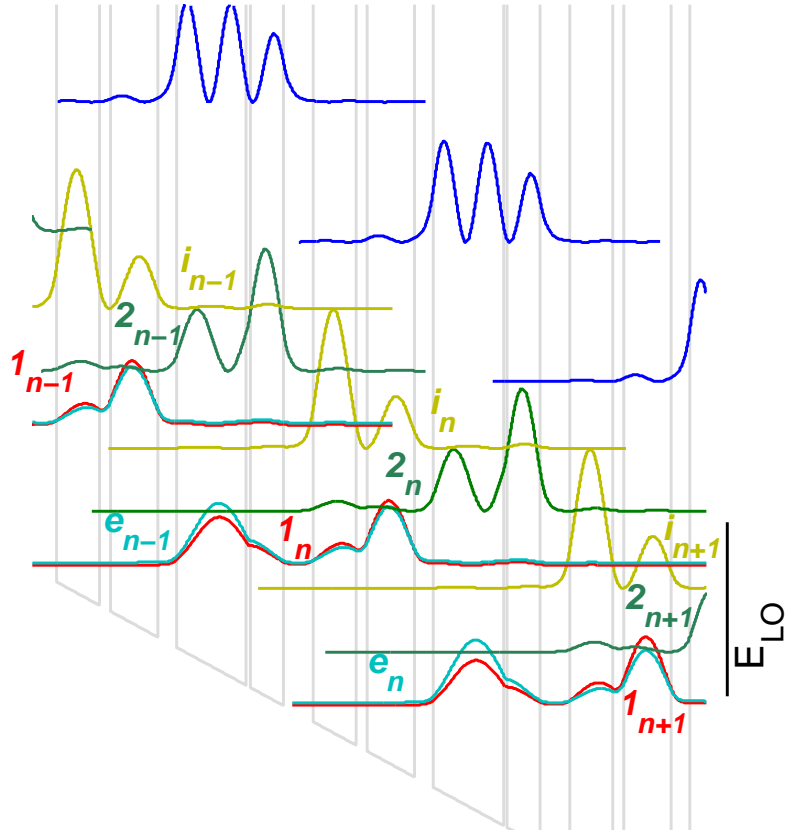


Figure 4.9: Conduction band diagram and the moduli squared of wavefunctions of V845 at 7.7 kV/cm. States in left module (upstream), middle module, and right module (downstream) are represented by subscripts $n - 1$, n , and $n + 1$, respectively. The extraction state (e) of each module is in resonance with state (I) of next module at an electric field of 7.7 kV/cm.

module minus $2E_{LO}$ is 7.3 meV at designed electric field in V845) are the main reasons that the roll-over in light measurement was not observed in V845 .

The spectral measurements of this structure at different current injections and different

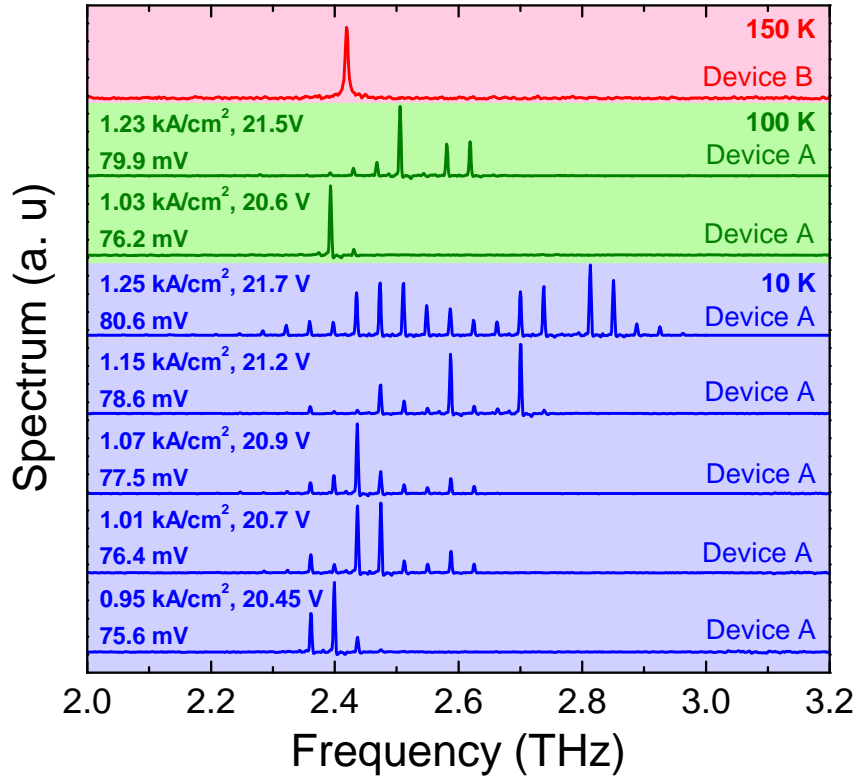


Figure 4.10: THz spectra recorded for different biases and temperatures. The current density, the applied voltage bias, and voltage drop per module are reported in the figure. Spectrum at 150 K was collected from device B while all other spectra were measured from device A.

temperatures are illustrated in Fig. 4.10. At 10 K, the lasing frequency started from ~ 2.4 THz at near threshold voltage and blue-shifted to ~ 2.8 THz at 21.7 V considering the highest amplitude longitudinal mode. At a current injection of 1.25 kA/cm^2 , corresponding to 21.7 V, the V845 device exhibits multiple Fabry-Perot modes ranging from 2.32 THz to 2.94 THz at 10 K. Even though our simulation predicted with fairly good accuracy the lasing frequency of the first generation of 3P-QCL, it cannot predict the spectrum of V845 accurately. For comparison, the simulations (the dash line in Fig.4.7(c)) predict that the lasing frequency is 2.9 THz at 19.7 kV/cm (an actual device bias of 20.45 V);

experimentally, 2.4 THz was observed. At 21 kV/cm the lasing frequency is 3.36 THz (simulation) vs. 2.32-2.94 THz (experiment). At 150 K and near the J_{\max} , the spectral measurement shows a single lasing frequency of ~ 2.4 THz, which seems to be the dominant frequency range (2.4-2.5 THz) over the lasing operating temperatures.

The theoretical study of laser frequency versus bias and temperature was not focused in this project. We will mention only three mechanisms that can change the peak gain frequency, and which were not taken into account in our RE model. Many-body interactions, in particular the depolarization (intersubband plasmon), can red-shift the optical resonance in an inverted two-level system.[110, 111] This depolarization effect could be weak though due to the small overlap between the lasing wavefunctions. If the population on LLS is substantial, for instance at high temperature by backfilling, the occurrence of Bloch gain cannot be excluded and it would tend to red-shift the peak position [112, 113]. Finally, our model does not solve self-consistently the Schrödinger, Poisson and rate equations. In reality, due to charge separation the electric field is not uniform within one module. Since the section between the expected positions of the ULS and LLS wavefunctions is more conductive when stimulated emission occurs, the electric field can be configured differently when device is lasing, thereby reducing the Stark effect on the lasing transition.[114].

Even though we could overcome some weak points of the first generation by defining a new figure of merit, the performance of the V845 is still far from the goal that we predict for 3P-QCL designs. We did not achieve a large discontinuity in differential resistance at threshold; therefore the collected optical power is not as high as RP-QCLs. The coupling injection is low which limits the maximum current density of the device. It seems the four-well 3P-QCL cannot simultaneously increase the maximum current density and the output power while keeping the intermediate resonant current low. In the next section, we introduce a new design based on five-well 3P-QCL, which may provide a solution to the dilemma and further improve the performance of the device.

4.5 Third 3P-QCL design (V962)

In first (V843) and second (V845) generations of THz 3P-QCLs, the injection coupling strength was sacrificed in order to suppress early negative differential resistance (NDR) prior to lasing threshold. In this section, we present a new 3P design with a high coupling-strength injection and a five-well quantum cascade module, focusing on achieving high output power and high lasing temperature operation. For this purpose, a narrow injector barrier is chosen to enhance lasing dynamic range. In addition, an extra well is included in the upper phonon stream to on the one hand reduce the intermediate resonance before the

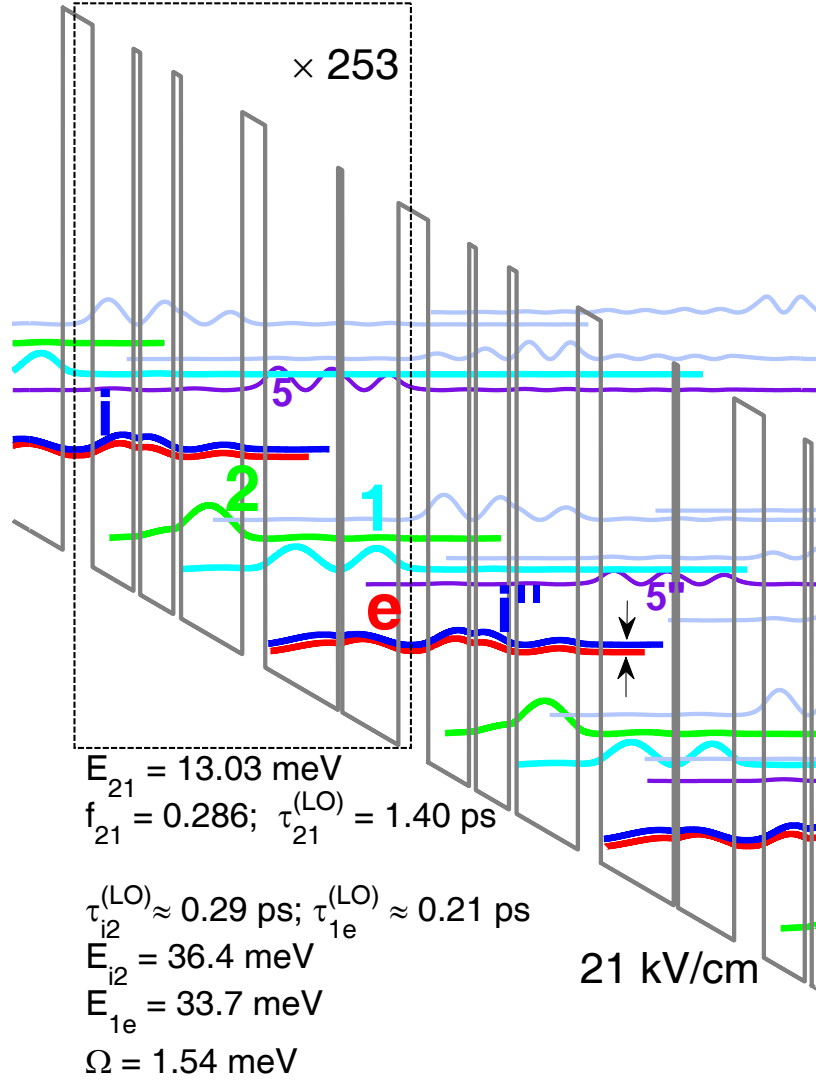


Figure 4.11: Conduction band diagram and the moduli squared of wavefunctions of a 3P THz QCL at 21 kV/cm. The quantum structure started with an injector barrier are **35/48/8/38.9/9/72/27/85.6/5/66** Å, where the bold font indicates the barrier. The center 20 Å of the 48 Å first well after the injector barrier is doped with Si to $1.5 \times 10^{17} \text{ cm}^{-3}$ to give a two-dimensional carrier concentration of $3 \times 10^{10} \text{ cm}^{-2}$ per module. The inter-subband lifetimes through LO phonon emission are given at the resonant in-plane kinetic energy.

threshold and, on the other hand minimize the rate of wrong injection to the lower lasing state (LLS) and thus increases device internal quantum efficiency.

Similar to what was presented in section 4.2 and in section 4.3, the first four states of the five-well 3P QCLs play the most important role in carrier transport and lasing operation. Nevertheless, the effect of the fifth and sixth energy states cannot be ignored because of the narrow injector barrier.[109] As a result, a simplified rate equation (RE) model that includes the first six states of each module was employed to predict the behavior of this laser.

The first two generations of 3P-QCLs (V843 and V845) were suffering from a thick injector barrier which impedes carrier injection from level e to i . Carriers were accumulated in level e and the device performance was deteriorated due to backfilling from level e to l . Simulation shows that the relative carrier population at level e is 37% in V843 and 42% in V845.

Figure 4.11 shows the conduction band and moduli wavefunctions of quantum states of the design. The inclusion of one extra well in upper phonon stream helps us to engineer the wavefunctions of levels i and l with more freedom. This results in a fast correct injection from level i to level l (0.33 ps at 10 K) and a slow wrong injection rate (4.65 ps in at 10 K) from level i to the level l . Since the energy spacing between level l and e is 46.7 meV (only 10 meV higher than the phonon energy in GaAs material (36.7 meV)), the wrong extraction ($l \rightarrow e$) rate has to be minimized by reducing the wavefunction overlap between those states. Using a relatively thicker radiative barrier could satisfy this requirement, while the oscillator strength is also lowered and the population inversion at high temperatures may thus be improved.

4.5.1 Numerical simulation of V962

To see the effect of a narrow injector barrier and adding one extra well in upper phonon wells, the most relevant scattering times were calculated and plotted in Fig. 4.12 (a). The tunneling time between level e and i of V962 is much faster than that of V845 and V843. In addition, as suggested in section 4.5.1, τ_i is as close as possible to the tunneling between level e and i . Figure 4.12(b) shows the carrier density of each state at different electric fields. Contrary to all RP-QCL designs and V843 and V845, level e is not the most populated state in V962 at $E > \sim 19$ kV/cm. This fast tunneling results in a low carrier population in level e near the designed electric field and reduces the backfilling to the LLS (l). The fast scattering time of level i helps carrier in that level to relax rapidly to the ULS. Since the oscillator strength of this V962 design is low (0.29), most of the electron

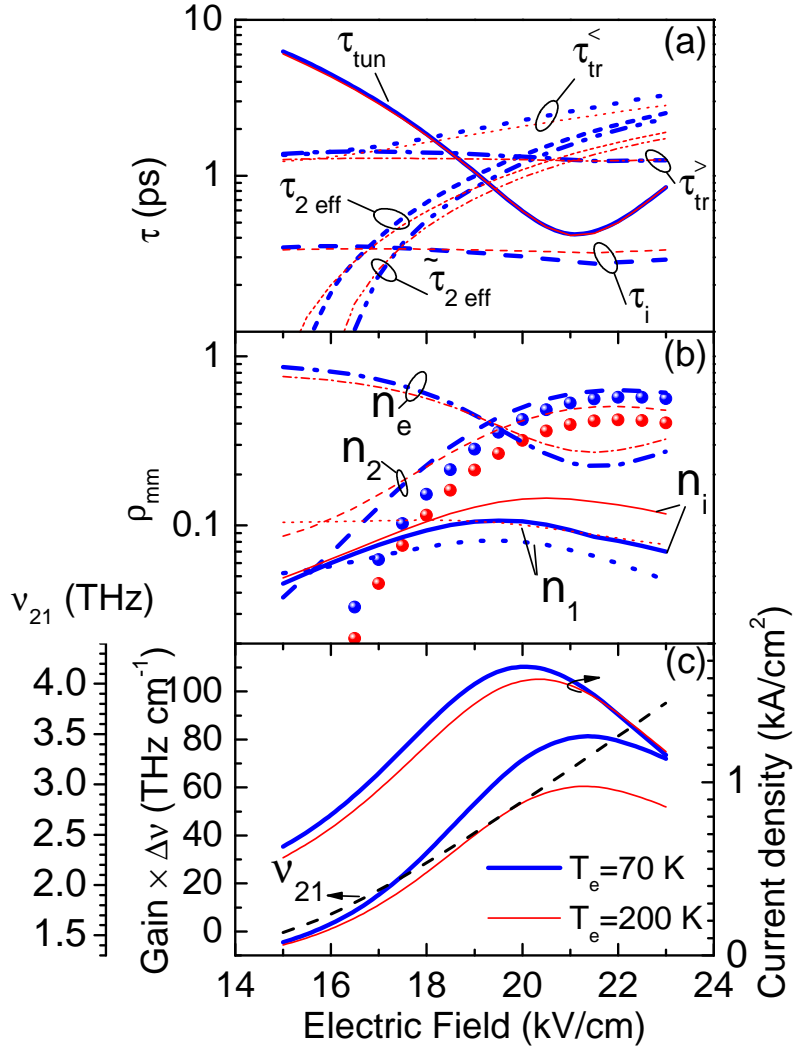


Figure 4.12: The 4-level RE simulation results of the structure presented in Fig. 4.11. (a) Different characteristic times at 20 K ($T_e = 70$ K, thick blue lines) and 150 K ($T_e = 200$ K, thin red lines). The scattering time presented in figure are defined as follows: τ_{tun} is tunneling time (solid line), $\tau_{\text{tr}}^<$ (dot line) and $\tau_{\text{tr}}^>$ (dash dot line) are the transit times—excluding the tunneling time—across the four wells before and after threshold, respectively; τ_i is injection state lifetime (dash line); and $\tilde{\tau}_{2\text{eff}}$ is the *modified* effective lifetime (dash dot dot line). (b) Normalized populations of the four states at 20 K (thick blue lines) and 150 K (thin red lines) lattice temperatures and the population inversion ($n_2 - n_1$) at 20 K (blue solid circles) and 150 K (red solid circles), (c) Current density of four-level system, lasing frequency (dashed line), and optical gain-bandwidth product vs electric field at 20 and 150 K lattice temperatures.

will stay in ULS at low temperature which means the population inversion of more than 50% is achievable. The population inversion of V962, plotted in solid circles reduces from 20 K to 150 K, but it is still higher than that of both V843 and V845. Even though the *modified* effective lifetime of V962 is not much different from that of V845, a higher population inversion is obtained in V962, which is attributed to the faster tunneling time (τ_{tun}) and transit time before threshold ($\tau_{\text{tr}}^<$) as revealed by equation (3.5).

The gain-bandwidth product, current density, and lasing frequency are shown in Fig. 4.12(c). The value of the gain-bandwidth product changes modestly, from 20 K to 150 K. The gain-bandwidth product of V962 is higher than those of V843 and V845 due to its higher population inversion. The current density, plotted in Fig. 4.12, is only the current density due to tunneling mechanism between level e and i . In all 3P-QCL designs, this is the major source of the total current density of the device. Fig. 4.12 shows that the maximum current density occurs at 19.5 kV/cm, 1.5 kV/cm lower than the alignment electric field of level e and level i which is 21 kV/cm. By including all the tunneling paths for first six states in one module, this electric field shifts to 21 kV/cm. The effect of leakage paths to level five and six of the next module can also be observed in our measurement JV curves, which show a shoulder before the final NDR. Figure 4.12 shows that the lasing frequency of the device will increase from 2.3 THz to 3.2 THz when the electric field rises from 18.5 kV/cm to 21 kV/cm. The change of the lasing frequency at low temperature from threshold voltage to NDR region is almost the same as what RE model predicts.

4.6 Experimental results of V962

The new five-well 3P structure is based on GaAs/Al_{0.25}Ga_{0.75}As material system, consists of 253 repeats of this module and is grown on a semi-insulating (SI) GaAs substrate by molecular beam epitaxy with a total thickness of 10 μm . Even though the fabrication process of V962 A is the same as device A of V843 and V845, the process of device B is different compared to equivalent V962 B of previous generation of 3P-QCLs. Instead of dry-etching process, the wet-etching was employed which is not in the same quality as dry-etching and the side wall of the device is not as sharp as previous devices. It may not be so fair to compare device V962 B to device V843 B and V845 B.

The fabrication process and the characterization set-up of device A are the same as what were used for both V843 and V845 to ensure fair comparison. Fig. 4.13 shows the pulsed light-current density-voltage (L-J-V) characteristics of fabricated QCL device with a Au-Au waveguide from 10 K to 144 K, with a pulse duration of 250 ns and repetition rate of 1 kHz. The threshold current density of 1.44 kA/cm² was measured at 10 K, while

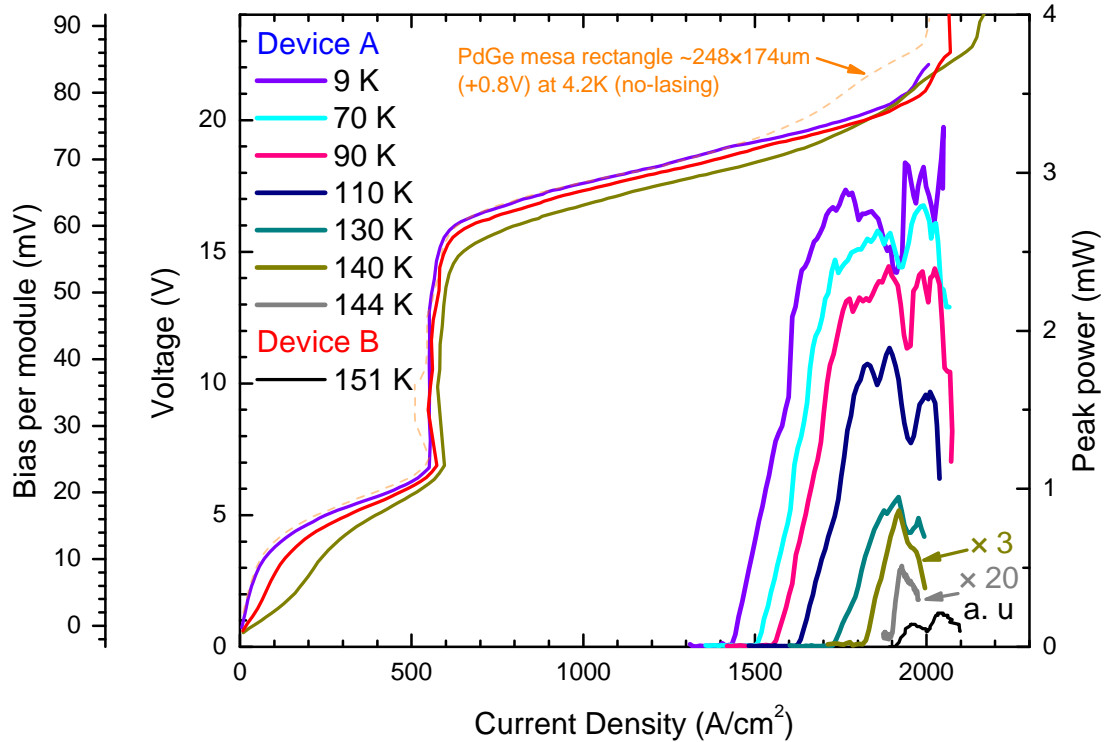


Figure 4.13: Left axis: The bias voltage of five-well THz 3P-QCL (V962) with a Au-Au waveguide versus the current density of the lasing (solid lines) at 4 K and non-lasing (dashed line) at 9 K, 90 K, and 140 K. The width and the length of the lasing device are $144 \mu\text{m}$ and $831 \mu\text{m}$, respectively. The short vertical arrows show the change in the slope of the V-J curves at laser threshold. Right axis: Collected THz light (optical output power) versus current density of device A (9 K to 144 K) and device B (151 K).

the maximum current density was 2.06 kA/cm^2 . A clear slope change in V-J curves at threshold can be observed from 10 K to 130 K due to improved quantum efficiency of this new design. The collected optical power is more than twice of what was collected in V845 with the same set-up and four times higher than that of V843. The maximum operating temperature was improved from 128.5 K in V845 and 138 K in V843 to 144 K in V962 with the same waveguide process. The first negative differential resistance (NDR) of both the non-lasing (orange dashed line) and the lasing device (purple line) is observed at 7.1 V, while the final NDR is at different biases (22.8 V for non-lasing and 22.0 V for lasing). Even though the maximum current density of the structure is as expected high due to narrow injector barrier, the intermediate tunneling current ($j_{\text{res}} = 575 \text{ A/cm}^2$) is not as low as what we initially expected. The inclusion of one extra well in upper phonon state is supposed to adequately suppress the intermediate tunneling current.

The first NDR of this device occurs at 7.1 V which corresponds to the electric field of 6.3 kV/cm ($7.1 - 0.8 \text{ V}$ Schottky drop voltage). The alignment between level e_{n-1} and l happens at 5.1 kV/cm with coupling strength of $\hbar\Omega = 0.32 \text{ meV}$. Since the injector barrier of this structure is small, there is a possibility of injecting carrier to a state of the non-neighbor module. Our calculation shows that level e_{n-1} will be in resonance with level i_{n+1} at 6.4 kV/cm which is roughly match with our measured resonance voltage. Figure 4.14 shows the conduction band diagram and moduli wavefunctions of V962 at electric field of 6.4 kV/cm . We did not expect this leakage current in our design. Generally the injector barrier is thick enough to separate each module from any other non-neighbor modules. Even though the leakage path increases the intermediate resonance current before threshold, it could not affect performance of the design since it is far below the threshold current. As will be shown in section 4.7, our simple rate equation model fails to predict the value of peak current density before threshold and the electric field at which this current occurs.

The spectral measurements of this structure at different current injections and different temperatures are illustrated in Fig. 4.15. The lasing frequency started from 2.42 THz at the threshold and blue-shifted to 3.3 THz at an electric field before NDR at 10 K. At the current injection of 2.02 kA/cm^2 (correspond to a bias of 22 V) and higher, the structure acts as a broad source that can lase from 2.42 THz to 3.92 THz (1.5 THz bandwidth) at 10 K. Our calculation shows that the lasing frequency changes from 2.3 THz at threshold to 3.2 THz at desired electric field of 21.2 kV/cm . Even though our model could predict the lasing frequency in most range of the operating electric fields, the high lasing frequency of 3.92 THz is far from of our simulation prediction. This high bandwidth lasing frequency could observe even at high temperature (up to 110 K), while at 130 K and higher, 2.67 THz is the main frequency of this structure. The origin of this 3.92 THz lasing frequency is not clear to us yet.

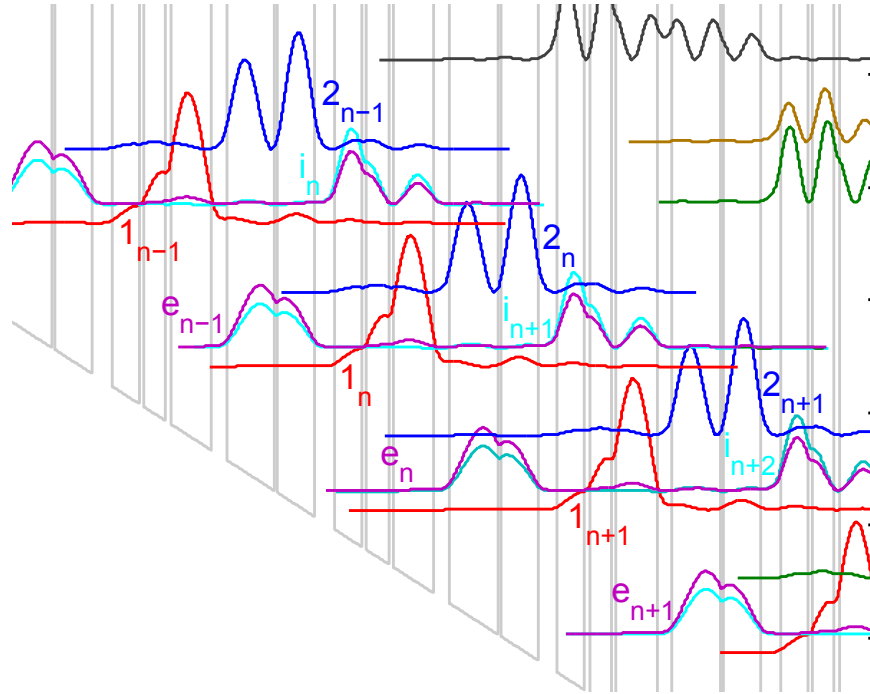


Figure 4.14: Conduction band diagram and the moduli squared of wavefunctions of 3P THz QCL at 6.4 kV/cm. States in left module (upstream), middle module, and right module (downstream) represent by $n-1$, n , and $n+1$, respectively. The extraction state (e_{n-1}) of each module is in resonance with state (1_{n+1}) of two-next module at electric field of 6.4 kV/cm.

The five-well 3P-QCL could improve the change in differential resistance, the output optical power, internal quantum efficiency, and the operating temperature, while the intermediate resonant current was not as low as what was expected. The detail comparison of those devices, presented in the next section, shows us the pros and cons of each 3P quantum design.

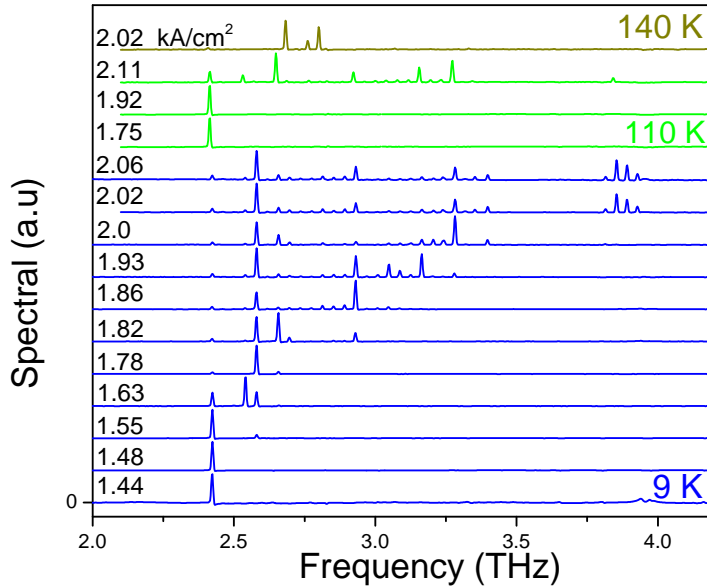


Figure 4.15: THz spectra recorded for different biases and temperatures. The spectrum at 10 K and a current density higher than 2 kA/cm² shows that this IDP structure works as a wideband source.

4.7 Analysis and Comparison of V843, V845, and V962

In this section of the thesis, we will analyze and compare three 3P-based designs, the details of their simulation and experimental results were presented in sections 4.2, 4.3, and 4.5. The RE model, presented in chapter 3, will be employed in this section to investigate the performance of all 3P-QCLs. The IV characteristic of each device, extracted from experimental results, will be compared to the current density calculation by our model. This comparison will help us to on the one hand understand the detail of each design

and the reason of unique behaviors of each structure, and on the other hand disclose the limitation of our model and inspire/enable us to make it more comprehensive and accurate. In addition, a few important experiment parameters, such as the discontinuity in differential resistance at threshold vs temperature will be plotted and compared. Finally, all specifications of 3P-QCLs will be tabulated to be easily compared.

4.7.1 Electrical characteristics

To investigate the performance of IDP-QCLs, the current density of all structures in a full range of electric fields at different temperatures were calculated and the simulation results of lasing and devices at 50 K are plotted in Fig. 4.16. For comparison, the experimental results are also plotted in a same figure for each device. The pure dephasing time, τ^* , was kept at a temperature-independent constant of 0.2 ps in our rate equation-based modeling so as to be consistent for all 3P-QCLs. We did not try to match for all temperatures the simulated J_{\max} with the experimental values. The threshold electric field of 19.2, 19.4, and 18.5 kV/cm was derived and matched the experimental value by assuming a gain bandwidth \times cavity loss product of ~ 40 THz cm^{-1} (38.5 - 41 THz cm^{-1}). Two pre-threshold current peaks are observable before the final NDR. In the experimental IV curves of V843, we could observed both peak currents while only one can be observed in V845 and V962. In V843, the tunneling current of the second peak is higher than the first tunneling current peak and it can be measured by our measurement setup. The second-order tunneling formalism with pure dephasing time of 0.2 ps could nicely predict not only the value of the first and second peak and the final NDR current density but also the electric fields at which those peak occur. In V845, the effect of tunneling of states e to 1 and e to 2 aligned at electric fields of 7.7 and 10.5 kV/cm, and giving rise to current peaks at ~ 7.7 and ~ 10.5 kV/cm, respectively. The measured peak leakage current at the first NDR, i.e., 7.7 kV/cm, is $J_{\text{res}} = 340$ A/cm², while the simulation result is 276 A/cm². however, the maximum current density of the lasing device can be reasonably well predicted by our simulation (at least at low temperature).

A vertical shift (64 A/cm²) was observed in the peak leakage current density at 7.7 kV/cm (340 A/cm² measured value vs. a 276 A/cm² simulation result). In V962, our model could not estimate the first NDR electric field accurately. Simulation results do not agree with experimental data in terms of the intermediate resonant current and voltage. Experimental results show that the first NDR of this device occurs at 7.1 V which corresponds to electric field of 6.3 kV/cm (7.1 - 0.8 V Schottky drop voltage). The measured current density of the device at that electric field is 575 A/cm². The alignment between level e_{n-1} and 1 happens at 5.1 kV/cm with coupling strength of $\hbar\Omega = 0.32$ meV. The

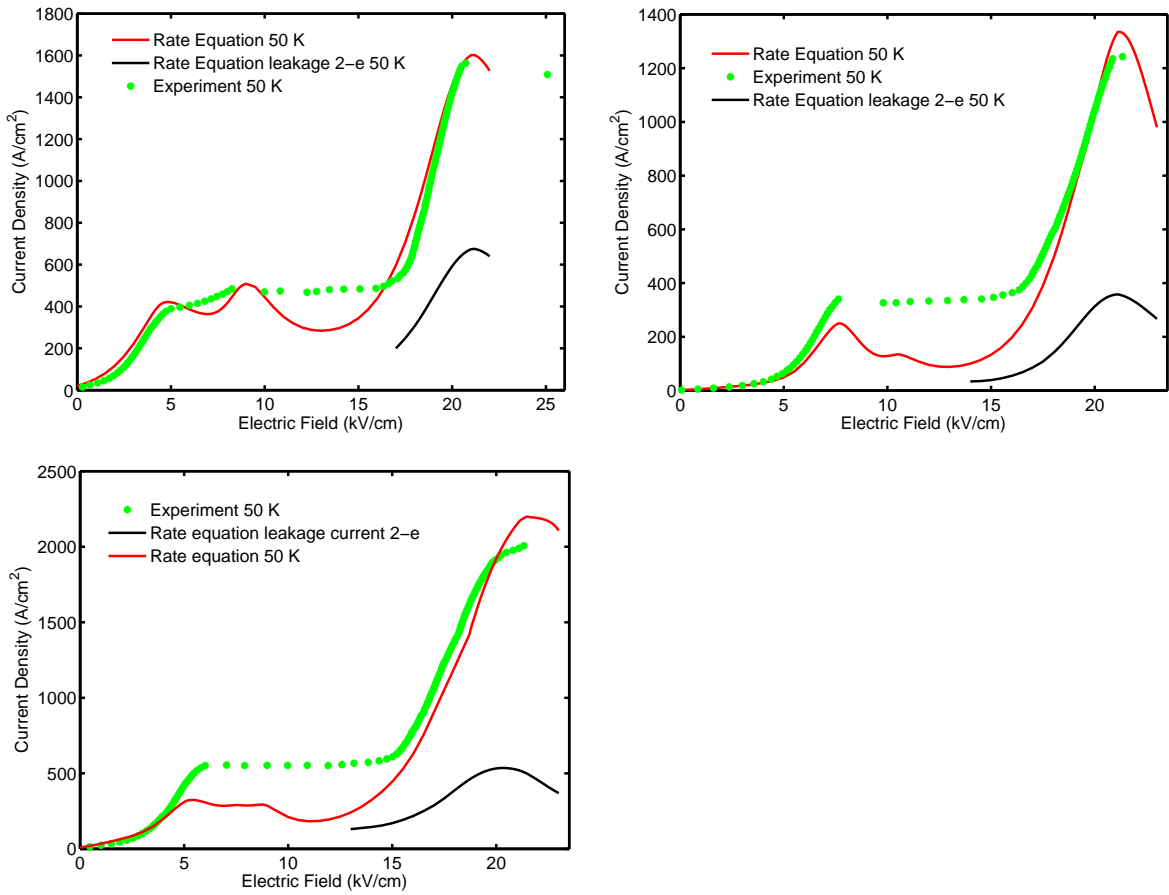


Figure 4.16: The current density vs the electric field of a) V843, b) V845, and c) V962. The red curve shows the simulation results based of RE formalism with second-order tunneling. The green dots show depict the experimental results of the lasing device. The black solid line represents the leakage currents from the wrong extraction $2-e$.

current density, calculated by rate equation, is 340 A/cm^2 , which is almost half of the measured current. Compared to the other 3P structures which show two intermediate resonances before threshold voltage (e_n to 1_{n+1} and e_n to 2_{n+1}), this structure suffers from an extra leakage path due to its very narrow injector barrier. As shown in Fig. 4.14, alignment between states e_{n-1} and i_{n+1} happens at an electric field (6.4 kV/cm) between alignment of states e_{n-1} and 1_n (5.1 kV/cm) and alignment of states e_{n-1} and 2_n (10.5 kV/cm). Even though there is an extra leakage path which increases the intermediate resonance current, the ratio of the maximum current over the intermediate peak current before threshold, J_{res} , is slightly better than V843 and almost the same high as V845 ($J_{\text{max}}/J_{\text{res}} = 3.7$ in V962 and V845 vs. 3.1 in V843). A small shoulder in JV of V962 at electric field of 19.5 kV/cm comes from two new leakage paths from ULS of module n to states 5 and 6 of module $n+1$ which were ignored in design stage.

The leakage current from the wrong extraction channel $2-e$, shown by a black lines in Fig. 4.16 (a), (b), and (c). After the first generation of 3P-QCL (V843), we keep in mind to reduce this leakage current in our design. As shown in Fig. 4.16, this leakage current in V845 is lower than that of V843, as is its fractional contribution to the total current. Lower spatial overlap, and higher energy spacing (50.5 meV in V845 compared to 42 meV in V843) between states 2 and e are the two main reasons for this lower leakage current and simply result from the specific wavefunction engineering where the net gain per electron injected was approximatively optimized through our GA approach. Two leakage currents from the wrong injection channels ($i-1$ and $i-e$) were small and can be ignored [109]. The same strategy was employed in V962 to keep the leakage path between states 2 and e low. Even though the absolute value of this leakage current in V962 is higher than that of V845, its fraction to the maximum current is lower than those of V843 and V845.

4.7.2 Differential resistance at threshold

The discontinuity in differential resistance at threshold is directly related to the performance of the device in terms of output power and internal quantum efficiency. The differential resistance of all 3P-QCLs (V843 A, V845 A, and V962 A) is calculated from the experimental data in different temperatures. Even though we could observe the discontinuity in differential resistance of V845 and V962, no such discontinuity is observed in V843. The measurement was done several times and the change was below the noise level. We only plot the differential resistance of V845 and V962 which are shown in Fig. 4.17. The differential resistance of V845 A (at different temperatures) versus current density, plotted in Fig. 4.17(a), shows a clear discontinuity at the lasing threshold, whereas the differential resistance is displayed as a smooth curve (dashed-magenta line) for the non-lasing

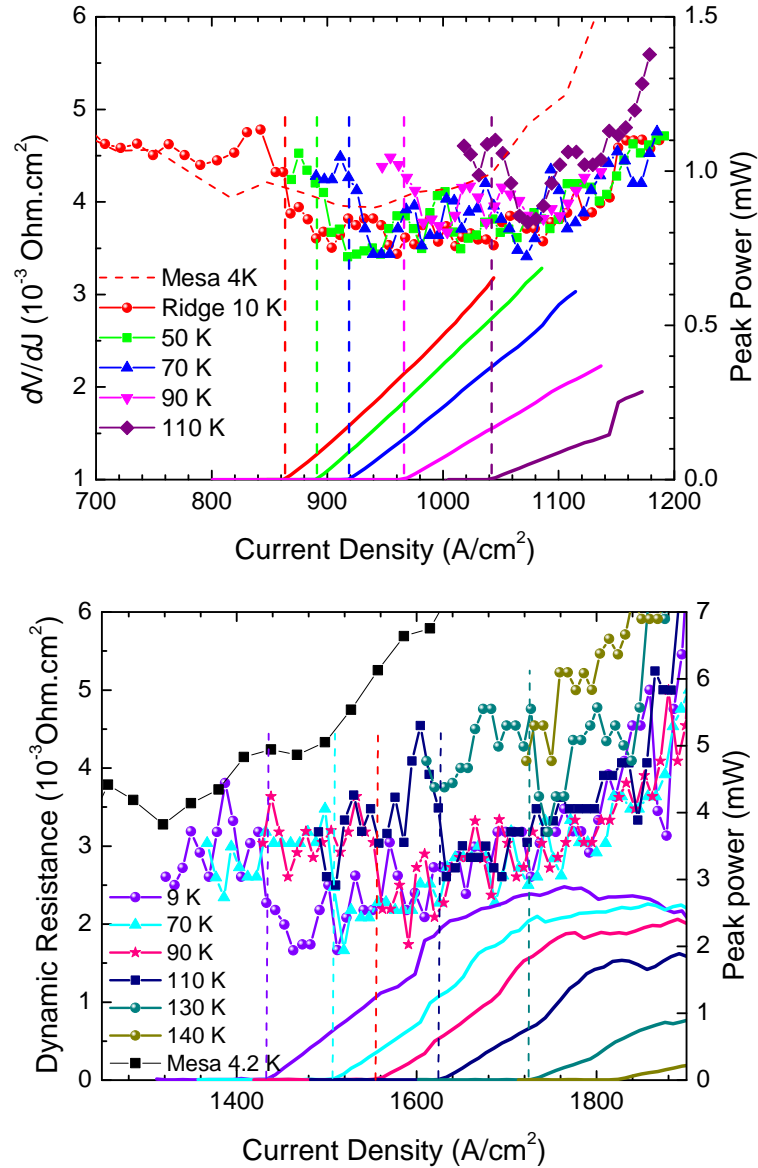


Figure 4.17: The differential resistance of a) V845 and b) V962. Left axis: The differential resistance of non-lasing (the red dashed line) and lasing (solid lines with symbols) device A versus current density at different temperatures. The L-J measurement results are also plotted (right scale) to determine the threshold current at each temperature.

mesa device (shown only at 4 K). The $\sim 16\%$ fractional change of differential resistance at threshold, observed in measurement at 10 K, is lower than what the rate equation model predicts (32% extracted from Fig. 4.16 by assuming $\Delta\nu \times \alpha_{\text{cav}} = 38.5 \text{ THz cm}^{-1}$). To more accurately determine the position of the discontinuity which shifts to higher currents with temperature, the L-J curves of device A are plotted with vertical dashed lines to denote the corresponding threshold points. A better internal efficiency of the second generation of THz 3P-QCL due to the longer *modified* effective lifetime of the ULS and shorter lifetime of the LLS results in a clear discontinuity of differential resistance and a higher output power (1.5 mW in V845 A compared to 0.9 mW in V843 A [60] with the same collecting optics). As mentioned in equation (3.14) in chapter 3 the discontinuity of differential resistance was estimated and appears to depend on two relaxation times associated with the extractor state, the wrong extraction lifetime (τ_{2e}), and the depopulation (τ_{1e}). The discontinuity of differential resistance in V845 is improved compared to the first iteration 3P design (V843) in a two-fold strategy: (i) τ_{2e} is longer because of the thicker radiative barrier ($\tau_{2e}=5.6$ vs. 2.55 ps in V843 at electron temperature of 70 K) which results in a higher *modified* effective ULS lifetime and (ii) τ_{1e} is shorter due to the higher energy spacing to make the depopulation more efficient. The observation of a discontinuity in differential resistance on V845 tends to support our hypothesis about the vanishing discontinuity on V843, which was attributed to a slow depopulation rate as the energy spacing between the states 1 and e was 9 meV below the LO-phonon energy.[60] This discontinuity in differential resistance on V845 is consistent with the higher emission power from this wafer, since $\Delta R_{\text{th}}/R_{\text{th}}$ is closely related to the internal efficiency of the QCL.

In V962, a more substantial discontinuity at laser threshold compared to V845 was observed in the differential resistance of the lasing device at different temperatures, while the differential resistance of non-lasing device is smooth at 4 K as illustrated in Fig.4.17(b) (black line). The L-J measurements of the lasing device are also shown in this figure to easily distinguish the position of discontinuity which is shifted to the right by temperature. The relative change ($\Delta R_{\text{th}}/R_{\text{th}}$) of the measured differential resistance of V962 (33%) is higher than those of V845 (16%) and V843 (not observed at all), which leads to a higher output emission and a higher quantum efficiency. The discontinuity can be observed up to 130 K in Fig.4.17(b), but our measurement setup did not detect any change in differential resistance at threshold in 140K and 144 K.

4.7.3 Comparing the main specification of V843, V845, and V962

In this section we tabulate all main specifications of the three 3P-based QCLs, explain the improvements that were achieved in each new generation, and discuss the strategy

which was employed for improving the device performance. It will help us to see how each generation was advanced over the previous generation. In addition, this result will show us the next approach to improve the performance of the emerging THz QCLs.

Specs	V843	V845	V962
Output power (mW)	0.9	1.5	3.4
Operating temperature (K)	138.5	128.5	144
Threshold current density at 10 K(kA/cm ²)	1.17	0.87	1.44
Maximum current density at 10 K (A/cm ²)	1.56	1.22	2.1
Current dynamic range at 10 K	0.25	0.28	0.3
$\Delta R_{\text{th}}/R_{\text{th}}$ at 10 K	—	16%	32%
$J_{\text{res}}/J_{\text{max}}$	3.7	3.1	3.1
Ω_{ei} (meV)	1.14	0.85	1.54
Ω_{e1} (meV)	0.385	0.23	0.32
Ω_{e2} (meV)	0.34	0.147	0.2
Main lasing frequency (THz)	3.2	2.4	2.6
Leakage current $2 \rightarrow e/J_{\text{max}}$	0.41	0.33	0.26
$k_B T/\hbar\omega$	0.9	1.11	1.15

Table 4.1: Main specifications of each design extracted from experiment (device A) and simulation result are presented.

After we investigated the first generation of THz 3P-QCL, some bottlenecks of this new design was revealed. Low output power, high intermediate resonance current before threshold, no evidence of discontinuity at threshold current in V843 are some of those issues that encouraged us to come up with a new design. In V845, we decided not to change the structure design (stay with the same material system as V843 and the same number of wells and barriers). The wavefunctions were engineered to reduce the intermediate resonance current by lowering the overlap integral of the wavefunctions at electric field below the threshold electric field. The optimization process converged with a design with low oscillator strength. Using a lower oscillator strength could improve the performance of the device in three different aspects. First, the non-lasing transition time will increase which results in a higher population inversion at high temperature. Secondly, since the wavefunctions of level i and level 2 (ULS) are highly overlapped, a lower oscillator strength will reduce the wavefunction overlap of level i and level 1 (LLS) and consequently reduce the wrong injection from level i to level 1 . The lower wrong injection rate to the LLS increases the internal quantum efficient of the device and may improve the output optical power. Thirdly, as the wrong extraction from level 2 to level e can be controlled by energy spacing

and wavefunction overlap between those states, the lower oscillator strength reduces the leakage current path between the ULS and extraction state ($2 \rightarrow e$). One should consider the effect of very diagonal design on increasing the gain bandwidth of the structure and lowering the gain value at low temperature. It can be easily possible to sacrifice the gain too much such that lasing is suppressed. Based on aforementioned discussion, V845 device improved the output optical power of the device by factor of ~ 2 , improve the the discontinuity in differential resistance at threshold (16% in V845 compared to non-visible change in V843), reduced the intermediate resonance current as a fraction of maximum current ($J_{\text{res}}/J_{\text{max}} = 3.1$ in V845 compared to $J_{\text{res}}/J_{\text{max}} = 3.7$ in V843), increase the current dynamic range (in V845 compared to in V843), and decrease the leakage current ($2 \rightarrow e$) as a fraction of maximum current density (in V845 compared to in V843). As shown in table 4.7.3, the maximum operating temperature of V845 A (128.5 K) is lower than that of V843 A (138.5 K) while the maximum operating of V845 B (152.5 K) is higher than that of V843 B (141 K). This could be due to the very diagonal design. The effect of low loss cavity waveguide in design with low oscillator strength is higher than those with high oscillator strength.[92] The $k_B T/\hbar\omega$ parameter increases from 0.9 (0.92) in device A (B) of V845 to 1.11 (1.3) in device A (B) of V845.

In third generation of THz 3P-QCL, even though we used the same material system as V843 and V845, the number of wells per cascade module is increased to 5. We add one extra well in upper phonon stream to on the one hand control the internal quantum efficiency by engineering the wavefunction and on the other hand reduce the intermediate current before threshold. Adding one extra well allowed us to make the injector barrier much narrower than what it was in V843 and V845 (35 Å in V962 compared of 44 Å in V843 and V845). Combination of adding one extra well in upper phonon stream and narrowing the injector barrier results in high output optical power while keep the intermediate resonance low. The oscillator strength of V962 is almost as low as V845 to have the same advantages of V845 in reducing the leakage current and increasing the population inversion and internal quantum efficiency. As a result, V962 enhanced the output optical power of THz 3P-QCL by factor of > 2 , increased the change in differential resistance at threshold (16% in V962 compared to 32% in V845), increased the current dynamic range (0.3 in V962 compared to 0.28 in V845 and 0.25 in V843), and decreased the leakage current ($2 \rightarrow e$) as a fraction of maximum current density (0.26 in V962 compared to 0.33 in V845). The intermediate resonance current as a fraction of maximum current did not change from V962 to V845. The maximum operating temperature of device A in V962 is 144 K which is higher than that of V845 A (128.5 K) and V834 A (138.5 K), while the maximum operating temperature of device B was almost the same. It has to be mentioned that the fabrication process of V962 B was not the same as V843 B and V845 B, so they cannot be directly compared. V962 B performance was very likely affected by its worse device fabrication process. The $k_B T/\hbar\omega$

parameter increases from 1.11 (1.3) in device A (B) of V845 to 1.15 (1.21) in device A (B) of V962.

4.8 Summary

In this chapter, three totally new active region designs based on a novel lasing scheme (3P-QCL) were developed and implemented. Based on our RE model, presented in chapter 3 of this thesis, the first 3P-QCL was designed and optimized. The final selected design was grown by MBE system, fabricated, and characterized. The experimental results encouraged us to do a comprehensive study on this structure and find a new approach to improve the performance of this scheme. The maximum operating temperature of the first generation of 3P-QCL (V843) is 138.5 K and it is almost the same as the first three-well RP-QCL [49]. The low output power and a high intermediate resonance current of V843 were addressed in next generation of 3P-QCL by defining a new figure of merit to maximize the gain at lower current. The discontinuity in differential resistance at threshold which was not observable in V843, was observed in V845 and its output optical power was increased. Finally, a five-well 3P-QCL was designed to further improve the operating temperature and optical power. The highest coupling injection strength was employed in V962 to improve the maximum operating temperature and the output power by increasing the maximum current density of the device. In addition we control the intermediate current not to be so high to affect the dynamic range of the device. Since the $k_B T / \hbar \omega$ of V845 and V962 is almost the same as the world record design, IDP-QCL is promising to continue to break performance record of THZ QCLs.

Chapter 5

Conclusion and future works

5.1 Summary and conclusion

The terahertz (THz) electromagnetic wave with a frequency range of (1–10) THz ($\nu = 30\mu\text{m} - 300\mu\text{m}$) is known to be the most unique area in all EM spectra, since it is not simply available due to lack of compact and convenient radiation sources. Terahertz quantum cascade lasers as coherent, compact solid-state, and high power THz sources start to become a reliable candidate for incredible applications in medicine, security, and astronomy. Even though the operating temperature of THz QCL is still not high enough to work under thermo-cooler system, many efforts have been done after the invention of THz QCL to increase the operating temperature; however the slope of this improvement was not promising in last five years.

Even though most of high performance THz QCLs, including state-of-the-art structure which lased up to ~ 200 K, are based on resonant-phonon (RP) QCL scheme and GaAs/ $\text{Al}_{0.15}\text{Ga}_{0.85}\text{As}$, many researchers have been investigating new material systems or even new design scheme in order to improve THz QCL performance. We developed a new design scheme based on phonon scattering injection to the upper lasing state and direct phonon extraction from lower lasing state to overcome the fundamental limits of designs based on THz RP-QCLs. This thesis presented the details of the design, implementation, and characterization of THz phonon-photon-phonon (3P) QCLs to generate THz waves at higher temperature.

Contrary to RP-QCL structures which are suffering from less than 50% maximum population inversion, the THz 3P-QCL scheme could reach a higher population inversion ideally upto 100%. Similar to any multi quantum well structures, we started with solving the

Schrödinger equation. Different non-lasing scattering times that affect the carrier transport in a THz QCL were discussed and the methods of calculation were introduced. A rate equation model was employed to analytically calculate the transport and the gain of 3P-QCLs. There are some unique features in 3P-QCLs which demarcate this new design scheme from the well-known RP-QCL and even from other indirectly-pumped (IDP) based structures. In RP-QCLs, the resonant tunneling is the mechanism which injects the electron into the ULS while extraction from LLS can be done by either tunneling followed by phonon transition or direct phonon transition. In other IDP QCL, even though electrons are injected into the ULS by a phonon scattering mechanism, the extraction occurred by a tunneling followed by a phonon scattering. It means in all THz QCL structures, presented so far, the injection to the ULS or the extraction from LLS or even both injection and extraction were based on resonant tunneling. In 3P-QCL, there is no injection/extraction state to be in resonance with lasing states. This simple idea helps the 3P-QCL designs not to suffer from broadening due to the resonant tunneling.

The modeling of the new lasing scheme is the key part of the device design. Among different transport modeling systems, used in THz QCL structures, we were interested in a model that on the one hand can be simply implemented for 3P-QCL structure and on the other hand can be rapidly calculated by a PC. A rate equation model with first- and second-order tunneling was implemented and analytical derivation of some important parameters that have the major effects on performance of the design were explained. All those intermediate parameters were employed to find an equation for current density and the gain of the structure which are the most interesting specifications of a THz QCL design. After finalizing the analytical expression of the current density and the gain of the structure, MATLAB program tool was employed to numerically calculate current density and the gain of each structure and to evaluate the design. To find the optimum structure, based on a defined figure of merit, a genetic algorithm was used. Since it was the first time that we developed this new design scheme, we tried to investigate different aspects of each design before the growth and made lot of efforts to accurately characterize them. Three structures were designed, simulated, fabricated, and characterized, then the pros and cons of each structure were discussed.

The performance of the first generation of 3P-QCL was not promising. A figure of merit that maximizes the product of population inversion at lattice temperature of 150 K and the oscillator strength was chosen. The final quantum design (V843 active region design), chosen by the genetic algorithm, was grown on a semi-insulating GaAs substrate by the molecular beam epitaxy (MBE). Two different fabrication processes were used in order to compare the effect of waveguide loss on device performance of this structure. Based on

our metal-effect study on performance of THz QCL and our loss calculation model, devices with top highly doped GaAs and Ti/Au metal process (V843 A) has higher loss compared to devices with no top highly doped material and Ta/Au metal process (V843 B). Two different fabrication processes on a same wafer give us this opportunity to investigate the effect of loss on temperature performance and current density of the structure. V843 A lased up to 138.5 K and output power was less than 1 mW while V843 B lased up to 141 K. Even though the injection coupling strength of V843 at alignment electric field was not high (the injector barrier was thick), the intermediate resonant current before the threshold was high. This comes from the wavefunction engineering which was only optimized at alignment electric field. In addition, the discontinuity in differential resistance at threshold was not observed in this structure, which explains the low output power of this device. The poor performance of V843 persuades us to design a new structure to reduce the intermediate resonant current and increase the internal quantum efficiency. The second generation of the 3P-QCL structure (V845) was designed to reduce the intermediate resonant current and improve the optical output power. As a result, the ratio of the maximum current over the resonance peak current before threshold (J_{\max}/J_{res}) at 10K in V845 is better than that of V843 (3.7 in V845 compared to 3.1 in V843), due to the weaker $e-2$ resonance in V845 because of the wider radiative barrier. A better quantum efficiency of V845 enhances the optical power. In addition, we observed the discontinuity in differential resistance at threshold even though it was still minor (16%). The maximum operating temperature ($T_{\max} = 128.5$ K (152.5 K) in device A (device B)) and the output power (1.5 mW) are also improved. Further improvement in 3P-QCL structure requires some fundamental changes rather than wavefunction engineering of four-well structure. To reach a device with a better performance, we need a high coupling injection device while keeping the intermediate resonant as low as possible. A five-well active region design was therefore proposed to improve the performance of the device in terms of optical power, maximum operating temperature, and intermediate current. Inserting one well in upstream phonon wells can increase the quantum efficiency and reduce the intermediate current. A much more significant discontinuity in differential resistance at threshold a larger current dynamic range of device V962A leading to higher maximum operating temperature (144 K) and optical power (3.4 mW).

In summary, a new lasing scheme was proposed and three different structures were designed and characterized to investigate the performance of this category of structures. Even though the absolute value of the maximum operating temperature was not as high as well-known RP-QCLs, one should consider that the lasing frequency of the proposed designs was lower than that of the high performance devices based on RP-QCL (2.4 THz in 3P-QCL compared to 3.22 THz in [56] and 3.9 THz in [54]). It is fair to compare the $k_B T/\hbar\omega$ parameter of those devices since the waveguide loss increases by wavelength. It

was shown that the second and third generations of 3P-QCL have a higher performance in terms of $k_B T / \hbar \omega$ compared to last two high performance devices, based on RP-QCLs, presented in [56, 54].

5.2 Future works

Even though the presented study started a new design method which could improve the performance of THz QCL, there are some issues either in modeling or designing of this lasing scheme which have to be considered. The proposed future works can be separated in two different areas. Our calculation shows that the roughness scattering mechanism is one of the limiting factors of the 3P-QCLs based on GaAs/Al_{0.25}Ga_{0.75}As material system. It can affect the performance of the design in two parts; i) it increases the non-lasing intersubband scattering rate between the lasing states, which lowers population inversion and thus the optical gain ii) it increases the intrasubband scattering rate and consequently increases the bandwidth of the gain. These two factors add up and deteriorate the performance of the device. Since the energetic barrier in 3P-QCLs is much higher than that of RP-QCLs in order to suppress the leakage to the continuum band, the adverse effect of roughness scattering becomes more severe in 3P-QCLs. We can improve the performance of the device by using different barrier height in one module. All other barriers in one module can be kept as high as all 3P-QCLs in this study to suppress the leakage current, except the radiative barrier can be reduced to mitigate the roughness scattering time.

Besides the roughness scattering issue, a comprehensive study on the effect of doping concentration and thickness of injector barrier on the performance of 3P-QCLs should be conducted. Since the injector barrier in 3P-QCL can be narrowed with minimal effect on quantum efficiency of the device, a 3P-QCL structure with variable injector barrier will show us the a guideline for an optimized design. In growth process, we can keep the thickness of all quantum wells and other barriers fixed and change the thickness of the injector barrier through a unique step-and-align technique. This will minimize device performance deterioration due to MBE grow fluctuation from one bath to another.

RP QCLs are drastically different from the 3P-QCLs in terms of carrier transport and distribution. As a result, the experimental doping concentration in RP QCL may not be applicable to a 3P-QCL. An experimental study needs to be conducted to find the optimum doping concentration for 3P-QCLs.

A simple rate equation model was used in the design and analysis of 3P-QCL structure. The effect of intersubband and intrasubband scattering time between the lasing states

on gain bandwidth was ignored in our current model. This is the key parameter that determines which oscillator strength has to be chosen to increase the population inversion while not affecting the gain bandwidth of the structure. An accurate gain bandwidth extracted from intersubband and intrasubband scattering time between the lasing states will give more reliable prediction compared to what we did in this study (We assumed that the gain bandwidth is constant for all temperatures).

In addition, this model failed in calculation of the intermediate resonant current when the injector barrier is thin and carriers could tunnel between two non-neighbor modules. A comprehensive density matrix model which includes three modules of a design in Hamiltonian can predict the behavior of this lasing scheme accurately. Apparently, a more comprehensive model (of course more complicated) will help a designer to find the optimum design which can demonstrate a better performance compared to what is presented so far.

References

- [1] P. H. Siegel. Terahertz technology. *IEEE Transactions on Microwave Theory and Techniques*, 50(3):910–928, March 2002.
- [2] Benjamin S. Williams. Terahertz quantum-cascade lasers. *Nature Photonics*, 1(9):517–525, September 2007.
- [3] S. Kumar. *Development of Terahertz Quantum-Cascade Lasers*. PhD thesis, Massachusetts Institute of Technology, 2007.
- [4] Rudeger Kohler, Alessandro Tredicucci, Fabio Beltram, Harvey E. Beere, Edmund H. Linfield, A. Giles Davies, David A. Ritchie, Rita C. Iotti, and Fausto Rossi. Terahertz semiconductor-heterostructure laser. *Nature*, 417(6885):156–159, May 2002.
- [5] J. C. Wiltse. History of millimeter and submillimeter waves. *IEEE Transactions on Microwave Theory and Techniques*, 32(9):1118–1127, September 1984.
- [6] Gas Sensing. THz QCL-Based Cryogen-Free Spectrometer for in Situ Trace Gas Sensing. *System*, pages 3331–3340, 2013.
- [7] D. T. Leisawitz, W. C. Danchi, M. J. DiPirro, L. D. Feinberg, D. Y. Gezari, M. Hagopian, W. D. Langer, J. C. Mather, S. H. Moseley, M. Shao, R. F. Silverberg, J. Staguhn, M. R. Swain, H. W. Yorke, and X. Zhang. Scientific motivation and technology requirements for the spirit and specs far-infrared/submillimeter space interferometers. In J. Breckinridge & P. Jakobsen, editor, *Society of Photo-Optical Instrumentation Engineers (SPIE) Conference Series*, volume 4013 of *Society of Photo-Optical Instrumentation Engineers (SPIE) Conference Series*, pages 36–46, July 2000.
- [8] <http://sci.esa.int/home/first>.
- [9] <http://mls.jpl.nasa.gov/index-eos-mls.php>.

- [10] N. C. Luhmann and W. A. Peebles. Instrumentation for magnetically confined fusion plasma diagnostics. *Review of Scientific Instruments*, 55(3):279+, 1984.
- [11] T. G. Phillips and J. Keene. Submillimeter astronomy (heterodyne spectroscopy). *Proceedings of the IEEE*, 80(11):1662–1678, Nov 1992.
- [12] Masayoshi Tonouchi. Cutting-edge terahertz technology. *Nature Photonics*, 1(2):97–105, February 2007.
- [13] Wai L. Chan, Jason Deibel, and Daniel M. Mittleman. Imaging with terahertz radiation. *Reports on Progress in Physics*, 70(8):1325–1379, August 2007.
- [14] Hai-Bo Liu, Hua Zhong, Nicholas Karpowicz, Yunqing Chen, and Xi-Cheng Zhang. Terahertz spectroscopy and imaging for defense and security applications. *Proceedings of the IEEE*, 95(8):1514–1527, 2007.
- [15] Terahertz wave parametric source. *Journal of Physics D: Applied Physics*, 35(3):R1+, February 2002.
- [16] D. J. Cook and R. M. Hochstrasser. Intense terahertz pulses by four-wave rectification in air. *Opt. Lett.*, 25(16):1210–1212, August 2000.
- [17] E. Dupont, Z.R. Wasilewski, and H.C. Liu. Terahertz emission in asymmetric quantum wells by frequency mixing of midinfrared waves. *Quantum Electronics, IEEE Journal of*, 42(11):1157–1174, 2006.
- [18] Q Y Lu, N Bandyopadhyay, S Slivken, Y Bai, M Razeghi, Q Y Lu, N Bandyopadhyay, S Slivken, Y Bai, and M Razeghi. Room temperature terahertz quantum cascade laser sources with 215 μ W output power through epilayer-down mounting Room temperature terahertz quantum cascade laser sources with 215 IW output power through epilayer-down mounting. 011101:1–5, 2013.
- [19] Karun Vijayraghavan, Yifan Jiang, Min Jang, Aiting Jiang, Karthik Choutagunta, Augustinas Vizbaras, Frederic Demmerle, Gerhard Boehm, Markus C Amann, and Mikhail A Belkin. mid-infrared quantum cascade lasers. *Nature Communications*, 4(May):1–7, 2013.
- [20] Q. Y. Lu, N. Bandyopadhyay, S. Slivken, Y. Bai, and M. Razeghi. High performance terahertz quantum cascade laser sources based on intracavity difference frequency generation. *Opt. Express*, 21(1):968–973, Jan 2013.

- [21] Q. Y. Lu, N. Bandyopadhyay, S. Slivken, Y. Bai, and M. Razeghi. Widely tuned room temperature terahertz quantum cascade laser sources based on difference-frequency generation. *Applied Physics Letters*, 101(25):251121, 2012.
- [22] Q. Y. Lu, N. Bandyopadhyay, S. Slivken, Y. Bai, and M. Razeghi. Widely tuned room temperature terahertz quantum cascade laser sources based on difference-frequency generation. *Applied Physics Letters*, 101(25):251121, 2012.
- [23] Karun Vijayraghavan, Robert W. Adams, Augustinas Vizbaras, Min Jang, Christian Grasse, Gerhard Boehm, Markus C. Amann, and Mikhail A. Belkin. Terahertz sources based on [c-caron]erenkov difference-frequency generation in quantum cascade lasers. *Applied Physics Letters*, 100(25):251104, 2012.
- [24] Mikhail A. Belkin, Federico Capasso, Feng Xie, Alexey Belyanin, Milan Fischer, Andreas Wittmann, and Jérôme Faist. Room temperature terahertz quantum cascade laser source based on intracavity difference-frequency generation. *Applied Physics Letters*, 92(20):201101, 2008.
- [25] Wei Shi, Yujie J. Ding, Nils Fernelius, and Konstantin Vodopyanov. Efficient, tunable, and coherent 0.18-5.27-thz source based on gase crystal. *Opt. Lett.*, 27(16):1454–1456, August 2002.
- [26] E. R. Mueller, W. E. Robotham, R. P. Meisner, R. A. Hart, J. Kennedy, and L. A. Newman. 2.5 thz laser local oscillator for the eos chem 1 satellite. March 1998.
- [27] M. Inguscio, G. Moruzzi, K. M. Evenson, and D. A. Jennings. A review of frequency measurements of optically pumped lasers from 0.1 to 8 thz. *Journal of Applied Physics*, 60(12):R161–R192, 1986.
- [28] A. Andronov. Hot electrons in semiconductors and submillimeter waves (review). *Sov. Phys. Semicond*, 21:701–721, 1987.
- [29] E. Gornik and A. A. Andronov. Far-infrared semiconductor lasers. *Optical and Quantum Electronics*, 23:v–v, 1991. 10.1007/BF00619760.
- [30] J. Niels Hovenier, M. Carmen Diez, T. O. Klaassen, W. T. Wenckebach, A. V. Muravjov, S. G. Pavlov, and V. N. Shastin. The p-ge terahertz laser-properties under pulsed- and mode-locked operation. *IEEE Transactions on Microwave Theory and Techniques*, 48(4):670–676, April 2000.

- [31] Faist J., F. Capasso, D. L. Sivco, A. L. Hutchinson, and A. Y Cho. Quantum cascade laser. *Science*, page 264:553, 1994.
- [32] Federico Capasso, Khalid Mohammed, and Alfred Y. Cho. Sequential resonant tunneling through a multiquantum well superlattice. *Applied Physics Letters*, 48(7):478–480, 1986.
- [33] R. F. Kazarinov and R. A. Suris. Possibility of the amplification of electromagnetic waves in a semiconductor with a superlattice. *Sov. Phys. Semicon.*, 5:707–709, 1971.
- [34] R. F. Kazarinov and R. A. Suris. Electric and electromagnetic properties of semiconductors with superlattice. *Sov. Phys. Semicon.*, 6:120–131, 1972.
- [35] Leo Esaki and R Tsu. Superlattice and negative differential conductivity in semiconductors. *IBM Journal of Research and Development*, 14(1):61–65, 1970.
- [36] LL Chang, L Esaki, WE Howard, R Ludeke, and G Schul. Structures grown by molecular beam epitaxy. *Journal of Vacuum Science and Technology*, 10(5):655–662, 1973.
- [37] LL Chang, Leo Esaki, and R Tsu. Resonant tunneling in semiconductor double barriers. *Applied Physics Letters*, 24:593, 1974.
- [38] F. Capasso, K. Mohammed, and A. Cho. Resonant tunneling through double barriers, perpendicular quantum transport phenomena in superlattices, and their device applications. *IEEE Journal of Quantum Electronics*, 22(9):1853–1869, September 1986.
- [39] J. Faist, F. Capasso, C. Sirtori, D. Sivco, and A. Cho. *Chapter 1 Quantum Cascade Laser*, volume 66 of *Semiconductors and Semimetals*, pages 1–83. Elsevier, 1999.
- [40] Benjamin Williams, Sushil Kumar, Qing Hu, and John Reno. Operation of terahertz quantum-cascade lasers at 164 k in pulsed mode and at 117 k in continuous-wave mode. *Opt. Express*, 13(9):3331–3339, May 2005.
- [41] B. S. Williams, S. Kumar, Q. Hu, and J. L. Reno. High-power terahertz quantum-cascade lasers. *Electronics Letters*, 42(2):89+, 2006.
- [42] Sukhdeep Dhillon, Jesse Alton, Stefano Barbieri, Carlo Sirtori, A. de Rossi, M. Caligaro, Harvey E. Beere, and David Ritchie. Ultralow threshold current terahertz quantum cascade lasers based on double-metal buried strip waveguides. *Applied Physics Letters*, 87(7):071107+, 2005.

- [43] Christoph Walther, Giacomo Scalari, Jérôme Faist, Harvey Beere, and David Ritchie. Low frequency terahertz quantum cascade laser operating from 1.6 to 1.8 thz. *Applied Physics Letters*, 89(23):231121, 2006.
- [44] Christoph Walther, Milan Fischer, Giacomo Scalari, Romain Terazzi, Nicolas Hoyler, and Jérôme Faist. Quantum cascade lasers operating from 1.2 to 1.6 thz. *Applied Physics Letters*, 91(13):131122, 2007.
- [45] Sushil Kumar, Benjamin S. Williams, Qing Hu, and John L. Reno. 1.9 thz quantum-cascade lasers with one-well injector. *Appl. Phys. Lett.*, 88(12):121123, 2006.
- [46] Sushil Kumar, Chun Wang I. Chan, Qing Hu, and John L. Reno. A 1.8-THz quantum cascade laser operating significantly above the temperature of $\hbar\omega/kB$. *Nat. Phys.*, 7(December):166–77, December 2010.
- [47] Chun Wang I. Chan, Qing Hu, and John L. Reno. Ground state terahertz quantum cascade lasers. *App. Phys. Lett.*, 101(15):151108, 2012.
- [48] Benjamin S. Williams, Sushil Kumar, Hans Callebaut, Qing Hu, and John L. Reno. Terahertz quantum-cascade laser operating up to 137 k. *Applied Physics Letters*, 83(25):5142–5144, 2003.
- [49] H. Luo, S. R. Laframboise, Z. R. Wasilewski, G. C. Aers, H. C. Liu, and J. C. Cao. Terahertz quantum-cascade lasers based on a three-well active module. *App. Phys. Lett.*, 90(4):041112, 2007.
- [50] Mikhail A. Belkin, Jonathan A. Fan, Sahand Hormoz, Federico Capasso, Suraj P. Khanna, Mohamed Lachab, A. G. Davies, and Edmund H. Linfield. Terahertz quantum cascade lasers with copper metal-metal waveguides operating up to 178 k. *Opt. Express*, 16(5):3242–3248, Mar 2008.
- [51] H Luo, S R Laframboise, Z R Wasilewski, and H C Liu. Effects of injector barrier on performance of terahertz quantum-cascade lasers. *Electronics Letters*, 43(11), 2007.
- [52] H Luo, S R Laframboise, Z R Wasilewski, H C Liu, and J C Cao. Effects of extraction barrier width on performance of terahertz quantum-cascade lasers. *Electronics Letters*, 44(10), 2008.
- [53] H. C. Liu, M. Wächter, D. Ban, Z. R. Wasilewski, M. Buchanan, G. C. Aers, J. C. Cao, S. L. Feng, B. S. Williams, and Q. Hu. Effect of doping concentration on the performance of terahertz quantum-cascade lasers. *Applied Physics Letters*, 87(14):141102, 2005.

- [54] Sushil Kumar, Qing Hu, and John L. Reno. 186 k operation of terahertz quantum-cascade lasers based on a diagonal design. *Applied Physics Letters*, 94(13):131105+, 2009.
- [55] E. Dupont, S. Fatholouloumi, and H. C. Liu. Simplified density-matrix model applied to three-well terahertz quantum cascade lasers. *Phys. Rev. B*, 81(20):205311, May 2010.
- [56] S. Fatholouloumi, E. Dupont, C.W.I. Chan, Z.R. Wasilewski, S.R. Laframboise, D. Ban, A. Mátyás, C. Jirauschek, Q. Hu, and H. C. Liu. Terahertz quantum cascade lasers operating up to ~ 200 k with optimized oscillator strength and improved injection tunneling. *Opt. Express*, 20(4):3866–3876, Feb 2012.
- [57] S. Fatholouloumi, E. Dupont, Z. R. Wasilewski, C. W. I. Chan, S. G. Razavipour, S. R. Laframboise, Shengxi Huang, Q. Hu, D. Ban, and H. C. Liu. Effect of oscillator strength and intermediate resonance on the performance of resonant phonon-based terahertz quantum cascade lasers. *Journal of Applied Physics*, 113(11):113109, 2013.
- [58] H. Yasuda, T. Kubis, P. Vogl, N. Sekine, I. Hosako, and K. Hirakawa. Nonequilibrium green’s function calculation for four-level scheme terahertz quantum cascade lasers. *Appl. Phys. Lett.*, 94(15):151109, 2009.
- [59] Tillmann Kubis, Saumitra Raj Mehrotra, and Gerhard Klimeck. Design concepts of terahertz quantum cascade lasers: Proposal for terahertz laser efficiency improvements. *Appl. Phys. Lett.*, 97(26):261106, 2010.
- [60] E. Dupont, S. Fatholouloumi, Z. R. Wasilewski, G. Aers, S. R. Laframboise, M. Lindskog, S. G. Razavipour, A. Wacker, D. Ban, and H. C. Liu. A phonon scattering assisted injection and extraction based terahertz quantum cascade laser. *J. Appl. Phys.*, 111(7):073111, 2012.
- [61] Masamichi Yamanishi, Kazuue Fujita, Tadataka Edamura, and Hirofumi Kan. Indirect pump scheme for quantum cascade lasers: dynamics of electron-transport and very high t_0 -values. *Opt. Express*, 16(25):20748–20758, Dec 2008.
- [62] Andreas Wacker. Extraction-controlled quantum cascade lasers. *Appl. Phys. Lett.*, 97(8):081105, 2010.
- [63] Tao Liu, Tillmann Kubis, Qi Jie Wang, and Gerhard Klimeck. Design of three-well indirect pumping terahertz quantum cascade lasers for high optical gain based on nonequilibrium green’s function analysis. *Appl. Phys. Lett.*, 100(12):122110, 2012.

- [64] Masamichi Yamanishi, Kazuue Fujita, Nanfang Yu, Tadataka Edamura, Kazunori Tanaka, and Federico Capasso. 3-4 thz ingaas / inalas quantum-cascade lasers based on the indirect pump scheme. paper presented at Conference on Lasers and Electro-Optics, Baltimore, MD, USA, 1-6 May 2011.
- [65] Kazuue Fujita, Masamichi Yamanishi, Shinichi Furuta, Kazunori Tanaka, Tadataka Edamura, Tillmann Kubis, and Gerhard Klimeck. Indirectly pumped 3.7 thz ingaas/inalas quantum-cascade lasers grown by metal-organic vapor-phase epitaxy. *Opt. Express*, 20(18):20647–20658, Aug 2012.
- [66] Masamichi Yamanishi, Kazuue Fujita, Shinichi Furuta, Kazunori Tanaka, Tadataka Edamura, Tillmann Kubis, and Gerhard Klimeck. Indirect pumping thz ingaas/inalas quantum-cascade-lasers with coupled-well injectors grown by movpe. paper presented at International quantum cascades laser school and workshop, Baden, Austria, 2-6 September 2012.
- [67] Nannapaneni N. Rao. *Elements of Engineering Electromagnetics (6th Edition)*. Prentice Hall, 6 edition, February 2004.
- [68] S. Kohen, B. S. Williams, and Q. Hu. Electromagnetic modeling of terahertz quantum cascade laser waveguides and resonators. *Journal of Applied Physics*, 97(5), March 2005.
- [69] Benjamin S. Williams, Hans Callebaut, Sushil Kumar, Qing Hu, and John L. Reno. 3.4-thz quantum cascade laser based on longitudinal-optical-phonon scattering for depopulation. *Applied Physics Letters*, 82(7):1015–1017, 2003.
- [70] W. J. Moore and R. T. Holm. Infrared dielectric constant of gallium arsenide. *Journal of Applied Physics*, 80(12):6939–6942, 1996.
- [71] Robert E. Collin. *Foundations for Microwave Engineering*. Wiley-IEEE Press, 2 edition, December 2000.
- [72] Ranjan Singh, Evgenya Smirnova, Antoinette J. Taylor, John F. O’Hara, and Weili Zhang. Optically thin terahertz metamaterials. *Opt. Express*, 16(9):6537–6543, Apr 2008.
- [73] N. Laman and D. Grischkowsky. Terahertz conductivity of thin metal films. *Applied Physics Letters*, 93(5):051105, 2008.

- [74] M A Seo, H R Park, S M Koo, D J Park, J H Kang, O K Suwal, S S Choi, P C M Planken, G S Park, N K Park, Q H Park, and D S Kim. Terahertz field enhancement by a metallic nano slit operating beyond the skin-depth limit. *Convergence*, 3(March), 2009.
- [75] C. Sirtori, H. Page, C. Becker, and V. Ortiz. Gaas-algaas quantum cascade lasers: physics, technology, and prospects. *IEEE Journal of Quantum Electronics*, 38(6):547–558, June 2002.
- [76] J. S. Yu, S. Slivken, A. Evans, J. David, and M. Razeghi. Very high average power at room temperature from 5.9- μ m quantum-cascade lasers. *Applied Physics Letters*, 82(20):3397–3399, 2003.
- [77] S. Fatholouloumi, E. Dupont, S. G. Razavipour, S. R. Laframboise, A. Delage, Z. R. Wasilewski, A. Bezinger, G. Z. Rafi, S. Safavi-Naeini, D. Ban, and H.C. Liu. Electrically switching transverse modes in high power thz quantum cascade lasers. *Opt. Express*, 18(10):10036–10048, May 2010.
- [78] Jonathan A. Fan, Mikhail A. Belkin, Federico Capasso, Suraj P. Khanna, Mohamed Lachab, A. Giles Davies, and Edmund H. Linfield. Wide-ridge metal-metal terahertz quantum cascade lasers with high-order lateral mode suppression. *Applied Physics Letters*, 92(3):031106, 2008.
- [79] Saeed Fatholouloumi, Emmanuel Dupont, S Ghasem Razavipour, Sylvain R Laframboise, Guy Parent, Zbigniew Wasilewski, H C Liu, and Dayan Ban. On metal contacts of terahertz quantum cascade lasers with a metalmetal waveguide. *Semicond. Sci. Technol.*, 26(10):105021, 2011.
- [80] J. S. Blakemore. Semiconducting and other major properties of gallium arsenide. *Journal of Applied Physics*, 53(10):R123–R181, 1982.
- [81] V.W.L. Chin, T. Osotchan, M.R. Vaughan, T.L. Tansley, G.J. Griffiths, and Z. Kachwalla. Hall and drift mobilities in molecular beam epitaxial grown gaas. *Journal of Electronic Materials*, 22(11):1317–1321, 1993.
- [82] M. A. Ordal, Robert J. Bell, Jr R. W. Alexander, L. L. Long, and M. R. Query. Optical properties of fourteen metals in the infrared and far infrared: Al, co, cu, au, fe, pb, mo, ni, pd, pt, ag, ti, v, and w. *Appl. Opt.*, 24(24):4493–4499, Dec 1985.

- [83] David Burghoff, Tsung-Yu Kao, Dayan Ban, Alan Wei Min Lee, Qing Hu, and John Reno. A terahertz pulse emitter monolithically integrated with a quantum cascade laser. *Applied Physics Letters*, 98(6):061112, 2011.
- [84] Paul Harrison. *Quantum Wells, Wires and Dots: Theoretical and Computational Physics*. John Wiley & Sons, March 2005.
- [85] D. F. Nelson, R. C. Miller, and D. A. Kleinman. Band nonparabolicity effects in semiconductor quantum wells. *Phys. Rev. B*, 35:7770–7773, May 1987.
- [86] G. Bastard. *Wave mechanics applied to semiconductor heterostructures*. EDP Sciences, January 1992.
- [87] Takeya Unuma, Masahiro Yoshita, Takeshi Noda, Hiroyuki Sakaki, and Hidefumi Akiyama. Intersubband absorption linewidth in gaas quantum wells due to scattering by interface roughness, phonons, alloy disorder, and impurities. *Journal of Applied Physics*, 93(3):1586–1597, 2003.
- [88] Tsuneya Ando. Line width of inter-subband absorption in inversion layers: Scattering from charged ions. *J. Phys. Soc. Jpn.*, 54(7):2671–2675, 1985.
- [89] C. Deutsch, H. Detz, M. Krall, M. Brandstetter, T. Zederbauer, A. M. Andrews, W. Schrenk, G. Strasser, and K. Unterrainer. Dopant migration effects in terahertz quantum cascade lasers. *Applied Physics Letters*, 102(20):201102, 2013.
- [90] Hans Callebaut, Sushil Kumar, Benjamin S. Williams, Qing Hu, and John L. Reno. Importance of electron-impurity scattering for electron transport in terahertz quantum-cascade lasers. *Applied Physics Letters*, 84(5):645–647, 2004.
- [91] Jurgen H. Smet, Clifton G. Fonstad, and Qing Hu. Intrawell and interwell inter-subband transitions in multiple quantum wells for far-infrared sources. *Journal of Applied Physics*, 79(12):9305–9320, 1996.
- [92] Alpár Mátyás, Mikhail A. Belkin, Paolo Lugli, and Christian Jirauschek. Temperature performance analysis of terahertz quantum cascade lasers: Vertical versus diagonal designs. *Applied Physics Letters*, 96(20):201110, 2010.
- [93] Carlo Sirtori, Federico Capasso, Jérôme Faist, and Sandro Scandolo. Nonparabolicity and a sum rule associated with bound-to-bound and bound-to-continuum intersubband transitions in quantum wells. *Phys. Rev. B*, 50:8663–8674, Sep 1994.

- [94] Jonathan A. Fan, Mikhail A. Belkin, Federico Capasso, Suraj P. Khanna, Mohamed Lachab, A. Giles Davies, and Edmund H. Linfield. Wide-ridge metal-metal terahertz quantum cascade lasers with high-order lateral mode suppression. *Applied Physics Letters*, 92(3):031106, 2008.
- [95] Giacomo Scalari, Romain Terazzi, Marcella Giovannini, Nicolas Hoyler, and Jérôme Faist. Population inversion by resonant tunneling in quantum wells. *Appl. Phys. Lett.*, 91(3):032103, 2007.
- [96] Sushil Kumar and Qing Hu. Coherence of resonant-tunneling transport in terahertz quantum-cascade lasers. *Phys. Rev. B*, 80:245316, Dec 2009.
- [97] S.-C. Lee and A. Wacker. Nonequilibrium green's function theory for transport and gain properties of quantum cascade structures. *Phys. Rev. B*, 66:245314, Dec 2002.
- [98] T. Kubis, C. Yeh, P. Vogl, A. Benz, G. Fasching, and C. Deutsch. Theory of nonequilibrium quantum transport and energy dissipation in terahertz quantum cascade lasers. *Phys. Rev. B*, 79:195323, May 2009.
- [99] T. Schmielau and Jr. M. F. Pereira. Nonequilibrium many body theory for quantum transport in terahertz quantum cascade lasers. *Appl. Phys. Lett.*, 95(23):231111, 2009.
- [100] Hans Callebaut, Sushil Kumar, Benjamin S. Williams, Qing Hu, and John L. Reno. Analysis of transport properties of tetrahertz quantum cascade lasers. *Appl. Phys. Lett.*, 83(2):207–209, 2003.
- [101] Hans Callebaut, Sushil Kumar, Benjamin S. Williams, Qing Hu, and John L. Reno. Importance of electron-impurity scattering for electron transport in terahertz quantum-cascade lasers. *Appl. Phys. Lett.*, 84(5):645–647, 2004.
- [102] Christian Jirauschek, Giuseppe Scarpa, Paolo Lugli, Miriam S. Vitiello, and Gaetano Scamarcio. Comparative analysis of resonant phonon thz quantum cascade lasers. *J. Appl. Phys.*, 101(8):086109, 2007.
- [103] Carlo Sirtori, F. Capasso, Jerome Faist, A.L. Hutchinson, Deborah L. Sivco, and Alfred Y. Cho. Resonant tunneling in quantum cascade lasers. *Quantum Electronics, IEEE Journal of*, 34(9):1722–1729, 1998.
- [104] Romain Terazzi, Tobias Gresch, Andreas Wittmann, and Jérôme Faist. Sequential resonant tunneling in quantum cascade lasers. *Phys. Rev. B*, 78:155328, Oct 2008.

- [105] Romain Terazzi and Jérôme Faist. A density matrix model of transport and radiation in quantum cascade lasers. *New journal of Physics*, 12(3):033045, 2010.
- [106] F. Carosella, C. Ndebeka-Bandou, R. Ferreira, E. Dupont, K. Unterrainer, G. Strasser, A. Wacker, and G. Bastard. Free-carrier absorption in quantum cascade structures. *Phys. Rev. B*, 85:085310, Feb 2012.
- [107] C. Ndebeka-Bandou, F. Carosella, R. Ferreira, A. Wacker, and G. Bastard. Relevance of intra- and inter-subband scattering on the absorption in heterostructures. *Appl. Phys. Lett.*, 101(19):191104, 2012.
- [108] C. Deutsch, H. Detz, M. Krall, M. Brandstetter, T. Zederbauer, A. M. Andrews, W. Schrenk, G. Strasser, and K. Unterrainer. Dopant migration effects in terahertz quantum cascade lasers. *App. Phys. Lett.*, 102(20):201102, 2013.
- [109] S. G. Razavipour, E. Dupont, S. Fatholouloumi, C. W. I. Chan, M. Lindskog, Z. R. Wasilewski, G. Aers, S. R. Laframboise, A. Wacker, Q. Hu, D. Ban, and H. C. Liu. An indirectly pumped terahertz quantum cascade laser with low injection coupling strength operating above 150 k. *Journal of Applied Physics*, 113(20):203107, 2013.
- [110] Mikhail V. Kisin, Michael A. Stroscio, Gregory Belenky, and Serge Luryi. Electron-plasmon relaxation in quantum wells with inverted subband occupation. *Appl. Phys. Lett.*, 73(15):2075–2077, 1998.
- [111] Tao Liu, Kenneth E. Lee, and Qi Jie Wang. Microscopic density matrix model for optical gain of terahertz quantum cascade lasers: Many-body, nonparabolicity, and resonant tunneling effects. *Phys. Rev. B*, 86:235306, Dec 2012.
- [112] H. Willenberg, G. H. Döhler, and J. Faist. Intersubband gain in a bloch oscillator and quantum cascade laser. *Phys. Rev. B*, 67:085315, Feb 2003.
- [113] Romain Terazzi, Tobias Gresch, Marcella Giovannini, Nicolas Hoyler, Norihiko Sekine, and Jerome Faist. Bloch gain in quantum cascade lasers. *Nat. Phys.*, 3:329–333, 2007.
- [114] Yu Yao, Zhijun Liu, A.J. Hoffman, K.J. Franz, and C.F. Gmachl. Voltage tunability of quantum cascade lasers. *IEEE J. Quant. Electron.*, 45(6):730–736, june 2009.
- [115] L. C. West and S. J. Eglash. First observation of an extremely large-dipole infrared transition within the conduction band of a gaas quantum well. *Applied Physics Letters*, 46:1156–1158, June 1985.

- [116] Wilfried Maineult, Pierre Gellie, Alessio Andronico, Pascal Filloux, Giuseppe Leo, Carlo Sirtori, Stefano Barbieri, Emilien Peytavit, Tahsin Akalin, Jean F. Lampin, Harvey E. Beere, and David A. Ritchie. Metal-metal terahertz quantum cascade laser with micro-transverse-electromagnetic-horn antenna. *Applied Physics Letters*, 93(18):183508+, 2008.
- [117] Hans Callebaut and Qing Hu. Importance of coherence for electron transport in terahertz quantum cascade lasers. *J. Appl. Phys.*, 98(10):104505, 2005.
- [118] Rikard Nelander and Andreas Wacker. Temperature dependence of the gain profile for terahertz quantum cascade lasers. *Appl. Phys. Lett.*, 92(8):081102, 2008.
- [119] Giacomo Scalari, Christoph Walther, Jérôme Faist, Harvey Beere, and David Ritchie. Electrically switchable, two-color quantum cascade laser emitting at 1.39 and 2.3 thz. *Applied Physics Letters*, 88(14):141102, 2006.